HOT TEARING SUSCEPTIBILITY OF SINGLE-PHASE Al-3.8 wt%Zn-1 wt%Mg ALLOY USING THE CONSTRAINED ROD SOLIDIFICATION EXPERIMENT: *INFLUENCE OF 1.2 wt%Fe ADDITION AND GRAIN REFINEMENT*

HOT TEARING SUSCEPTIBILITY OF SINGLE-PHASE Al-3.8 wt%Zn-1 wt%Mg ALLOY USING THE CONSTRAINED ROD SOLIDIFICATION EXPERIMENT: *INFLUENCE OF 1.2 wt%Fe ADDITION AND GRAIN REFINEMENT*

By AMANDA MAIA AGUIAR, B.Eng.

A Thesis Submitted to the School of Graduate Studies in Partial Fulfilment of the Requirements for the Degree of Master of Applied Science

MASTER OF APPLIED SCIENCE (2020)

Mechanical Engineering

McMaster University, Hamilton, Ontario

TITLE: Hot Tearing Susceptibility of Single-Phase Al-3.8 wt%Zn-1 wt%Mg Alloy Using the Constrained Rod Solidification Experiment: *Influence of 1.2 wt%Fe Addition and Grain Refinement*

AUTHOR: Amanda Maia Aguiar, B. Eng

SUPERVISOR: Dr. Sumanth Shankar

Number of Pages: xiv, 123

ABSTRACT

The increasing global demand for a substantial lightweighting of automobiles to enable a reduction in the greenhouse gas (GHG) emissions and fuel consumption has led to the adaptation of the high strength Al wrought alloys such as the 2xxx and 7xxx series in near net-shaped manufacturing using the high pressure die casting (HPDC) process. However, the obstacle for this adaptation is the high susceptibility to hot tearing during the solidification of these alloys. A new structural Al alloy for high pressure die casting application was developed from the single-phase Al-Zn-Mg family; a high strength and ductile alloy that could be adapted to manufacturing automotive structural components using HPDC and help with a significant reduction in the overall curb-weight of an automobile and thereby increasing the vehicle fuel efficiency. The objective of this study was to enable a better understanding of the hot tearing phenomenon during solidification of the Al-3.8 wt%Zn-1 wt%Mg alloy, the effect of adding 1.2 wt% Fe to the alloy to improve the castability in HPDC process and the effect of adding Ti as a grain refiner of the primary Al phase during solidification of the alloy using Al-5 wt%Ti-1 wt%B master alloy. The constrained rod solidification (CRS) experiments were carried out to measure transient stress, transient strain, and transient temperature during solidification of the alloy. Improvements to the CRS experiments were also developed to obtain a repeatability of the acquired data. The computerized Tomography (CT) imaging was used to visually characterize the hot tearing. Hypothesis on the factors promoting the hot tearing tendencies in single-phase alloys solidified using net-shaped casting processes has been presented with evidence-based on transient stress-strain and thermal data curves obtained during the solidification experiments.

ACKNOWLEDGEMENTS

TABLE OF CONTENTS

LIST OF FIGURES

LIST OF TABLES

CHAPTER 1. *INTRODUCTION*

The world population has had a significant growth over the last century and is anticipated to exceed 10 billion by the year 2100, according to the United Nations Report in 2019 [1], as shown in Figure 1.1. Consequently, the number of automobiles and the consumption of natural resources will also increase. Over the past few decades, the cost of the natural resources and concerns of deteriorating global environment have drastically increased, resulting in a higher global demand for significant lightweighting of automobiles so as to realize a notable reduction in greenhouse gas (GHG) emission and fuel consumption; mandating manufacturing of automobiles that are more energy-efficient, cost-effective, and environmentally friendly.
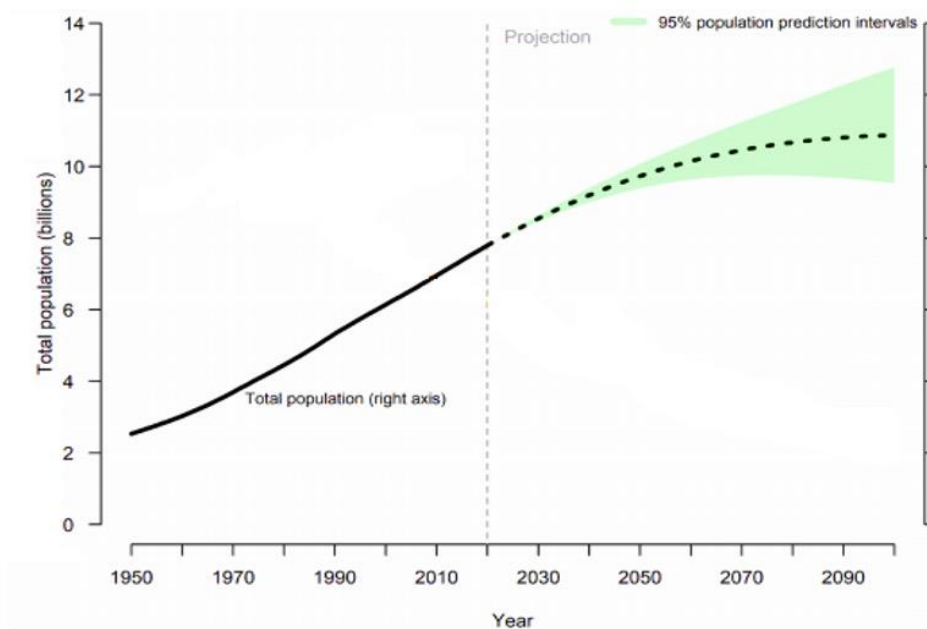
Figure 1.1: World Population Size Growth 1950-2020 and medium-variant projection with 95 percent prediction intervals, 2020-2100 [after 1].

Many countries have implemented stringent regulations on increased average fuel economies for cars and light trucks [2]. For example, in the USA, the average fuel economy of fleet cars and light trucks produced by a car manufacturer had to increase to 54.5 mpg (mile per US gallon) by the year 2025, while in Canada, the fuel economy target for passenger automobiles would have to be 56.2 mpg by 2025, as shown in Figure 1.2: Passenger car fuel economy in the last 10 years and future targets [4]. In the European Union, it would have to be 57.9 mpg by 2025, in South Korea it is regulated to be 58.8 mpg by 2020, and in China, 56 mpg by 2025. Additionally, this trend had also been adapted by other transportation sectors such as aerospace and railway, where decreasing the overall weight of a vehicle has been mandated for improved fuel efficiency and decreased carbon emissions [3].
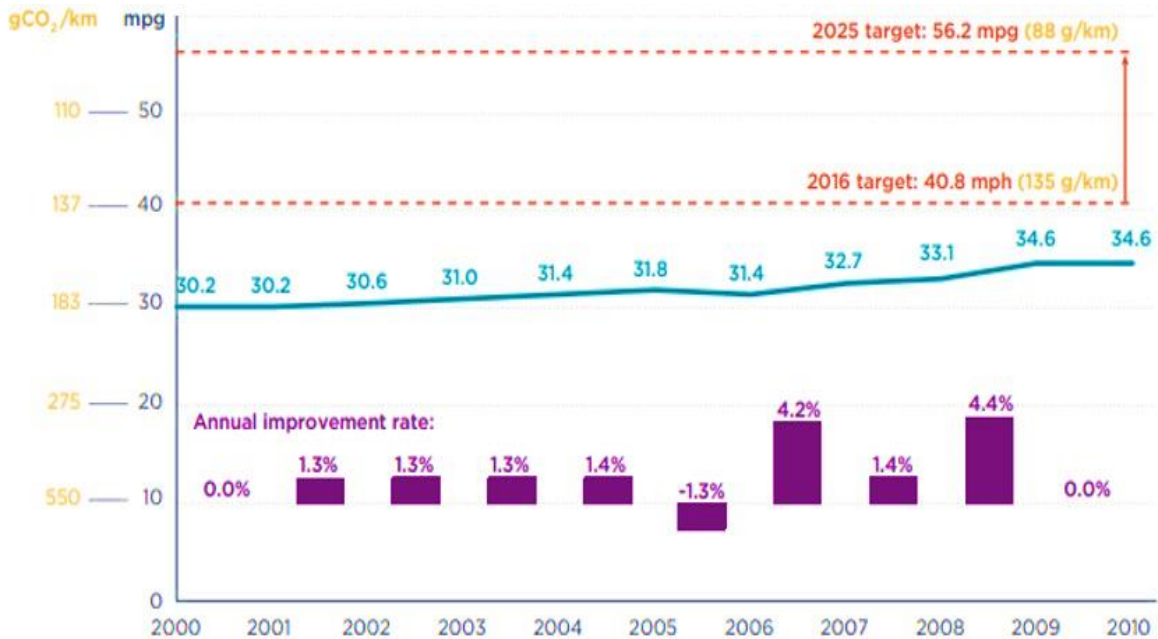
Figure 1.2: Passenger car fuel economy in the last 10 years and future targets [4].

One of the popular approaches for lightweighting automobiles is the substitution of high-density materials such as steel with low-density ones such as aluminum and magnesium alloys. Over the past decade, a significant shift to incorporate an increasing amount of alternate lightweight materials such as advanced high strength steel (AHSS), magnesium alloys, polymer matrix composites (PMCs) and aluminum alloys has been driving the research and development (R&D) in the automotive industry. The use of aluminum alloys in passenger automobiles has shown significant benefits in curb-weight reduction and lowering GHG emissions. This has resulted in an increase of the use of aluminum by about 23%, from 1995 to 2007 [4]. According to the Ducker Worldwide report [5], by 2028, at least 16% of the curb-weight of vehicles in North America will be aluminum alloys, in comparison to 13% in 2020. The report predicts that aluminum content in North American light vehicles will continue to grow uninterruptedly until 2028, as shown in Figure 1.3 and Figure 1.4.
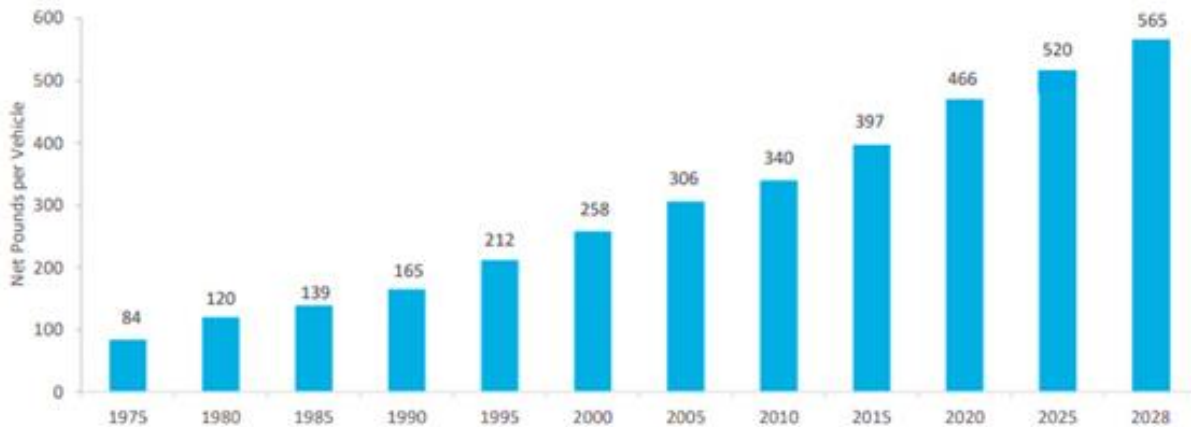
Figure 1.3: Aluminum content in light automobiles in North America [5].

Figure 1.4: Typical selection of alternate lightweight materials in a light car [6].

Among the several options for using lightweight alloys, the aluminum alloys have shown the most promise to be easily adapted as lightweighting alternatives to ferrous alloys for reducing the curb-weight of automobiles. However, typically, only the polyphase aluminum alloys with a significant volume fraction of eutectic phases (>10 %) lend themselves to sound near net shape casting processes. Further, these polyphase alloys are limited in their strengths and ductility even with variations of heat treatments on the cast component. The single-phase Al alloys typically do not lend themselves to near net shape casting processes because of the inherent problems of hot tearing during solidification, which renders the component defective. However, the mechanical properties and performance of a single-phase Al alloy are far superior to the polyphase versions because of the significant reduction in the evolution of secondary phases during solidification that diminish properties and performance. Moreover, solidification of the single-phase alloys takes place over a larger temperature regime when compared to the polyphase counterparts. The single-phase alloys are typically formed into net shape components

using solid-state transformation processes such as forging, extrusion, drawing, stamping, etc., all of which significantly increase the manufacturing cost and cycle time when compared to near net shape casting processes.

Increasing the use of single-phase Al alloys such as the 5xxx, 6xxx and 7xxx series [7] over the polyphase counterparts such as the 2xx, 3xx and 4xx series [8], to replace existing structural ferrous components in automobiles would lead to significant lightweighting [5]. However, the increased manufacturing complexities and costs prohibit the use of solid-state transformation processes in manufacturing net shape components using Al single-phase alloys, also termed as *wrought* alloys. Innovation in adapting near net shape casting process to manufacture structural automotive components using aluminum single-phase alloys is warranted to realize the necessary lightweighting. The global need for innovations in cost-effective casting processes and integration of the structural optimization strategies into the automotive component design is mandatory to successfully enable lightweighting without compromising on vehicle performance.

Near net shape casting processes such as insulating and metal mould processes account for manufacturing about 60% of aluminum products in an automobile [5]; among these, the high-pressure die casting (HPDC) is one of the most common processes used by automobile manufactures currently, because of the significantly lower manufacturing cost and cycle-time. While HPDC is widely used in the automotive industry, the process itself is fraught with significant gas porosity due to the highly turbulent nature of molten metal injection into the metal die mould [9]. Hence, components manufactured using HPDC processes do not lend themselves to heat treatment because of problems such as

blistering and exhibit a significant reduction of the ductility, rendering them ineffective as structural automotive components [10].

High Vacuum High-pressure Die Casting (HVHPDC) is a new and advanced HPDC process that creates a significant vacuum (<50 mbar) during the filling of the die mould so as to alleviate the gas entrapment and porosity in the solidified component. HVHPDC improves mechanical properties, performance, enables heat treatment without blistering and facilitates net shape manufacturing of structural cast components for automobiles. However, even with all these improvements in the process, the problem of hot tearing in single-phase Al would not be mitigated.

The main problem of high Hot Tearing Susceptibility (HTS) in single-phase Al alloys would necessitate modification of the alloy chemistry with suitable elements that mitigate the same and process parameters to adapt to the marked changes in the rate of transient fraction solid evolution during solidification of these alloys. Figure 1.5 shows images of a typical hot tearing problem seen on a structural Top Hat component that was manufactured using the HVHPDC process with the new Al-Zn-Mg-Fe single-phase alloy. The Top Hat component die tool was modified to present locations that promotes hot tearing, wherein, a relatively thin wall thickness of the component was placed in-between opposing thicker wall thickness sections to enable increased solidification strain fields and create a favourable scenario for HTS for an in-depth study of the defect phenomenon in these alloys with HVHPDC.
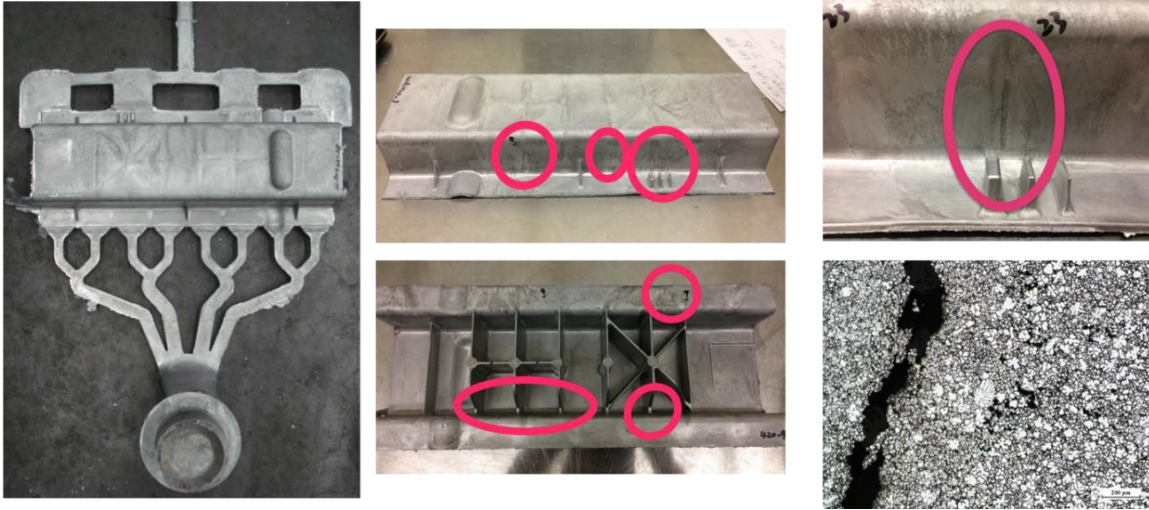
Figure 1.5: Typical hot tearing observed in a customized Top Hat component casting manufactured in HVHPDC with the new Al-Zn-Mg-Fe single-phase alloy.

The purpose of this study was to understand the hot tearing phenomena in primary single-phase Al alloys, specifically the newly developed Al-Zn-Mg-Fe system and provide recommendations to alleviate the HTS of these alloys in the HVHPDC process. Uniaxial transient strain and stress were measured during solidification using a constrained rod segment within a metal (H13 steel) mould and these data were coupled with the analyses of the macro- and microstructure of the solidified component to better understand and quantify the HTS of the Al-Zn-Mg-Fe system. The A356.2 alloy was also evaluated using the same experiment plan to provide a comparative analysis with a familiar alloy system. The grain morphology and microstructure were characterized using the optical and scanning electron microscope. Thermal analysis simulations and techniques were conducted to identify the onset temperature and solid fraction of hot tearing in the experiment and to understand the solidification characteristics and feeding behaviour of the single-phase alloy.

CHAPTER 2. *LITERATURE REVIEW*

An in-depth understanding of the current state-of-the-art in this research would require a critical review of the HVHPDC process, hot tearing susceptibility in Al alloys along with the models that define the same and transient evolution of solid fraction during the solidification of Al alloys. These topics are further expanded in this chapter.

2.1.   High Vacuum High-Pressure Die Casting

High-pressure die casting (HPDC) is a process where molten metal or metal alloy is forced at high speed and under high-pressure into reusable steel mould which is typically made from tempered H13 tool steel. This process is considered a quick, reliable and cost-effective manufacturing method for producing a high volume of components that have tight tolerances and require low surface roughness and high dimensional accuracy. It is regularly used in the automotive industry and the majority of the alloys can be cast using this technology [11,12].

The molten metal is injected into the mould cavity through an injection plunger in a fraction of a second and it is held in the mould by a powerful compressor until the metal solidifies. Once the metal is solidified the mould is opened, the cast part disengaged, and the die surface is sprayed with lubricant to continue the casting cycle. In summary, the HPDC process consists of three important phases: injection of molten metal, solidification, part extraction, and spraying of the die surface. It is considered one of the fasted castings processes; however, due to its complexity and a large number of critical parameters that need to be controlled, its optimization is tedious and less predictable[11].

Figure 2.1 shows the typical traces of the transient parameters during one HVHPDC shot Cycle. When the melt is filled into the shot-sleeve, the air pressure in the mould cavity corresponds to the atmospheric pressure (1bar) (Figure 2.1b). As the plunger moves forward at a low velocity (slow shot), a signal is sent from the die casting machine to the vacuum system that makes the air pressure in the mould cavity slightly to increase. Once the plunger has passed the filling opening, the vacuum starts the forced venting, drawing out air and gases of the shot-sleeve and the mould cavity (see Figure 2.1c).

(a)

(b)

(c)
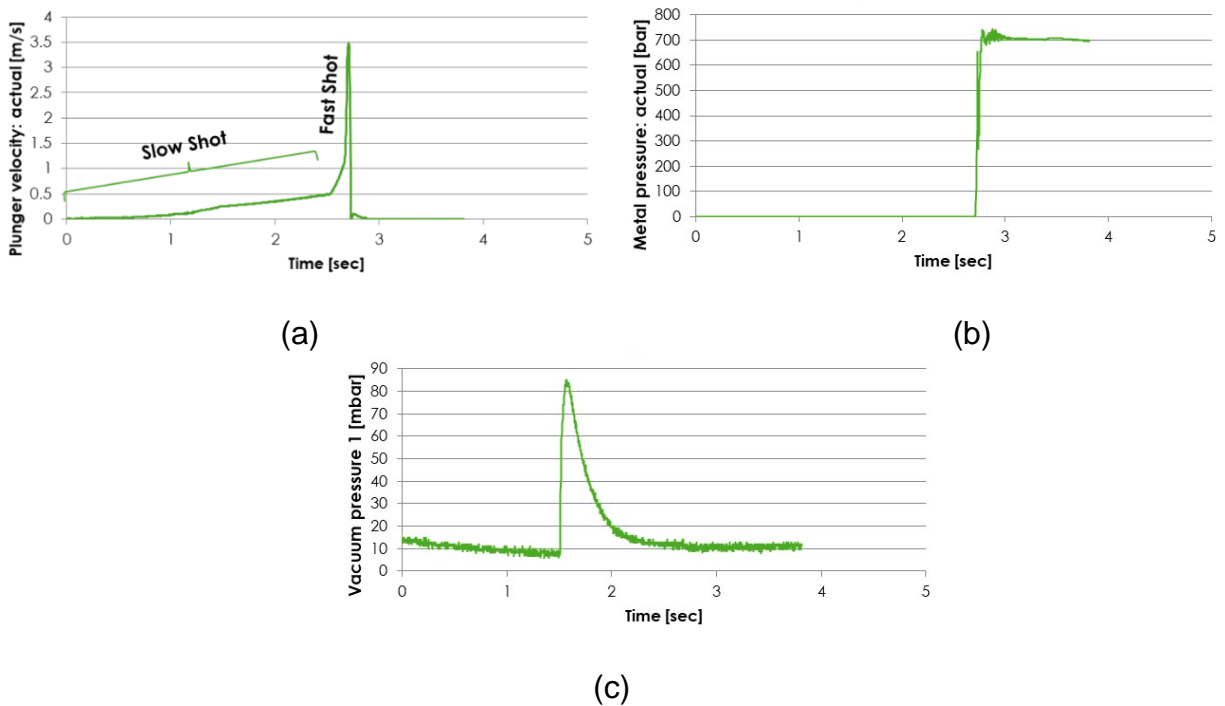
Figure 2.1: Typical traces of (a) plunger velocity, (b) metal pressure and (c) transient vacuum during metal injection and solidification of Al-Zn-Mg-Fe alloy in HVHPDC process [13].

During the first phase (slow shot), the plunger moves at low velocities up to the changeover point (~ 2.8s) to the second phase (fast shot) in which the velocity is increased (see Figure 2.1a). When the melt reaches the end of the mould cavity and the die casting

machine switches to mould filling speed, the metal pressure in the mould cavity slowly reaches the maximum vacuum value, which is 700bar (see Figure 2.1b) and the velocity of the plunger increases to 3.5m/s (see Figure 2.1a). Then, the second half of the mould filling phase is now reached, and the mould cavity is now completely filled.

High-Q cast is an innovative commercial HVHPDC process [14,15] that was innovated to produce structural and heat treatable Al alloy castings from a polyphase Al-Si-Mg family of alloys to realize significant improvements to component ductility, strength and performance. Figure 2.2 shows a schematic of the typical advantages of significant reduction in porosity in the cast component from introducing high vacuum into the HPDC process.
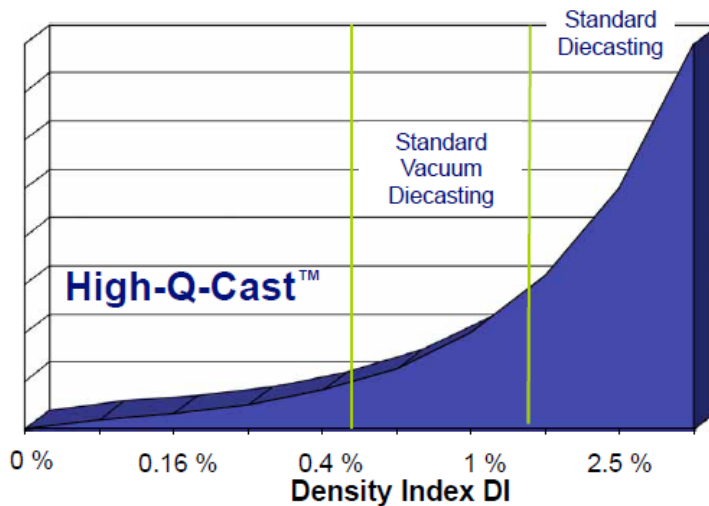
Figure 2.2: Porosity density in different types of HPDC [15].

According to Ducker worldwide analysis [16], to realize the aggressive lightweight strategies in automobile designs, there should be a significant increase in components manufactured by the HVHPDC (termed Vacuum Die Casting (VDC) in the report) so as to enable manufacturing structural Al components to replace some of the ferrous

counterparts. Figure 2.3 highlights the current trend in the typical automotive manufacturing processes in North America, wherein, the market for vacuum die casting of polyphase Al alloys would have to grow from 7 lb per light vehicle now (2020) to 12 lb by the year of 2025. This coupled with the innovation of enabling HVHPDC of single-phase Al alloys would further expand the opportunities for improved automotive lightweight.

This chart excludes rod and bar, fin stock, brazing sheet, forgings and all castings except VDC
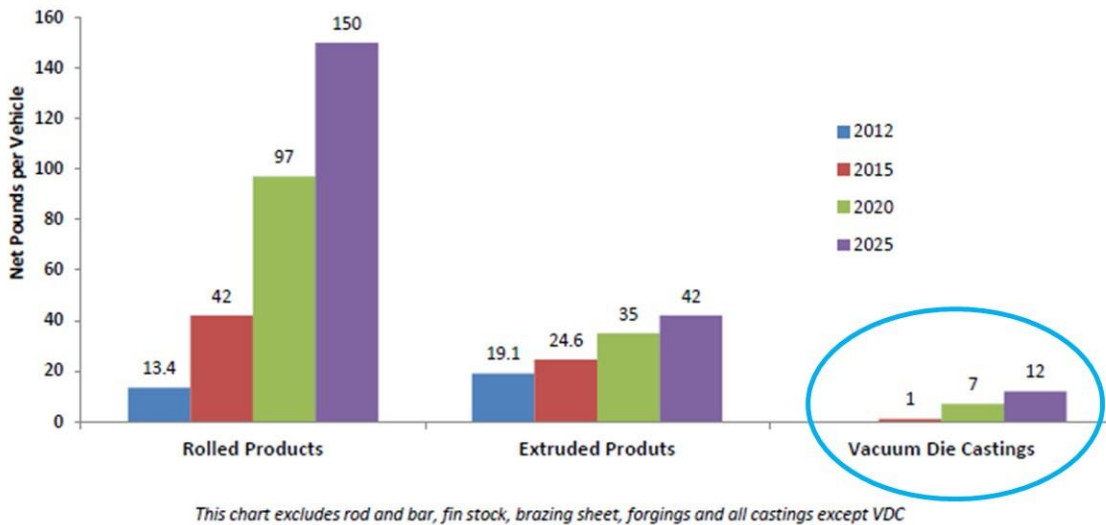
Figure 2.3: Net Pounds per Vehicle for Select Processes, highlighting HVHPDC [16]

While the process is capital intensive, with upfront expenses in die tool manufacturing, HVHPDC machine and other process related setup expenses, the operation costs and throughput rate are significantly lower than other near net shape casting processes. Weight reduction - very thin walls, part integration (replacing weldments), high mechanical properties, crash performance, distortion free with tight tolerances, corrosion resistance, pressure tightness, allowance of using heat treatment and single-phase alloys are some of the advantages of using HVHPDC. However, the hot tearing is still are an issue even using this process and innovations in the process and improvements in the alloys are necessary to alleviate HTS.

2.2.   Hot Tearing

Hot Tearing is a defect that happens in metal casting parts during solidification. Predicting a hot tearing phenomenon is challenging due to the complexity of the mushy zone (liquid + solid coexists) during solidification. Typically, phenomena that lead to hot tearing are shrinkage and hindered contraction that builds-up of local stresses, and lack of liquid feeding in the mushy zone during solidification, as a result of high fraction solids and blockages by intermetallic phases [17,18].

Figure 2.4 illustrates the hot tearing susceptibility in a dendritic solidification alloy. Several studies [18–22] have shown that polyphase alloys with a dendritic structure of the primary solidifying phase have a higher tendency to hot tearing. During the solidification, the grains being formed are subjected to continual shrinkage and increasing strain; continuous feeding by the remaining liquid in the mushy zone would be necessary to compensate for the shrinkage and heal voids. Further, in polyphase alloys, the intermetallic phases (IMP) start to evolve during solidification, typically after ~25% solid fraction has evolved, resulting in a complex and disconnected network of such IMP around the grains of primary Al phases, leading to blockages of the intergranular feeding paths for the liquid to compensate for shrinkage during solidification, which leads to a lack of feeding and consequently resulting in the formation of stable voids that lead to hot tearing from the increasing strain fields concentrated around the growing voids [23].
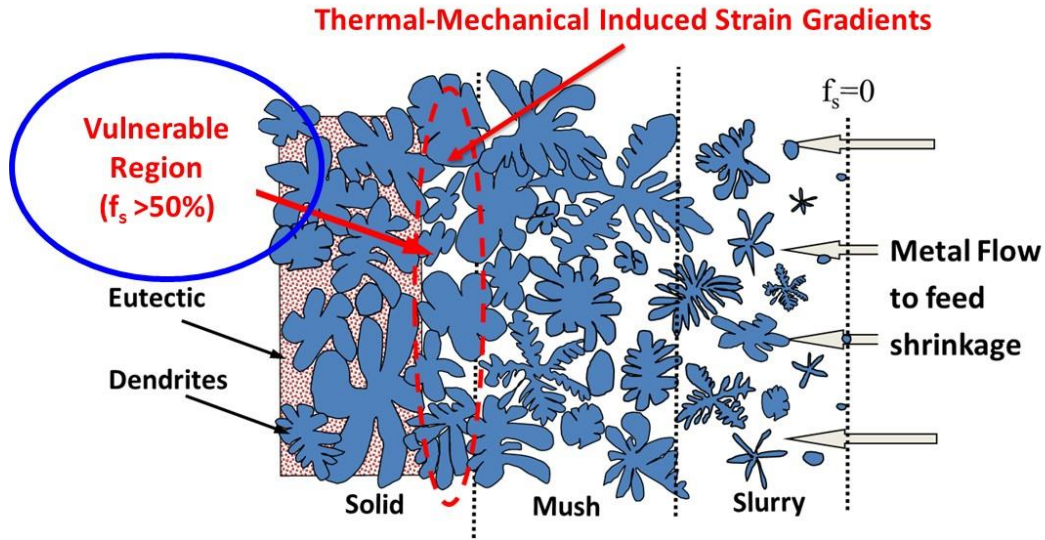
Figure 2.4 Schematic representation of hot tearing susceptibility in a polyphase alloy with a dendritic structure of primary solidifying phase [24].

Figure 2.5 shows the hot tearing susceptibility in a typical binary hypoeutectic alloy, solidifying with a non-dendritic structure of the primary phase, where the fraction of solid varies from 0 at the $T_{liquidus}$ to 1 at the $T_{solidus}$. There are some stages during the solidification process that are critical to understanding the hot tearing phenomenon; $T_{Cohesion}$ is related to the point that the liquid feeding to compensate the shrinkage during the solidification starts to become limited due to the grains impingement on one another and the path for the liquid feeding through the network of primary phases becomes restricted; T_{Film} is when there is about 35-55% of solid formed; $T_{Coalesce}$ is where 90% of the solid network is formed and the grains coalesce with a thin film of liquid around the primary grains. The region after the T_{Film} and closer to the $T_{Coalesce}$ is when the alloy is most susceptible to hot tearing; due to the high fraction of solid that restricts the intergranular feedability. In addition, the thin liquid layer around the primary phase is weak and it could promote hot tearing when subjected to local solidification local stresses.
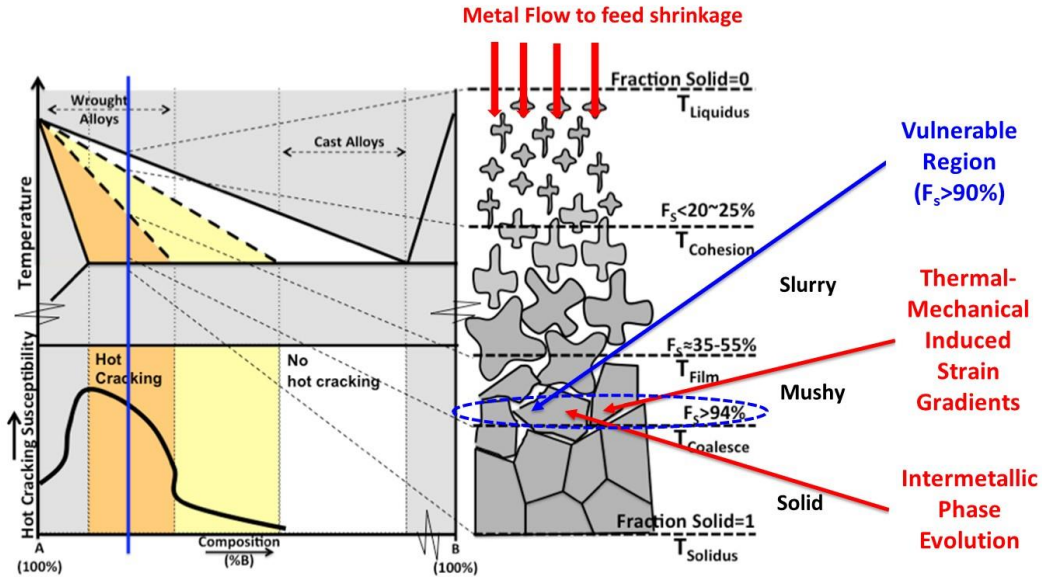
Figure 2.5: Schematic representation of hot tearing susceptibility as a function of fraction solid during solidification of a binary alloy system and non-dendritic structure [25].

The non-dendritic structure has shown to alleviate hot tearing by modifying the grain structure from columnar dendritic to equiaxed by using grain refiner, varying alloy compositions and thermal conditions [21,23,26]. A non-dendritic primary phase morphology results in a higher amount of liquid fraction and a higher fluidity of the alloy in the mould to fill the voids between the grains and to form a well-bridged structure that can resist the increasing solidification strain and stress [23,25].

Over the years the hot tearing during solidification of near net shape casting has been studied and analyzed by several researchers [17,20,23,27–30]. Li et al. [31] developed a detailed review of hot tearing and critical factors that affect it: alloy composition, grain morphology, mould preheat temperature and pouring temperature are the salient ones.

Various phenomenological models and criteria have been developed to better understand and predict hot tearing; the details of these are presented in Section 2.2.4 of this thesis.

2.2.1. Alloys composition, Grain Morphology, and Intermetallic Phases

Metallic alloys are broadly categorized as either single-phase or polyphase alloys. Figure 2.6 shows the evolution of transient solid fraction during solidification of the mushy zone (modelled using Scheil-Gulliver solute redistribution paradigm) in a typical single-phase (AA7050) [7] and polyphase (A356.2) [8] alloys. Figure 2.6 shows that in the polyphase alloys, the rate of evolution of the solid fraction is gradual while in the single-phase alloys, the evolution is significantly rapid, initially. As an example, for the formation of 25% solid in both the alloys, the temperature difference (ΔT) between $T_{Liquidus}$ and $T_{Cohesion}$ for a single-phase alloy is substantially smaller than for the polyphase alloy leading to a rapid formation of the coherent grain network in the former. Polyphase alloys usually do not present $T_{Coalesce}$, and the primary Al ceases to evolve at around the 50% solid regime, leaving a significant bulk of liquid to solidify as a polyphase eutectic system; consequently, the continuous volumetric shrinkage during the solidification would be constantly fed by the remaining bulk liquid, resulting in the absence of hot tears. In a single-phase alloys, the primary Al phase evolves for a large range of temperature until a solid fraction of around 0.9, which renders the system with a significantly thin layer of liquid that would be weak to resist the large strain and stress fields from solidification and not efficiently fed by the bulk liquid; leading to high HTS. Further, during the final stages of solidification of a single-phase alloy (>70 % Solid) if and when an IMP forms during solidification, these tend to block the liquid feeding paths in the intergranular regions and disconnecting portions of

the solidifying system from the bulk liquid feeding. This could also contribute to increasing

HTS. Hence, HTS in single-phase alloys is greater than that for the polyphase counterpart

and the lack of liquid feeding the final stages of solidification in these alloys could due to

one or a combination of blocking feeding paths by the evolution of IMPs and the inability

of the liquid to feed the capillary pathways.
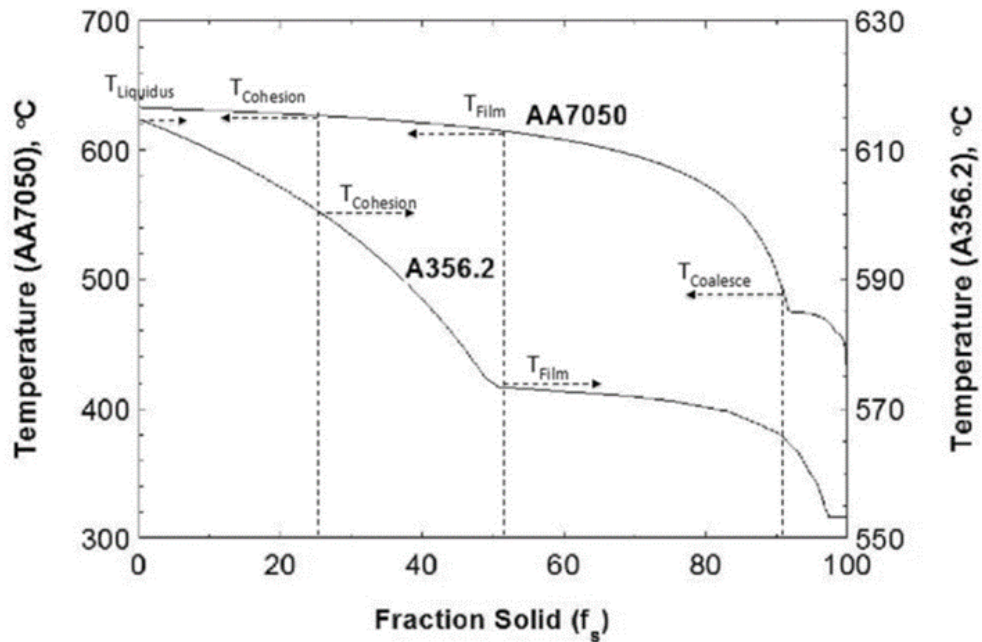
Figure 2.6: Typical evolution of transient solid fraction as a function of temperature for a single-phase alloy and polyphase alloy; AA7050 and A356.2, respectively. [23]

In 1975, Clynes and Davis [32] designed a permanent mould using a dog-bone specimen,

where it was possible to measure the total cracking through the resistance variations in

the mould. Aiming to promote directional solidification and axial contraction stresses in

order to simulate an environment suitable for crack formation, water coolers were installed

at the end of the mould and a heating coil in the center of the mould, to create a

customized thermal gradient during solidification; hence, forcing the heat extraction to be nearly unidirectional. In this study, the composition of the Al-Mg alloys and initial melt pouring temperatures were the independent parameters. It was found that a maximum cracking susceptibility occurred at around 1 wt% Mg and subsequently, the HTS decreased with increasing solute content in the alloy; further, it was found that only a *super* purity Al metal would alleviate HTS and even a small amount of impurities would increase HTS in aluminum alloys [32]. Tensile tests were carried out in the cracked samples and results showed that a big single crack is more harmful than multiple small cracks [32].

In 2010, Strobel et al. [33] developed a study to evaluate the castability of Mg-Al alloys cast using the HPDC process; a new casting design was developed to simulate all the factors that can affect the quality of a good casting, such as low fluidity and stresses. Five alloys were tested with four (4) levels of the solute Al content (2.4% to 8.9%) and one containing a higher Zn content (Mg-12Zn-4Al / ZA124) under four (4) variations of fast shot velocities and die temperatures, alike. The results showed that the alloy ZA124 followed with higher Al content, cast with the higher fast shot plunger velocity and higher die temperature has a better castability based on the evaluation criteria for cracking, filling, and spangling (surface quality). Low plunger velocity and low die temperature promoted casting with a high number of defects, such as porosity and lack of filling. It was also observed that increasing the Al content decreases the liquidus temperature, the solidification temperature range and rate of solidification, while, increasing the eutectic content in the final solidified structure. A higher amount of eutectic would be beneficial for the castability from the enhanced feedability during solidification [33].

In 2011, in a similar study, Easton et al [34] studied the castability of a family of creep-resistant HPDC alloys with three different Mg alloys cast with the HPDC process while varying the fast shot plunger velocity and nominal die mould preheat temperatures. It was observed that Mg-alloys with a higher content of aluminum cast with a higher fast shot velocity and higher die temperature has a better castability. The alloy with a higher content of Ca showed the worst performance possibly due to oxide formed in some spots. Notably, the castability rating criteria presented in these works [33,34] were developed from visual inspection and hence, qualitative.

Several studies [28,35–39] have showed that grain size and morphology also have a strong effect on hot tearing tendencies. Most of the research results indicate that refinement of the grain morphology improved resistance to hot tearing. Pumphrey and Lyons [21] carried out experiments on the effect of grain refinement on binary Al alloys achieved by increasing solute additions. It was found that increasing solute content on the binary alloy systems (Al-Si, Al-Cu, Al-Mg, Al-Zn), decreased grain size, consequently decreasing HTS. When the grain structure changed from columnar to equiaxed, HTS decreased due to changes in the distribution of eutectic phases and reduction in grain size. It was indicated that the finer the primary grains, the higher the probability of having eutectic phases around the grains, thus, promoting better feedability during solidification and alleviating HTS [21].

In 1975, Clyne and Davies [32] also performed a study adding Titanium as a grain refiner in two Al-Mg alloys, Al-2%Mg (low cracking susceptibility) and Al-1%Mg (high cracking susceptibility). Both alloys with no grain refiner (Ti) had a columnar grain morphology. The results demonstrated that the low susceptibility alloy had an increase in cracking tendency

over a narrow range of Ti content as it can be seen in Figure 2.7, even though the grain size has become smaller and equiaxed. The high susceptibility alloy was affected by the grain refiner, Ti additions, but only at high levels of >0.2 % Ti, although the grain changed from columnar to equiaxed. They concluded that was there was a complex relation among impurity content, grain structure, and cracking susceptibility [32].
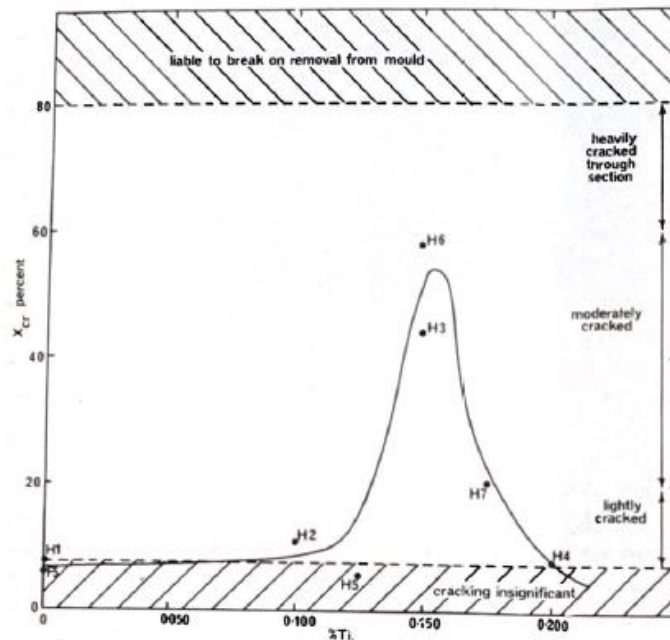
Figure 2.7: Variation of cracking fraction with composition for a high purity Al-2%Mg alloy with Ti [32].

Warrington and McCartney [26] carried out a study in the 7000 series alloys, 7050 and 7010 (Al-Zn-Mg-Cu alloys) to analyze the effect of grain refinement on hot tearing. The experiments consisted of additions of Ti ranging from 0 to 0.05 wt%. Both alloys showed a columnar Al grain structure with no grain refiner (Ti) addition. It was found that some grain refinement is beneficial in 7000 series alloys; additions of Ti ranging from 0.015 to 0.03 wt% showed to be very effective in reducing hot tearing susceptibility when changing the grain structure from columnar to equiaxed-dendritic. However, additions above 0.03%

promoted the formation of extremely small grains with an equiaxed-cellular structure, which made the hot tearing tendency to become worse. They concluded that, when exposed to solidification stresses, the areas with the equiaxed dendritic network that is highly branched and connected, are less susceptible to hot tearing than those areas with unbranched cellular grains [26].

In 2004, Easton et al. [28] performed a study on the influence of grain structure on hot tearing susceptibly in wrought alloys and using a modified Rappaz-Drezet-Gremaud (RDG) [20] hot tearing model. The experiments were carried out using the aluminum alloy 6061 that was cast in a hot tearing rig with varying levels of Ti addition as a grain refiner: The load developed during solidification was measured as a function of temperature. The results obtained are shown in Figure 2.8; the grain refined samples has a delayed onset of load development and increasing the grain refinement, decreased the load developed during solidification [28].

It was found that Ti additions were very effective in decreasing the grain size and changing the grain morphology from large columnar to dendritic equiaxed grains, which resulted in a decrease in hot tearing tendencies. However, further refinement of the cellular equiaxed grains morphology was attributed to causing an increase in hot tearing tendencies due to a reduction in permeability of the liquid through the microstructure [28,35]; these results mirrored those obtained by Warrington and McCartney [26], as well. Additional studies using different wrought aluminum alloys and cooling rates showed that increasing the cooling rate increased the grain refinement and consequently decreased the hot tearing susceptibility [35].
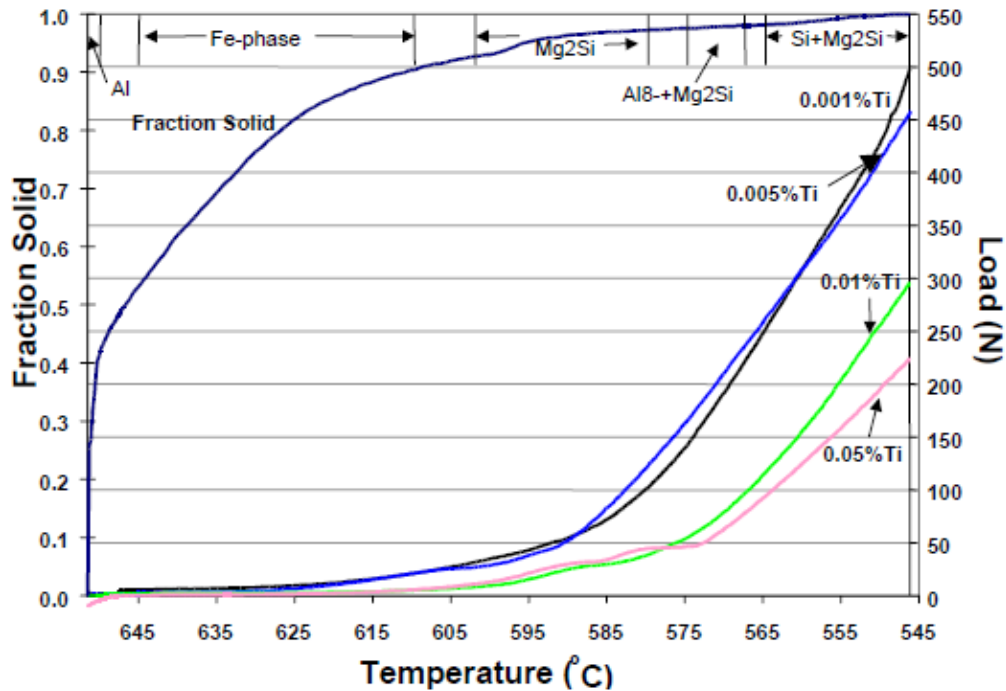
Figure 2.8: Load measured during solidification of alloy 6061 with different grain refiner levels. Transient solid fraction and phase formation are shown as a function of temperature [28].

Mazahery [40] carried out experiments in a permanent mould casting to study the effect of Ti addition on the Al-3Zn-1Mg alloy. Additions of 0.05wt% Ti were added to the alloy and the grain size morphologies and sizes can be seen in Figure 2.9. The results showed that the grains without Ti addition (shown in Figure 2.9a) are approximately 400μm in size, while the grains with Ti addition (shown in Figure 2.9b) are approximately 80μm, demonstrating that Ti is a great grain refiner for this system. Moreover, refined grain structures improve the hot tearing resistance, and consequently the casting quality [40,41].
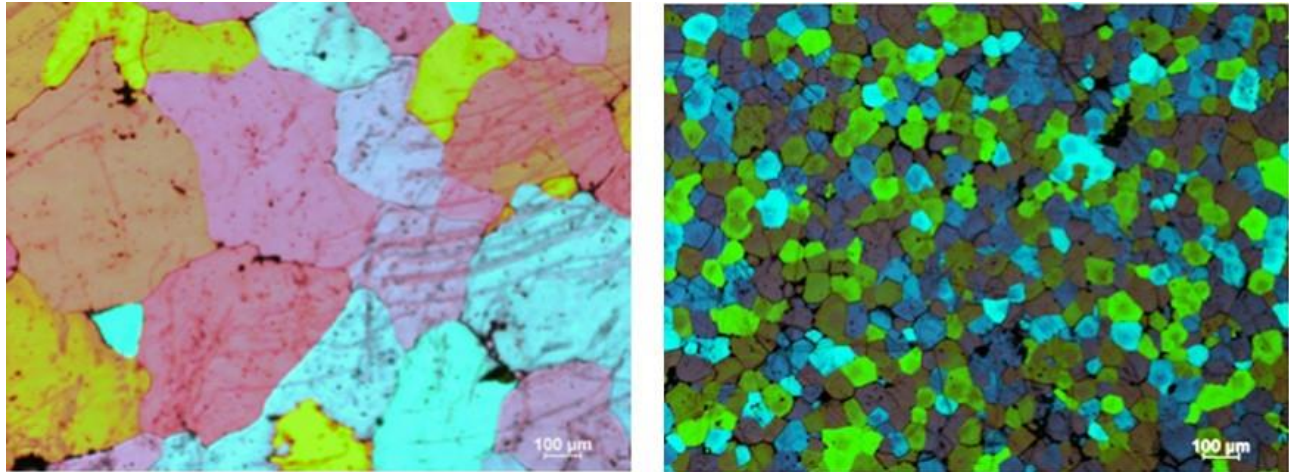
<p align="center">(a)   (b)</p>

Figure 2.9: Optical micrographs showing the effect on grain size and morphology when adding 0.05wt% of Ti to the Al-3Zn-1Mg alloy cast using permanent mould, (a) without Ti addition, (b) with Ti addition [40].

Several studies [42–47] have shown that the IMPs evolving during solidification have a strong influence on the HTS, in many different Al alloys systems. Sweet et al.[19] studied the influence of Fe content on hot tearing susceptibility of Al 6060 alloy using a CAST hot tearing rig. The alloy used in the study was Al-0.52Si-0.34Mg-xFe-0.05Ti with Fe varying from 0.10 to 0.30 wt%. During the experiment, hot tears were observed when Fe additions were varied from 0.02 to 0.22 wt%. However, the maximum susceptibility was observed from 0.05 to 0.15 wt% Fe and almost no hot tear was present above 0.22 wt% Fe. These results proved that Fe additions have a strong effect on hot tearing susceptibility, higher the Fe content lower the hot tearing susceptibility. It was also measured the load during solidification and the results relating to solid fraction could be observed in Figure 2.10. In the graph, it could be observed that the mean load development curves, obtained from several experiment repetitions show that the alloy with a higher iron content shows a

marked transition in load gradient at a lower F_s and the change in gradient occurs at increasing F_s values as the Fe content in the alloy is increased. The experiments showed the as the Fe content increase, the load at $T_{coalesce}$ increases, $T_{coalesce}$ occurs at a lower F_s and HTS decreases, which contradicts with other studies for such alloys where the load had been shown to decrease with increasing HTS [19].

The authors propose that the alloys with a higher Fe content of 0.55 wt% showed less HTS, even when the load curves in Figure 2.10 shows a trend that opposes this observation when compared to other literature sources [19]. The explanations presented to support the conclusion that the HTS reduces as Fe content increases are not entirely convincing because the relationship between transient load developed during solidification and transient fraction solid was established through the theoretical S-G paradigm which would over predict the solid fraction at any given temperature when compared to the transient solid fraction evolution in an experiment.
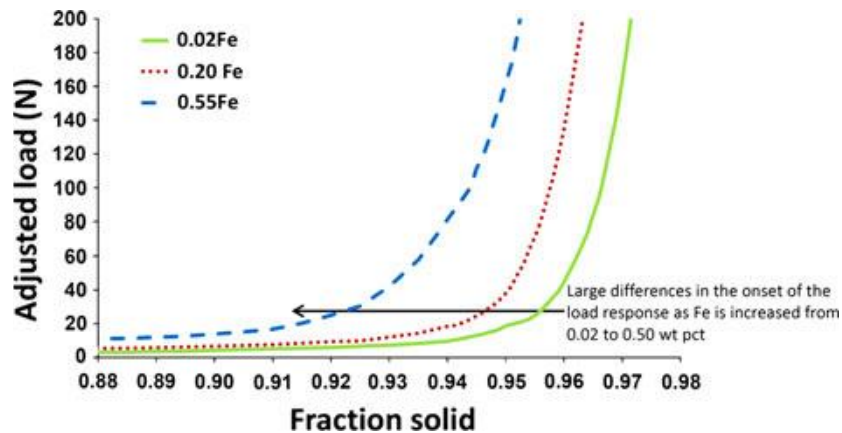
Figure 2.10: Averaged load versus f_s for hot tearing experiment grouped according to Fe content [19].

According to Sweet et al. [19], when Fe is added to the system, as the amount of Fe is increased the dendrite coherency point ($f_{s,0}$) and grain coalesce point ($f_{s,co}$) is moved to lower fraction solids. This way, the region influencing hot tearing is narrower and the hot tearing susceptibility decreases. However, due to a grain coalescence at lower fraction solids, the initial load development starts earlier, which leads to higher load development at the end of the solidification and lower hot tearing susceptibility. A schematic was presented (shown in Figure 2.11) to explain the transient load development and its relationship to the dendrite coherency point ($f_{s,0}$) and grain coalesce point ($f_{s,co}$). Further, analyses on the intermetallic phase morphologies were performed on the SEM and simulations were carried out using the RDG model [20] modified by Grandfield [24] and using Thermo-Calc thermodynamic software. Different types of intermetallic phases were found and showed to have a strong influence on hot tearing [19].

The β-Al$_5$FeSi intermetallic phase when fully formed was found to be the most helpful in reducing hot tearing when compared to other intermetallics since it helps the grains to bridge earlier and to develop strength. However, typically, the significant amount of interface anisotropy between the β-Al$_5$FeSi intermetallic phase and the primary Al phase would lead to a reduction in the network strength of the microstructure rather than an increase in the same. Further, the evidence presented in the publication does not entirely support the conclusion of the role of Fe based IMPs in changing the hot tearing tendencies of the alloy. Further, the variance in the observed data for hot tearing has a significant scatter to arrive at a statistically sound conclusion. They concluded that for the 6060 alloys system, the hot tearing susceptibility reduction is related to the morphology,

prevalence, and solidification sequence of Fe-based intermetallics and eutectics, and their influence on grain coalescence [19].
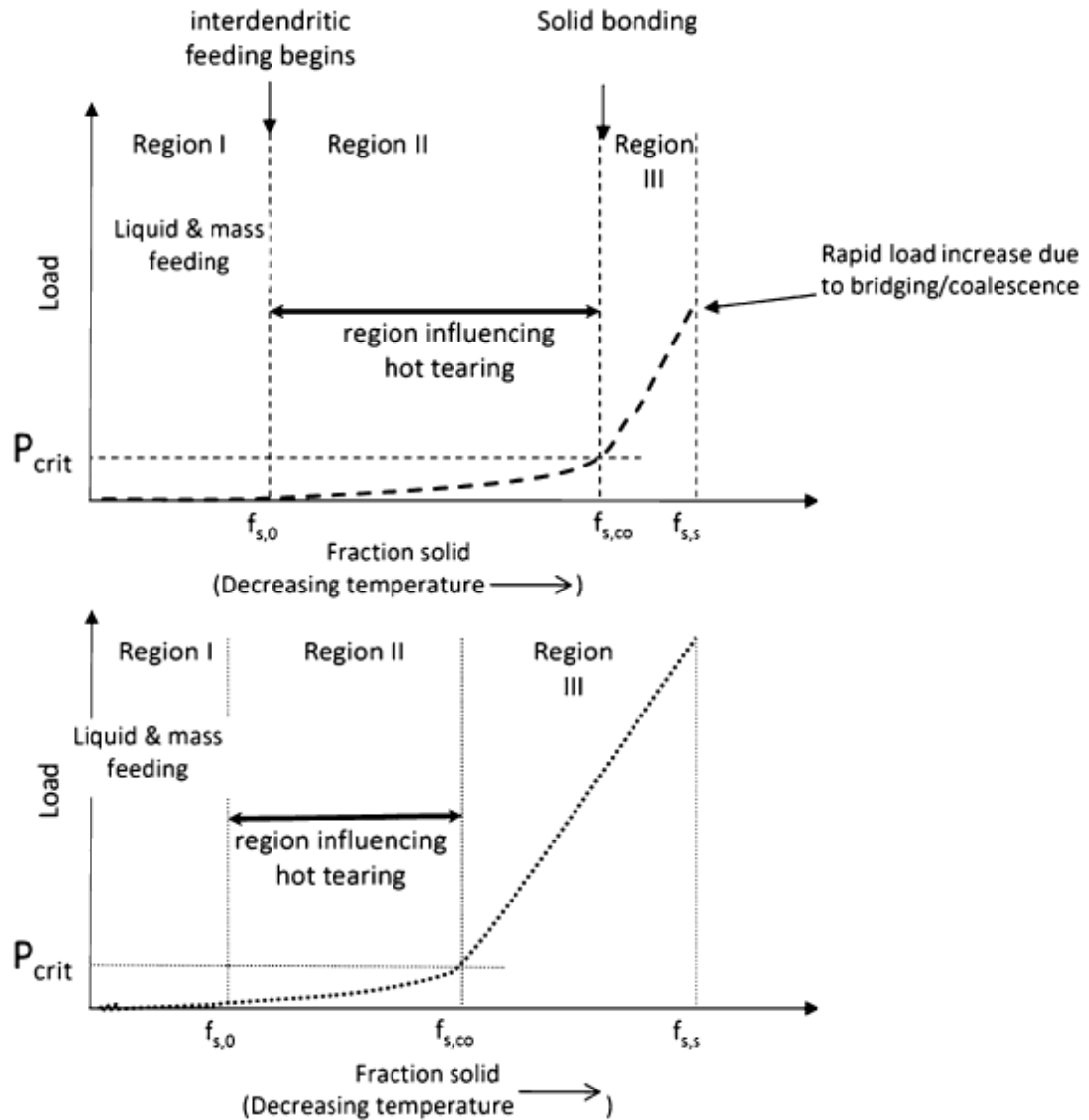
Figure 2.11: Schematic developed by Sweet et al. to explain the load-fraction solid profiles obtained in the hot tearing experiments. The upper schematic represents an alloy with a lower Fe content than the bottom schematic [19].

Puncreobutr et al. [48] also studied the influence of Fe-rich intermetallic phases on defects (hot tearing and pores/voids) formed during the solidification process of Al-Si-Cu alloys. Using an X-ray tomographic microscopy, in situ solidification and in situ semi-solid deformation experiments, carried out on A319 alloys with two Fe levels of 0.02 wt% and 0.06 wt%. It was found that a high fraction of β-intermetallic phases blocks the interdendritic channels, reducing permeability and helping on the formation and growth of pores as well as changing its morphology, which can promote the hot tearing initiation. Their results showed that the alloy with 0.06 wt% Fe and consequently higher volume fraction of the β- intermetallic phases had the internal pores near the fracture surface, and shaped flatter and more aligned with the β-intermetallic phases than that observed in the alloy with 0.02 wt% Fe. These changes in the pore shape resulted in a higher concentration of strain and weaker mushy zone, which could have resulted in an increase in HTS [48].

Liu et al. [48] performed a study with A206 (Al-Cu) alloys in order to understand the influence of Fe-intermetallic phases. Two A206 alloys were cast with dominant Fe-rich IMPs, one being the platelet β-Fe and the other α-Fe. Results showed that cracks can initiate and propagate easier along the platelet β-Fe and the tensile stress increases much faster with displacement when the alloy has a high fraction of platelet β-Fe, which indicates a higher hot tearing susceptibility. Their experiments also showed that the liquid can move more freely with the α-Fe and that platelet β-Fe can block the liquid feeding [48].

2.2.1.1. *Solidification of Al-Zn-Mg-Fe-(Ti) alloy*

This section will discuss some of the general solidification characteristics of the Al-Zn-Mg system and the newly developed alloy Al-Zn-Mg-Fe-Ti. This new Al alloy was developed

from the family of the AA7xxx (Al-Zn-Cu-Mg) alloy to enable structural automotive cast components that would potentially replace several high-density iron-based components.

Al-Zn-Mg alloys have been used in the transportation industry because of the demand for low weight materials. Additions of Zn and Mg have been used for alloy hardening due to their high solubility in aluminum, which contributes to the development of better tensile strength than in pure Al [49]. However, even with Zn and Mg addition, the Al-Zn-Mg alloys still has a low castability and mechanical properties that make them not suitable for structural casting. During the solidification of the Al-Mg-Zn alloys, the primary Al phase microstructure is a dendritic network formed due to the solute rejection taking place ahead of the solid/liquid interface and which forms Zn and Mg intermetallic phases [41]. Most Al-Mg-Zn alloys are formed with 3-8 wt% Zn and 0.3-3 Mg wt%, with a maximum ratio Zn:Mg ≈ 2.8 [49]. Due to its poor castability and poor mechanical properties, elements, such as Cr, Mn, Cu, Fe and/or Ti can be added to some Al-Mg-Zn alloys in this family to improve the mechanical properties and cast quality and consequently hot tearing resistance.

The new alloy was developed having the Al-Zn-Mg system as a base and aiming to maximize the solute dissolution in the primary Al phase while having less than the maximum solubility levels of the primary alloying elements in equilibrium conditions [41]. Figure 2.12 shows the transient solid fraction as a function of temperature during the solidification of the Al-Zn-Mg alloy, with and without Fe addition simulated on Pandat[1] software using the Scheil-Gulliver solidification paradigm. Additions of Fe into the Al-Zn-Mg system promoted a reduction of the liquidus temperature and in the solid fraction at

---

[1] Computherm LLC, Madison, WI, USA

any given temperature. Further, the freezing range decreases from 119°C (647.99°C to 529.04°C) without Fe addition to 87 °C (642.97°C to 555.77°C) with Fe addition. which directly influences on the HTS. According to Li et al. [31], having a larger freezing range would cause the alloy to spend a longer time in the vulnerable stage, which would result in a higher HTS [31]. In summary, the thermodynamic changes result in a considerable decrease in the HTS of this alloy.
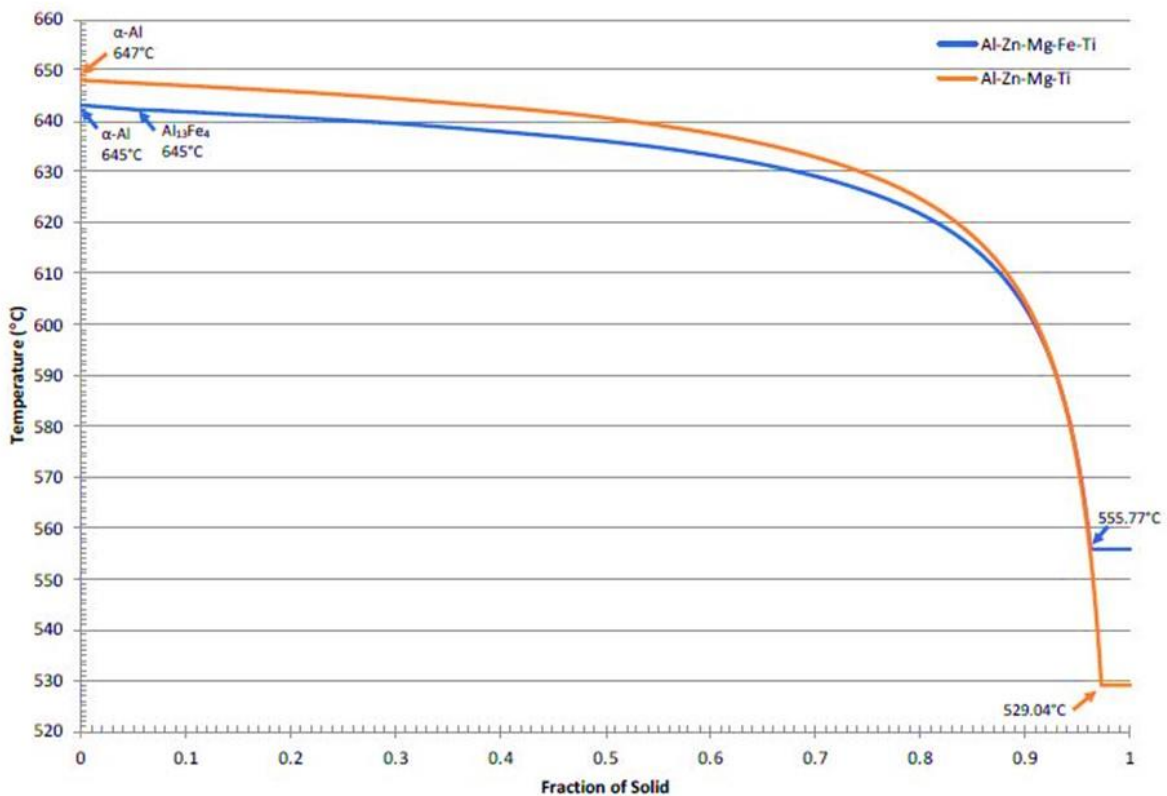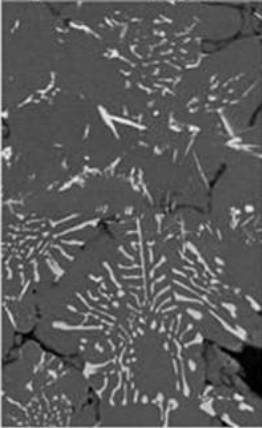
Figure 2.12: Transient solid fraction as a function of temperature obtained by thermodynamic simulation using the Scheil-Gulliver paradigm for solidification in Pandat[2];

28

However, iron additions can be very harmful during the solidification process depending on the type of intermetallic phases formed. Table 2.1 presented on Zhang et al. [42,50] work shows the different types of Al-Fe intermetallic phases that can form during the solidification process depending on the thermal gradients [41,42,50].

Table 2.1: Composition, structure and morphology of the Al-Fe intermetallic phases that can form during solidification of the alloy Al-Mg-Zn-Fe [41,42,50].

Fe based IMP [2,3]	Crystal Structure	Favourable Cooling Rate for Evolution	Stability	Morphology
θ $Al_{13}Fe_4$	C-centered monoclinic	< 3ºC	Stable	
Al_6Fe	C-centered orthorhomic	10-20ºC	Metastable	
Al_mFe $m \rightarrow 4\ to\ 4.4$	Body centered tetragonal	> 20ºC	Metastable	

In the Al-Zn-Mg system, the intermetallic Fe-rich phase $Al_{13}Fe_4$ is formed when there a cooling rate <3°C (as shown in Table 2.1) has a plate format microstructure, as shown in Figure 2.13(a). This IMP can increase the HTS due to its plate shape format that can cause a blockage and prevent the liquid feeding into the shrinkage and local stress areas. However, according to Wu's work [41], when there are high thermal gradients (>10°C) (as shown in Table 2.1), Al and Fe can form specific non-equilibrium intermetallic phases such

as Al_6Fe and Al_mFe (m=4 to 4.4), which could decrease HTS on this alloy. These metastable phases have a feather shape microstructure as shown in Figure 2.13(b), which can increase the fluidity of the liquid between the grains and consequently reduce HTS.

(a)   (b)
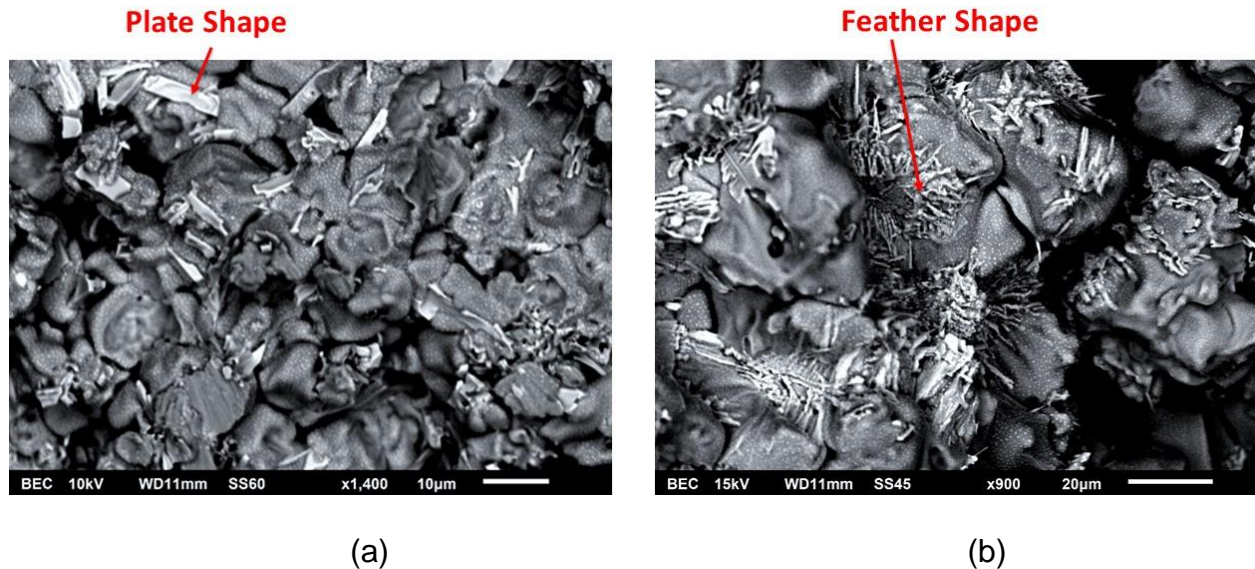
Figure 2.13: Different types of IMP formed during the solidification process: (a) $Al_{13}Fe_4$, Please shape microstructure formed in at the hot tear surface (b) Al_6Fe and Al_mFe, Feather shape microstructure formed in the bulk of a top hat cast by HPDC process.

Titanium additions in the form of Al-5Ti-1B to the Al-Zn-Mg-Fe alloys would result in refinement of the primary phases grains and would help to change the morphology of the primary phase grains from dendritic to uniform equiaxed as presented in the Figure 2.14.

(a)   (b)
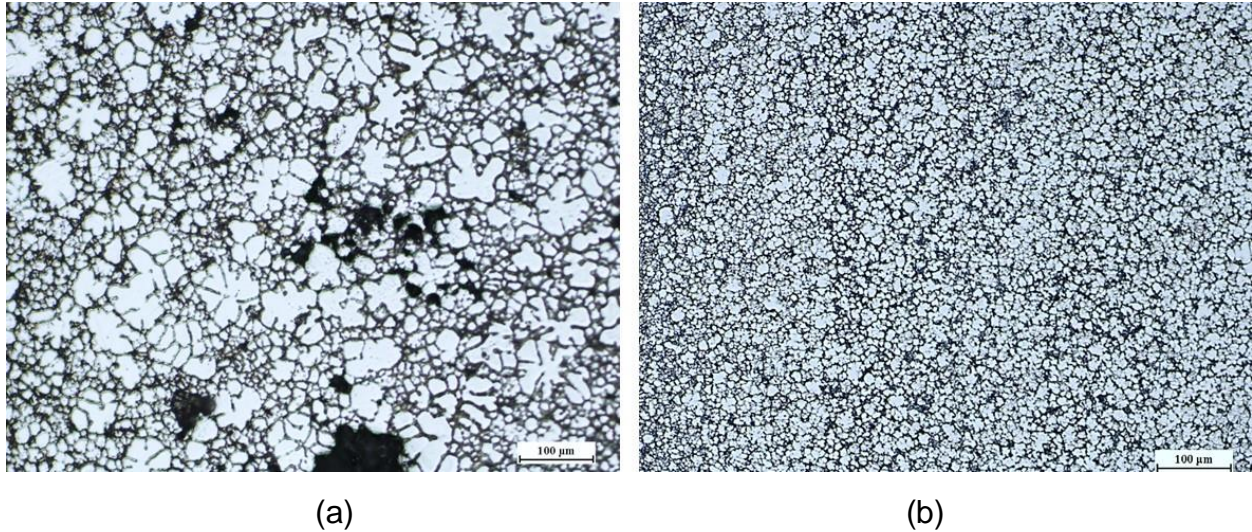
Figure 2.14: Difference in the microstructure top hat cast by HPDC process (a)

dendritic (b) equiaxed.

Furthermore, Al and Ti evolve as a trace-level primary phase (Al$_3$Ti), which facilitates the nucleation of the α-Al primary phase during the solidification. The grain refinement and the changes in the morphology could prevent HTS. However, the high addition of Ti (>0.03%) could affect the alloy properties and even increase the HTS as stated by Warrington and McCartney [26]. The newly developed alloy is a hypoeutectic iron content as to be observed in Figure 2.15, which shows the phase diagram for the Al-Zn-Mg-Fe-Ti with increasing Fe wt% as a function of temperature and all the equilibrium phases that may evolve during the solidification process. The phase diagram was made using the Pandat[3] software.

---

[3] Computherm LLC, Madison, WI, USA

31
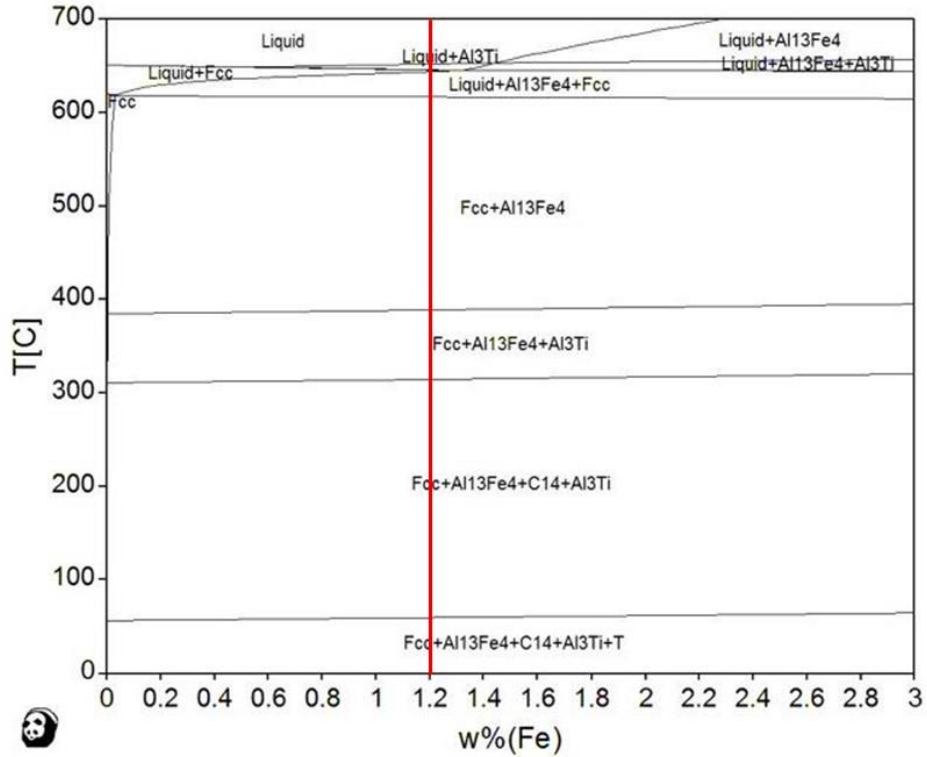
Figure 2.15: The simulated Al-Fe phase diagram of the Al-4Mg-1Zn-1.2Fe-0.1Ti alloy, with all IMP formed during the solidification. The red line shows the percentage in wt% of Fe of the alloy.

2.2.2. Mould preheat temperature

Mould preheat temperatures directly control the cooling rate of the solidifying alloy, which influences the resultant casting microstructure and consequently in the HTS. Bichler et al. [51] analyzed the influence of mould preheat temperature with the range of 140 °C to 380 °C and used a constant melt pouring temperature of 700°C for the Al-Mg alloy, AZ91D. Results showed that mould preheat temperature has a significant effect on HTS; increasing the same lead to decreasing HTS [51].

He at al. [17], through experiments and simulations, showed that the higher mould preheat temperatures lead to lower thermal gradients at the growing solid-liquid interface leading to a suppression of the columnar growth, resulting in a decreased HTS [17]; Figure 2.16 presents a snapshot of the results from this work.
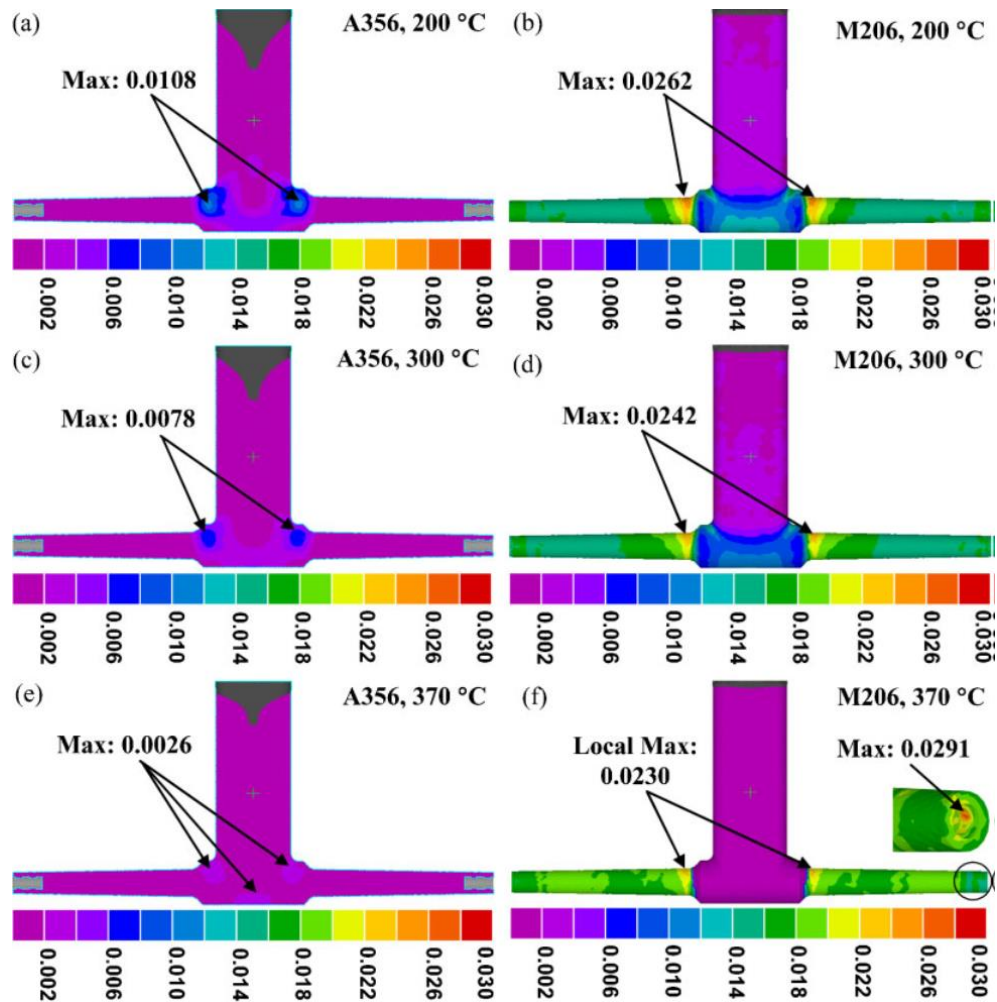
Figure 2.16: Hot tearing indicator for A356 (a, c, e) and M206 (b, d, f) cast in steel mould with three different mould preheat temperatures and pouring temperature equal to 750 ºC. The HTS was evaluated using a proposed model. The coloured gradation scale in each image is the HTS indicator number [17].

Li et al. [52] studied the influence of mould preheat temperature on hot tearing. The experiments were carried out on a constrained rod mould that measures load/time/temperature during solidification using two different alloys, a modified Al-Cu alloy 206 that has a high hot tearing tendency (alloy M206 - no Ti was added) and A356 alloy that has a low hot tearing tendency. The tests were conducted at a pouring temperature of 750°C (M206) and 715°C (A356) both 100°C superheat and mould preheat temperatures of 200,300 and 370°C. They found that lower mould preheat temperature results in a higher hot tearing tendency. For both alloys, the load and displacement increased more rapidly for lower mould temperatures. Experiments with alloy A356 showed that the higher the mould preheat temperature, the higher the load and displacement at the end of solidification and no crack was observed. Alloys M206 showed a similar trend. However, the load development during the solidification of M206 samples was interrupted at some points for all three mould temperatures, which proves the presence of a crack and hence, resulted in a lower load at the end of the solidification. In summary, increasing the mould temperature decreases substantially the hot tearing susceptibility and linear contraction in the alloy M206 as shown in Figure 2.17 [52].
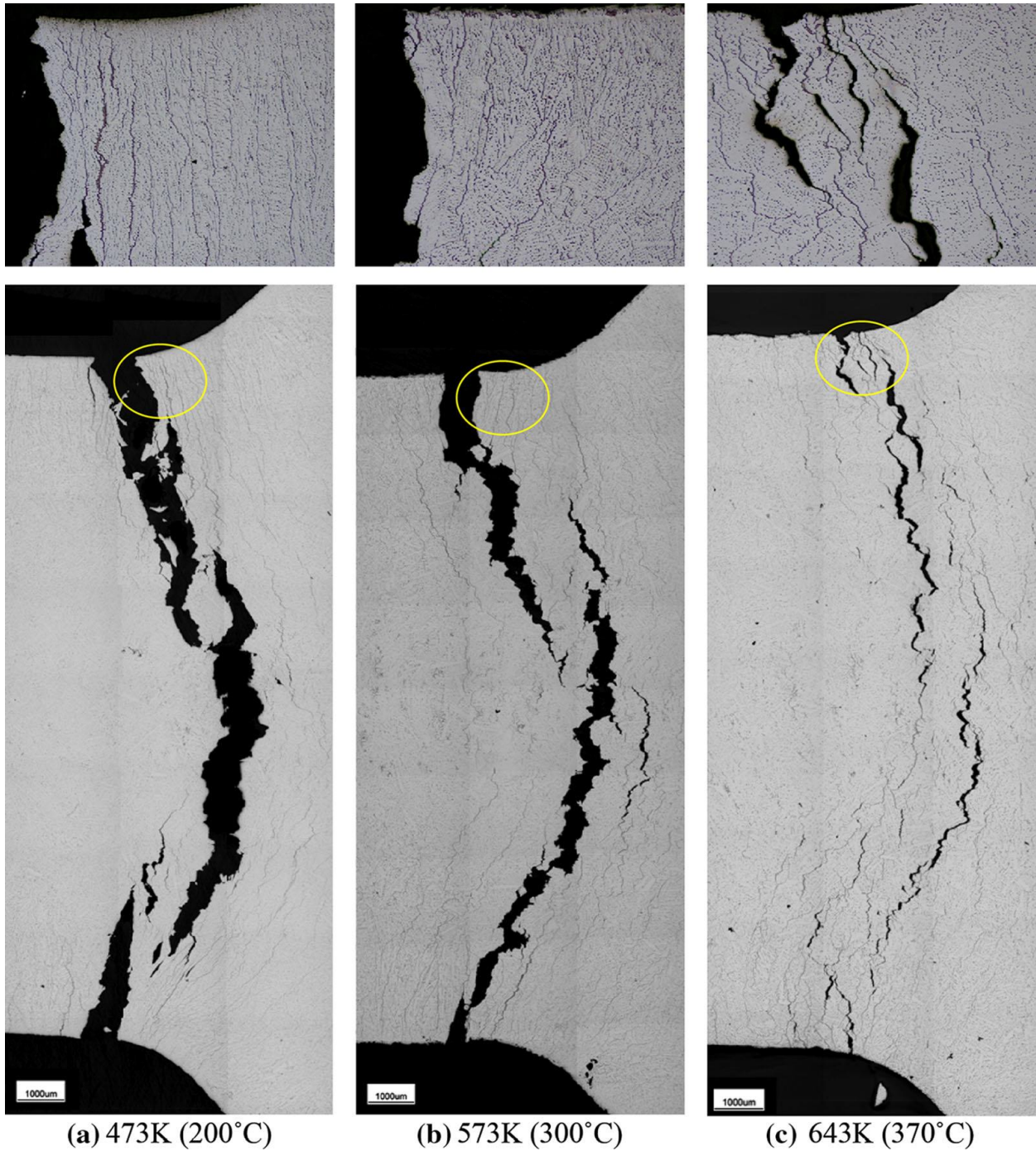
Figure 2.17: Optical micrographs of hot tears in the neck region of M206 at mould preheat temperature: (a) (200°C), (b) (300°C), (c) (370°C) and pouring temperature at 750°C [52].

2.2.3. Pouring Temperature

The pouring temperature has been the main topic of study among many researchers that analyze parameters that can influence hot tearing. Over the years, foundry researchers have had divided opinions about whether the pouring temperature increased or decreased HTS, since contradicting results have been featured in the literature [51,53–56].

Clyne and Davies [32] tested various initial melt pouring temperatures while varying Mg composition and it was observed that the HTS decreases when the initial pouring temperature increased, as shown in Figure 2.18; the relationship between HTS and Mg content in the alloy is more complex, wherein, within the regime of solubility of Mg in primary Al, the HTS showed a peak value that moved to higher values of Mg in the alloy with decreasing melt pouring temperatures [32]. However, Bichler et al. [51] experimented on an Al-Mg alloy (AZ91D) varying the pouring temperature from 680°C to 720°C and it was found that the pouring temperature did not have an appreciable effect on HTS [51].
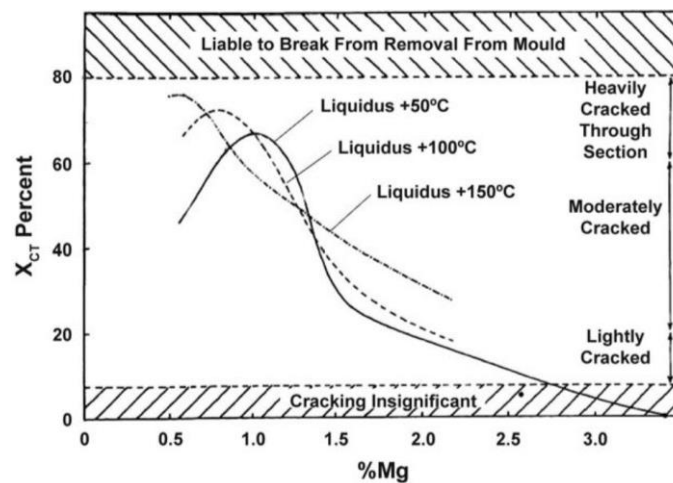
Figure 2.18: Variation of cracking fraction of Al-Mg single-phase alloys as a function of initial melt pouring temperature and solute content [32].

He et al. [17] and Li et al. [52] studied the influence of pouring temperature on hot tearing in the M206 alloy using the constrained rod mould. Both analyses conducted the same tests using pouring temperatures of 700, 750 and 800°C. It was found that as the pouring temperature increases, the severity of hot tearing in the alloy M206 increased slightly [17,52]. According to Li et al. [52], the influence is not as significant as that of mould temperature possibly due to a decrease in the ability of the alloy structure in accommodating the local stresses formed during thermal contractions and to an increase in the liquid film thickness between the grains, which results in an increase in the hot tearing tendency [52].

2.2.4. Hot Tearing Models

There have been several attempts to develop a predictive model to define HTS; some of the salient ones are discussed below.

2.2.4.1. *Prokhorov's Criterion*

In 1962, Prokhorov [57] developed a hot tearing model that was based on the configuration of a solidifying body. It was proposed that during solidification, the metallic alloys experience a low-ductility range during the solidification process, called the brittle temperature range (BTR). The lowest fracture strain in this range was termed D_{min}. The actual strain in the solidifying body (ε_{app}) was determined by the solidification shrinkage/contraction and the geometrical configuration and given by Equation 2.1:

$$\varepsilon_{app} = \varepsilon_{int} - \varepsilon_{free} \qquad\qquad (2.1)$$

where, ε_{int} is the strain resulting from the restricted shrinkage and the thermal stresses as a result of the configuration of the solidifying body and ε_{free} is the free solidification shrinkage strain. The reserve of hot tearing strain in the semi-solid state ($\Delta\varepsilon_{res}$) was written as Equation 2.2:

$$\Delta\boldsymbol{\varepsilon}_{res} = \boldsymbol{D}_{min} - (\boldsymbol{\varepsilon}_{int} - \boldsymbol{\varepsilon}_{free}) \tag{2.2}$$

The expression was divided by BTR, as shown in Equation 2.3:

$$\frac{\Delta\varepsilon_{res}}{BTR} = \frac{D_{min} - (\varepsilon_{int} - \varepsilon_{free})}{BTR} \tag{2.3}$$

Since $\dot{\varepsilon} = \frac{\Delta\varepsilon_{res}}{BTR}\dot{T}$ where $\dot{\varepsilon}$ is strain rate and $\dot{T}$ is the cooling rate, then the previous expression results in Equation 2.4:

$$\dot{\boldsymbol{\varepsilon}}_{res} = \dot{\boldsymbol{\varepsilon}}_{min} - \dot{\boldsymbol{\varepsilon}}_{free} - \dot{\boldsymbol{\varepsilon}}_{app} \tag{2.4}$$

There is a maximum strain rate that the semisolid material could endure without fracture during solidification. If $\dot{\varepsilon}_{res} \geq 0$ or $\dot{\varepsilon}_{min} - \dot{\varepsilon}_{free} \geq \dot{\varepsilon}_{app}$, then a hot tear would occur in the solidified body [57–59].

2.2.4.2.   Novikov's Criterion

In 1966, Novikov [30] performed a study to analyze the effect of chemical composition on the hot tearing of non-ferrous alloys in binary and multicomponent systems based on aluminum, magnesium and copper. Novikov's model proposes a "reserve of plasticity" (p_r) in the solidification range that can be obtained by the integration of the difference between the elongation to failure (ε_{fr}) and linear shrinkage (ε_{sh}). The interval of integration was carried out between the coherency and solidus temperatures, which was called "brittle"

(or "effective") temperature range (ΔT_{br}) by Novikov. The hot tearing susceptibility, p_r, was proposed as Equation 2.5:

$$p_r = \frac{1}{\Delta T_{br}} \int_{T_{sol}}^{T_{coh}} \left(\varepsilon_{fr} - \varepsilon_{sh} \right) dT \qquad (2.5)$$

where, T_{coh} is the coherency temperature and T_{sol} is the solidus temperature. In order to determine the HTS, the strain due to linear shrinkage was computed with the FEM in the semisolid region and the fracture strain in the semi-solid region was obtained from the experimental data [30,59].

2.2.4.3.   Feurer's Criterion

In 1977, Feurer [60] developed a criterion for hot tearing that focused on feeding and shrinkage during solidification; hot tearing was caused from a lack of liquid feeding during the solidification process caused by the difficulties of the liquid to flow through the mushy zone to compensate for the continual solidification shrinkage. This model considered two terms: SPV, which indicated the maximum volumetric flow rate (feeding term) through a dendritic network, and SRG that indicated the volumetric solidification shrinkage. According to Feurer's criterion, hot tearing would be possible only if SPV < SRG. SPV could be evaluated using Equation 2.6 and the following Equations 2.7 to 2.10, enabled the calculation of SPV as shown in Equation 2.6:

$$SPV = \frac{f_l^2 \lambda_2^2 P_S}{24 \pi c^3 \eta L^2} \qquad (2.6)$$

$$P_S = P_O + P_M - P_C \qquad (2.7)$$

$$P_M = \bar{\rho} g h \qquad (2.8)$$

$$\bar{\rho} = \rho_l f_l + \rho_s f_s \qquad (2.9)$$

$$P_C = \frac{4\gamma_{SL}}{\lambda_2} \qquad\qquad\qquad (2.10)$$

where,

$\mathfrak{f}_l$ is volume fraction liquid;

λ_2 is secondary dendrite arm spacing;

P_S is effective feeding pressure;

c is tortuosity constant of the dendritic network;

η is viscosity of the liquid phase;

L is length of porous network that is determined as the distance between the locations at coherency and solidus temperature;

P_O, P_M and P_C are atmospheric, metallostatic, and capillary pressure, respectively.

$\bar{\rho}$ is average density of the mush;

g is gravity constant;

h is distance to the melt surface;

ρ_l and ρ_s are densities of liquid and solid, respectively;

$\mathfrak{f}_l$ and $\mathfrak{f}_s$ are volume fractions liquid and solid in the dendritic network, respectively;

γ_{SL} is solid-liquid interfacial energy.

SRG was caused by the density difference between solid and liquid phase, and the shrinkage velocity, as shown in Equation 2.11:

$$SRG = \frac{\partial lnV}{\partial t} = -\frac{1}{\rho}\frac{\partial \overline{P}}{\partial t} \tag{2.11}$$

where V is a volume element of the solidifying mush with constant mass and t is time. The data used for computing HTS using Feurer's criterion are shown in Table 2.2 [18,59,60].

Table 2.2: Data used for computing the HTS by Feurer's criterion.

Variables	Value
ρ_l	2328 kg/m^3
ρ_s	2570 kg/m^3
λ_2	10µm
c	4.6
η	0.0013 Pa.s
γ_{SL}	0.84N/m

2.2.4.4. Clyne & Davies's Criterion

In 1979, Clyne and Davies [27] developed a hot tearing model to calculate the cracking susceptibility coefficient (CSC) based on the time that the strain accommodation would happen due to four salient phenomena: solid movement, liquid movement, interdendritic separation and interdendritic coexistence, which would translate to a liquid fraction. Their model focused on the solidification time at the last stage of the freezing range, the mushy zone. During this stage, the structure would be most vulnerable to cracking due to a lack of liquid mass feeding in the regions where strains developed from shrinkage. Their model defined cracking susceptibility coefficient (CSC) by the ratio of the vulnerable time period when hot tearing may occur (t_v) and time available for the stress-relief process (t_R) when the mass and interdendritic feeding would occur. It was proposed that the stage most susceptible to hot tearing would be the interdendritic separation with a fraction of solid between 0.9 and 0.99 and the stress could be released at a fraction of solid between 0.4 and 0.9 [18,27,61]. The crack susceptibility coefficient (CSC) was defined as follow:

$$CSC = \frac{t_V}{t_R} = \frac{t_{0.99} - t_{0.9}}{t_{0.9} - t_{0.4}} \qquad\qquad (2.12)$$

Where $t_{0.99}$, $t_{0.9}$, and $t_{0.4}$ correspond the time when the local solid fraction (fs) is 0.99, 0.9, and 0.4, respectively [27].

Clyne and Davies [62] performed experiments with different alloys and the experimental results were compared with the theoretical results obtained from their model calculation. Both the prediction and the experimental results follow the so-called Λ (Lambda) shape. The model also showed that the amount of liquid available to feed the shrinkage and crack regions would be a critical factor on the CSC. According to the experiments, the solute elements in an Al alloy would have a decreasing influence on the hot tearing susceptibility in this order: Sn, Si, Cu, Mg and Zn [62].

However, there are a few limitations with Clyne and Davies' model, such as a fixed equation is used in the model to calculate the cooling rate and the model does not take into consideration the influence of the initial mould preheat temperature. Additionally, the calculation used fails to consider the role of microstructure and material properties on the HTS. Given these limitations to their model, the measurements for CSC would not be affected by the casting speed or by the location of the hot tearing and this is problematic because microstructure morphologies, as well as mechanical properties, play a critical role on HTS in the semi-solid state [61]. However, when the $t_{0.4}$ and $t_{0.9}$, which were assumed as constants for the time to reach dendritic coherency temperature (T_{coh}) and grain coalescence temperature ($T_{coalesce}$), could be changed to a variable that when uniquely determined from the solidification conditions such as the rate of heat extraction and morphology of the primary Al phase, might strengthen the model by circumventing the above-mentioned limitations.

2.2.4.5.   Katgerman's Criterion

In 1982, Katgerman [63] suggested a model, where the theoretical considerations of Clyne and Davies [27] and Feurer [60] were combined. The model evaluated the hot tearing index (HCS) as follows:

$$HSC = \frac{t_V}{t_R} = \frac{t_{0.99} - t_{cr}}{t_{cr} - t_{coh}} \qquad (2.13)$$

where $t_{0.99}$ is the time when the volume fraction of solid (f_s) is equal to 0.99, t_{coh} is the time when fs at the coherency point, t_{cr} is the time when feeding becomes inadequate and it is defined by using Feurer's criterion and is the time for that SPV = SRG [63].

2.2.4.6.   Rappaz, Drezet & Gremaud's Criterion

In 1999, Rappaz *et al.* [20] developed a model to predict the initiation of hot tears based on the maximum strain rate that the mushy zone can resist. Their model focused on the mushy zone solidification and considered the deformation caused by thermal stresses in the coherent solid network and lack of feeding as the main cause of tear initiation. In the RDG hot tearing criterion, the maximum pressure drop (Δp_{max}) over the mushy zone is established as:

$$\Delta p_{max} = \Delta p_{\varepsilon} + \Delta p_{sh} = \Delta p_c \qquad (2.14)$$

where the terms Δp_{ε}, Δp_{sh} and Δp_c are the pressure drop contributions in the mush associated with the deformation-induced fluid flow, the solidification shrinkage, and cavitation pressure, respectively.

The maximum deformation rate ($\dot{\varepsilon}_{p.max}$) that the mushy zone can sustain before a hot tear nucleate at the root of the dendrites was defined as:

$$\dot{\varepsilon}_{p.max} = \frac{G^2 \lambda_2^2}{180(1+\beta)B\mu\Delta T_0^2} \Delta p_{max} - \frac{v_T G \beta A}{(1+\beta)B\Delta T_0} \qquad (2.15)$$

$$where, A = \frac{1}{\Delta T} \int_{T_{end}}^{T_{mf}} \frac{f_s^2 dT}{(1-f_s)^2}; \; B = \frac{1}{\Delta T} \int_{T_{end}}^{T_{mf}} \frac{f_s^2 F_s(T)}{(1-f_s)^3} dT; and \; F_s(T) = \frac{1}{\Delta T} \int_{T_{end}}^{T} f_s dT$$

and G is the temperature gradient; λ_2 is the secondary dendrite arm spacing; β is the shrinkage factor; μ is the viscosity; ΔT_0 is the solidification interval; Δp_{max} is the maximum pressure drop the mushy zone could tolerate; v_T is the velocity of the isotherms; f_s is the volume fraction of solid; T_{end} is the temperature at which bridging of the dendrite arms between grains occurred, and T_{mf} is mass feeding temperature. Then, the HCS index can be expressed as:

$$HCS = \frac{1}{\dot{\varepsilon}_{p.max}} \qquad (2.16)$$

Δp_{max} is a measure of the hot tearing sensitivity. A criterion for hot cracking is presented by the introduction of a critical cavitation pressure(Δp_c), which for Al-Cu binary alloy is 2kPa. If $\Delta p_{max} > \Delta p_c$, a hot tear would form.

It was also pointed out that the most critical stage that a tear could initiate was when the dendrite arms have not coalesced and bridged yet, and the film of interdendritic liquid is continuous. Experiments with Al-Cu alloys, varying the alloy composition was also carried out and curves Λ-shaped were obtained where the maximum HCS was around 1.3. The model confirmed that the strain rate that causes the hot tear was a function of thermal gradients, permeability, and viscosity. However, the model could be used only for columnar dendrites [20,31,59,61].

2.2.4.7. Lahaie and Bouchard's Criterion

In 2000, a model to predict hot tearing was developed by Lahaie and Bouchard [29]. The model is a physical model that analyzed the fracture stress and fracture strain during the final stages of solidification, using the parameters that would influence the strength of the solidifying structure. The model considered the complete wetting of the solid grains and a semisolid 2D microstructure in the film liquid stage with $h \ll a$ as shown in Figure 2.19 was idealized [29].
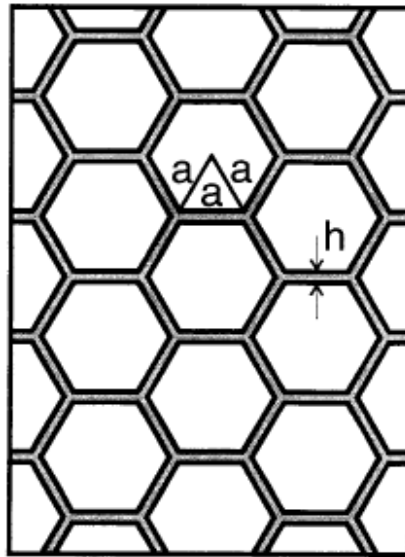
Figure 2.19: Idealized microstructure of a semisolid body in the liquid film stage [29].

Exploiting the hexagonal arrangement from Figure 2.19, where the stress of the structure is 2/3 the stress on each horizontal channel, a fracture criterion was developed to measure hot tearing as shown in Equation 2.17:

$$\sigma_i = \frac{4\eta}{3h}\left(1 + \left(\frac{f_s^m}{1-f_s^m}\right)\varepsilon\right)^{-1} \qquad (2.17)$$

where η is the viscosity, h is the film thickness before deformation, f_s is solid fraction, ε is the accumulated strain and m is the microstructure parameter, which is 1/3 for equiaxed and 1/2 for columnar structure.

Parameters considered to have an influence on the strength of the solidifying structure were analyzed using Equation 2.17. It was shown that the hot tearing was more prone to occur when there was a high fraction of solid ($F_s > 0.95$), as this was the value that the strength in the solidifying structure sharply increased and the fracture strain decreased, consequently decreasing the ductility. Embrittlement was one of the conditions for hot tearing according to this theory. Parameters such as grain shape, the ratio of liquid film thickness to the grain size and interfacial surface energy were shown to have a significant influence on the fracture strength, however, it was showed to have a marginal to negligible influence on the fracture strain. While parameters such as viscosity and isothermal compressibility were shown to not have a notable influence on hot tearing. Although it was proposed that the viscosity does not influence hot tearing, it would play a significant role in influencing the liquid feeding and healing shrinkage voids in the final stages of the solidification that directly determined the HTS of the alloy [29].

2.2.4.8.   He, Sadayappan and Apelian's Criterion

In 2013, he et al. [17] performed a study in a constrained permanent mould equipment, in order to measure displacement, tensile load and temperature during solidification and developed a strain-based model where it was assumed that hot tearing formed due to the growth of stable voids in a ductile and porous solid. The hot tearing indicator (HTI) was defined as the time integration of the void nucleation rate ($\dot{f}_{nucleation}$, as controlled by the

strain field) over the range between the coherency temperature and solidus temperature as shown in the Equation 2.18:

$$\text{HTI} = \int_{\tau_C}^{\tau_S} \dot{f}_{nucleation} d\tau = \int_{\tau_C}^{\tau_S} [(2/3)\dot{\varepsilon}^p : \dot{\varepsilon}^p]^{1/2} d\tau \qquad (2.18)$$

where, $\dot{\varepsilon}^p$ is the plastic strain rate, τ_C is the time to reach the coherency temperature at $f_s \cong 0.5$, and τ_S is the time to reach the solidus temperature.

Simulations and experiments were performed using two different alloys, M206 (High tendency to hot tearing) and A356 which three (3) different pouring temperatures and three (3) different mould preheat temperatures were used in two (2) different types of mould. Besides, parameters, which could influence the solidification process, were calculated based on the type of alloy and mould material used, such as the assumption of linear thermal expansion coefficient and heat transfer coefficient. The calculated displacement and tensile load obtained in the simulations were compared with the measured data in the experiments. It was found that the computed cooling curves and cooling rates were similar to the measured curves for both alloys. The computed displacement curves, although similar in shape with the measured displacement curves, the latter was quantitatively higher than the former, because in the simulations, the mould deformation was not included and in reality, the mould deformation occurred. Further, M206 had a larger displacement because it had a higher thermal expansion coefficient value than that A356 alloy. The tensile load curves did not show a good fit between the calculated value and measured value, the former was higher than the latter because was not possible to carry out the simulation of the crack formation. However, since M206 had a high tendency to crack, both results agree to M206 having lower values of tensile

strengths. When a crack initiated, the effective area of the solidification cross-section decreased, thus, reducing the load transferring ability [17].

2.2.5. Transient Solid Fraction Evolution during Solidification

Computed-aided cooling curve analysis (CA-CCA) could be a very helpful tool to study hot tearing and have been widely used in the metalcasting industry to obtain several processing and material parameters, such as alloy composition, prediction of transition temperatures, amount of different phases, latent heat and dendrite coherency.

As shown by many studies [38,64], one of the main causes of hot tearing in alloys is the lack of liquid feed to compensate for solidification shrinkage and typically occurs when the solid fraction is at high values. Therefore, many models have been developed in order to calculate the correct fraction of solids during solidification, such as Linear, Lever Rule, Scheil-Gulliver model, Grain Nucleation, Differential Scanning Calorimetry (DSC), Newtonian Heat Balance and Fourier Analysis.

The linear model is extremely simple with no theoretical basis and it assumes that the latent heat diffusion varies linearly in the freezing zone. Lever Rule model is dependent on the equilibrium solidification, which evolves very slowly and assumes that the solid and liquid phases are present in the mushy zone in thermodynamic equilibrium and that the solute phase redistributing at the solid-liquid interface would be completely diffused in both the solid and liquid phases; moreover, the fraction of solids is determined by the lever rule assuming that the liquidus and solidus lines are straight lines.

The Scheil-Gulliver (S-G) model also depends on the equilibrium solidification assumption couples with complete diffusion of solutes in the liquid but no solute diffusion in the solid

phase. Further, it also considers the liquidus and solidus lines are straight lines. The grain nucleation model uses the grain nucleation law to calculate the fraction of solids, assuming that the grain shape is spherical. In the DSC model, the fraction of solids is determined experimentally by assuming that the heat of melting is independent of the temperature, then, the composition of the solid phase is linearly proportional to the amount of the melted alloy.

The Newtonian Heat Balance model assumes that the temperature field can be considered spatially uniform (zero temperature gradient in the liquid phase) and considers constant sensible specific heat for the alloy (temperature independent. While the Fourier analysis model considers the effect of the thermal gradient during solidification and assumes that the heat transfer happens only by conduction.

Table 2.3 presents the seven different models to calculate fraction of solid with their respective limitations of use in rapid non-equilibrium solidification conditions.

Table 2.3: Summary of seven models of solid fraction [65,66]

Model	Equation	Comments	References
Linear	$f_s = \dfrac{T_{Liq} - T_{Ins}}{T_{Liq} - T_{sol}}$ f_s - solid fraction T_{Liq} - Liquidus temperature T_{Ins} - instantaneous temperature T_{sol} - solidus temperature	• no theoretical basis • extremely simple	[67]
Lever Rule	$f_s = \dfrac{1}{1-k} \cdot \dfrac{T_{Liq} - T_{Ins}}{T_m - T_{Ins}}$ $k = \dfrac{T_m - T_{Liq}}{T_m - T_{Sol}}$ T_m - melting temperature of a pure dominated element in an alloy k - partition ratio	• equilibrium solidification • The solid fraction is defined using the lever rule. • Liquidus and solidus lines are straight lines.	[67]

Scheil	$f_s = 1 - \left[\dfrac{T_m - T_{Ins}}{T_m - T_{Liq}}\right]^{\frac{1}{k-1}}$	• No mass/solute diffusion occurs in the solid phase. • The diffusion in the liquid is perfectly homogeneous liquidus and solidus lines are straight	[67,68]
Grain Nucleation	$f_s = 1 - e^{\left(-\frac{4}{3}.\pi.R^3.N\right)}$ R - average grain radius N - average grain density	• Gains shape is spherical	[67]
DSC	$f_s = 1 - \dfrac{Q(T)}{m.\Delta H}$ $Q(T)$ − Heat absorbed from melting to T m − Mass of sample ΔH − Heat of melting	• the heat of melting is independent of the temperature	[66,67,69]
Newtonian Heat balance	$f_s = \dfrac{\int_{t_{Liq}}^{t}\left[\frac{dT_c}{dt} - \frac{dT_{CBL}}{dt}\right]dt}{\int_{t_{Liq}}^{t_{Sol}}\left[\frac{dT_c}{dt} - \frac{dT_{CBL}}{dt}\right]dt}$ $\frac{dT_c}{dt}$ - the first derivative of the cooling curve (measurement) $\frac{dT_{CBL}}{dt}$ − The Newtonian baseline	• the temperature field is spatially uniform, • constant sensible specific heat for the alloy.	[67,70–72]
Fourier analysis	$f_s = \dfrac{1}{L}\int_{ts}^{t}\left[\frac{\partial Q}{\partial t}\right](t)dt$ L-latent heat Q-latent heat of solidification at t	• heat transfer takes place by conduction only. • Linear temperature gradient	[67,70–72]

CHAPTER 3. *OBJECTIVES AND PROJECT STRATEGY*

The primary goal of this research project is to evaluate the hot tearing susceptibility (HTS) of the single-phase Al-3.8Zn-1Mg alloy using a constrained rod solidification apparatus and assess the influence of Fe additions and grain refinement on HTS. Following this train of thought, the objectives of this project are presented below and Figure 3.1 presents a *birds-eye* perspective of the project strategy that was undertaken in this project.

1. Verify the constrained rod solidification (CRS) experiments for the study of hot tearing susceptibility (HTS). Improve the CRS experiments for repeatability of responses such as transient temperature, transient load, and transient displacement during solidification.

2. Carry out the CRS experiments for three alloys for various rates of solidification through variations of mould preheat temperature.

    a. Al-4 wt%Zn- 1wt% Mg,

    b. Al-4 wt%Zn- 1wt% Mg – 1.2 wt% Fe, and

    c. Al-4 wt%Zn- 1wt% Mg – 1.2 wt% Fe – 0.1 wt% Ti

3. Analyze the response from the CRS experiments and propose a mechanistic understanding of the HTS of the three alloys.
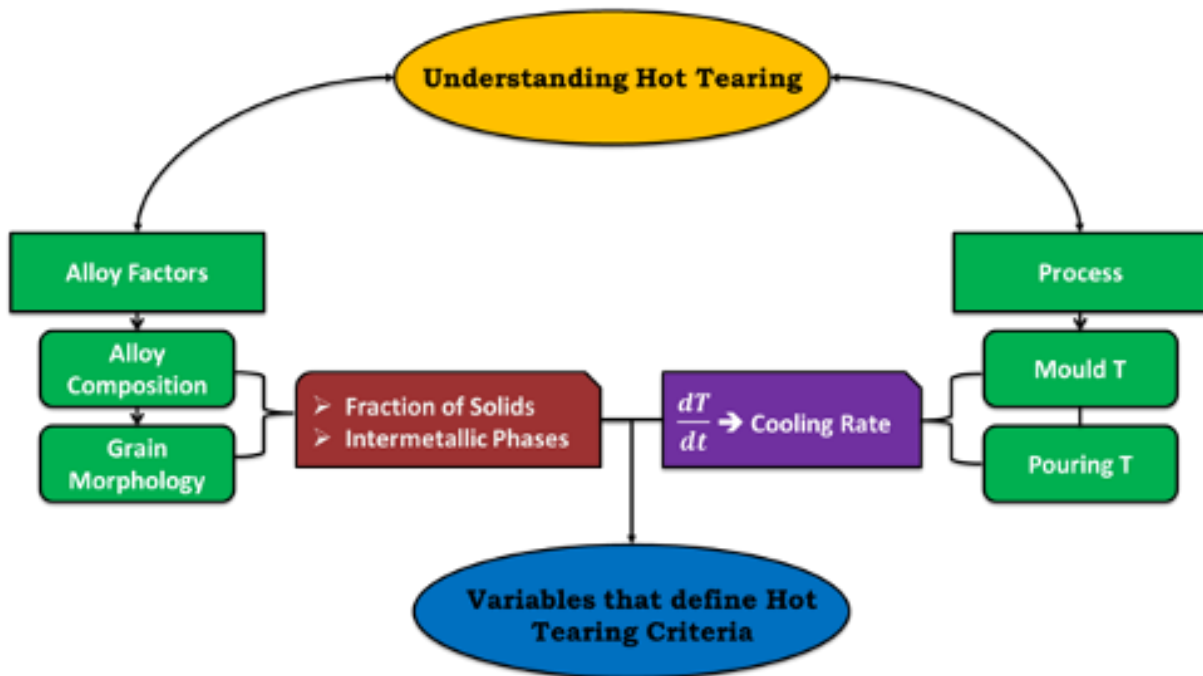
Figure 3.1:   Flow chart showing the overall project strategy

CHAPTER 4. *METHODOLOGY*

This section presents the experimental methodology undertaken in this research, including alloys preparation and melting, castings experiments using the constrained rod solidification apparatus, analyses of the Computerized Tomography (CT) images and microstructure evaluation. The schematic below shows a summary of the methodology used in this study. Figure 4.1 presents the flow chart of the methodology used in this project to achieve the project objectives.
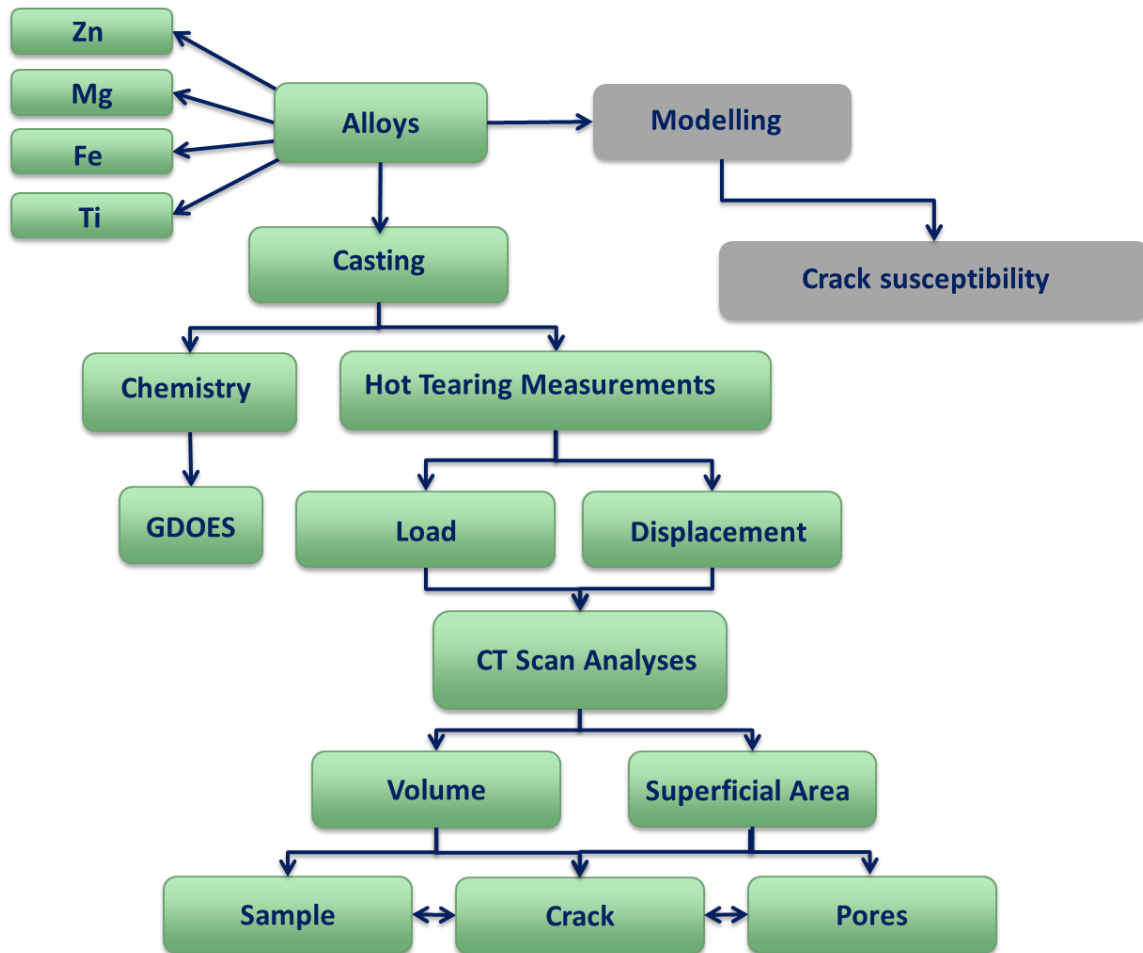
Figure 4.1:   Flow chart of the methodology employed in this project.

4.1.   Casting Experiments

The casting experiments were carried out at the Light Metal Casting Research Centre (LMCRC) at McMaster University. This section describes the hot tearing apparatus, the alloy composition and casting parameters used in the experiments.

4.1.1. Hot Tearing Apparatus

The hot tearing apparatus used in this experiment was provided by the CANMETMaterials in Hamilton, ON, Canada. Figure 4.2(a) shows photographs of the hot tearing apparatus used in this project and Figure 4.2(b) shows the permanent mould cavity geometry.
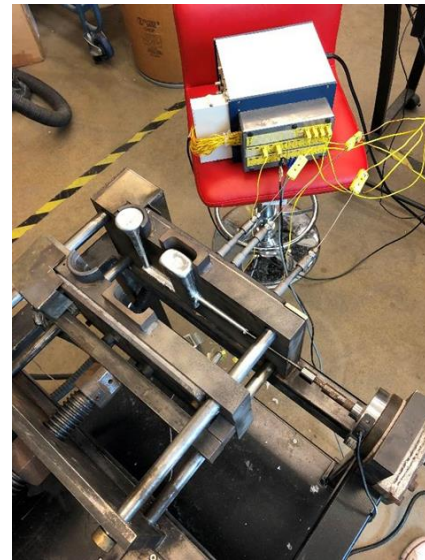
(a)   (b)

Figure 4.2: (a) Constrained Rod Solidification (CRS) experiment apparatus; (b) H13 tool steel permanent mould.

The mould geometry was purposely designed to promote hot tear formation in the casting, and it is made of H-13 steel. The mould cavity consisted of a down sprue of 90 mm height

and 70 mm long, a bulk of 45 mm long and 80 mm height, additionally, a 90 mm long cylindrical arm with the diameter varying from 10 to 12 mm. The casting thickness was 20 mm, except for the arm. The mould cavity geometry and dimensions are shown in Figure 4.3.
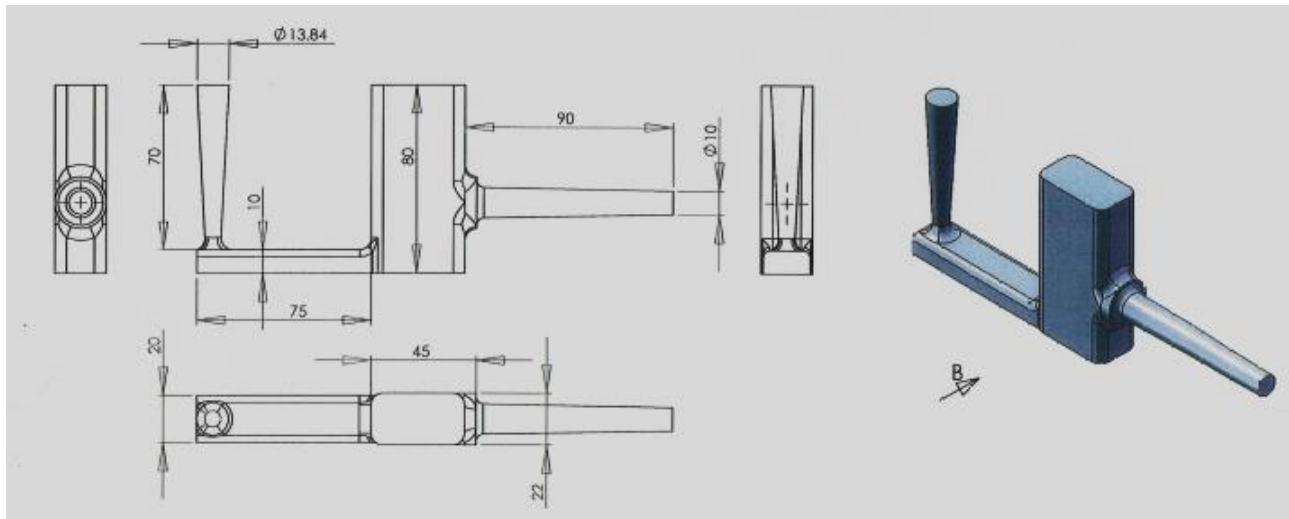
Figure 4.3: Mould cavity geometry and dimensions.

The experiment method used in this study was developed to reproduce the stress and strain in the shape casting processes. The design would be able to measure transient temperature, load and displacement date using thermocouples in the casting, a load sensor and Linear Variable Differential Transformer (LVDT) sensor, respectively. The transient load is measured using a restrained casting rod and transient displacement (shrinkage) with a relaxed sensor rod during the solidification, which contributes to a deep understanding of the behaviour of aluminum alloys during the solidification and the formation of hot tearing. The mould preheat temperature was controlled precisely with four heat strips (two located at each side of the mould) and the mould preheat is monitored

using two independent K-type thermocouples, embedded in the mould, which were located in the bottom face of each side of the mould.

During the experiment, the load was measured using a load cell (Loadstar iLoad Pro Analog 500lb) and the displacement was measured using a linear variable differential transformer (LVDT, Macro Sensors HSTA 750-1000). Both sensors contain a rod that is connected to the end of the arm in the solidifying sample. The rod in the LVDT is unrestrained and can move horizontally while the rod in the load cell is constrained/restrained, causing resistance in the metal during the solidification, which would result in loading the casting, caused by the solidification shrinkage and akin to a uniaxial tensile test process. The increase in stress in the casting could result in hot tears in the sample.

The temperature in the experiment was measured using three K-type thermocouples, it was inserted in the mould at specific locations (as shown in Figure 4.5) such that the thermocouple tips were in the middle section of the casting location. The sensors and thermocouples were connected to a National Instrument System SCXI-1000 terminal block, which records the data through a computer. The data is generated in Volts (V) and it is acquired from the terminal block using a software called LabVIEW (DASYlab). Figure 4.4 shows the load and displacement sensor as well as the thermocouples' positions in the mould.
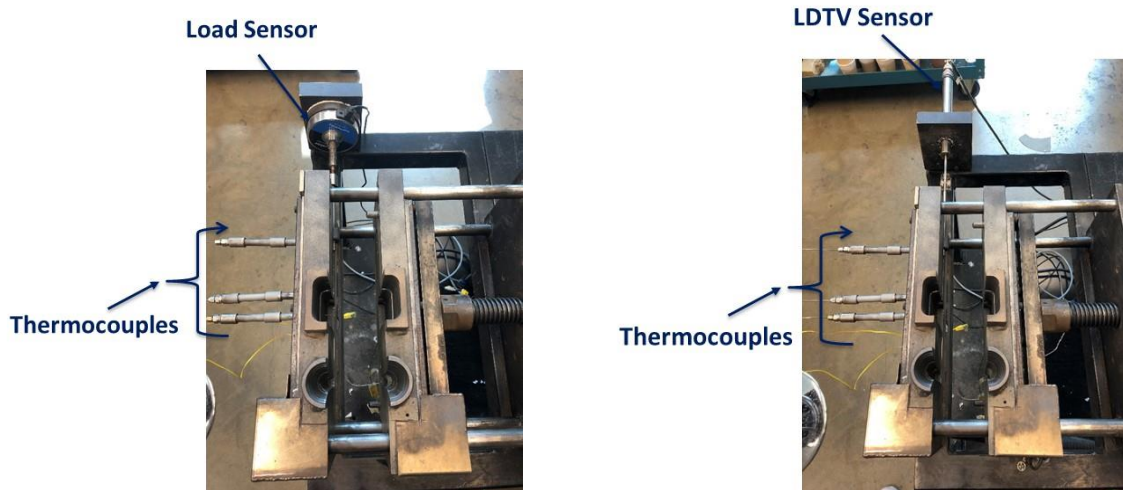
Figure 4.4: Thermocouple positions and (a) Load sensor and (b) Displacement sensor positions.

Figure 4.5 shows the position of the three thermocouples in the sample; the first one was in the bulk of the casting (*TC1*), the second one was positioned at the beginning of the arm close to bulk (*TC2*), where the propensity for hot tearing would be maximum and the third one was located at the end of the cylindrical arm and close to the load/displacement sensor rods (*TC3*).
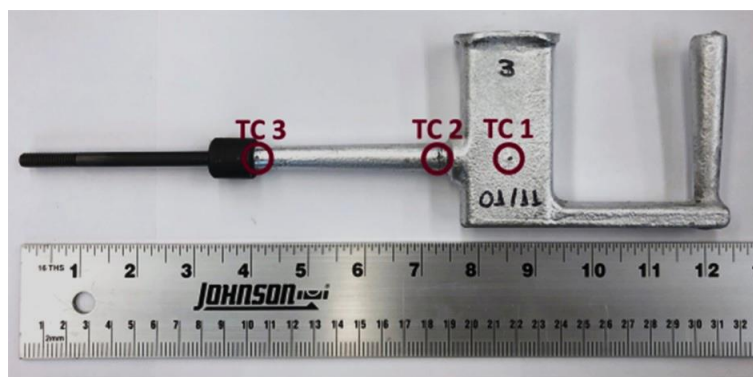
Figure 4.5: The position of thermocouples in the casting sample.

4.1.2. Calibration of Load and LVDT sensor

The load sensor was calibrated by a company, specialized in load sensors calibration and the calibration result is presented in Equation 3.1, where V is the measured load data in mV and the load evaluated is the force acting on the sensor from solidification shrinkage.

$$\textbf{Load (lb) = (144.3880) V} \hspace{3cm} \textbf{(4.1)}$$

Since the results from the LVDT displacement sensor were obtained in mV, it was necessary to carry out the calibration of the sensor to obtain the displacement in units of lengths.

The displacement sensor was calibrated using image analyses of static photographs of the rod in different positions from a varying and predefined set of voltage values. The photos were taken using a calibrated camera on a tripod and the images analyzed using the ImageJ software. Figure 4.6 shows examples of the pictures taken to calibrate the LVDT displacement sensor and Figure 4.7 shows the calibration curve obtained.
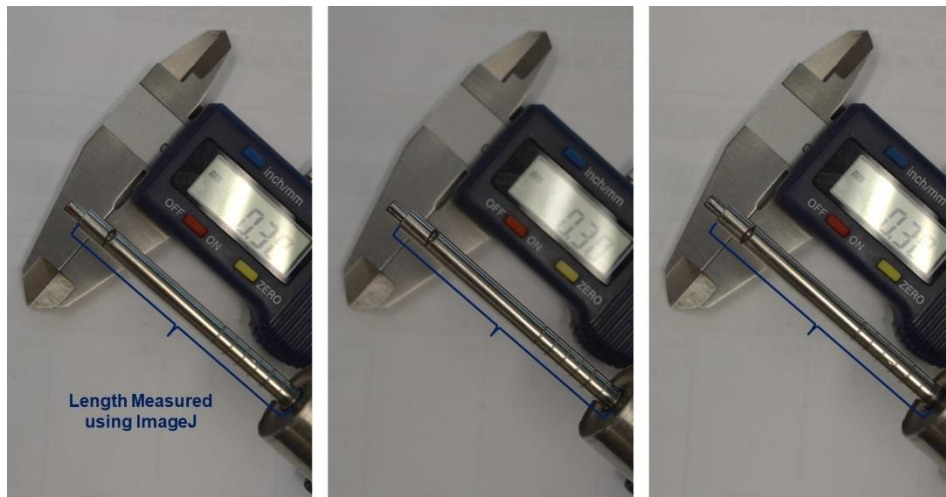
Figure 4.6: Typical photographs used in the displacement sensor calibration.
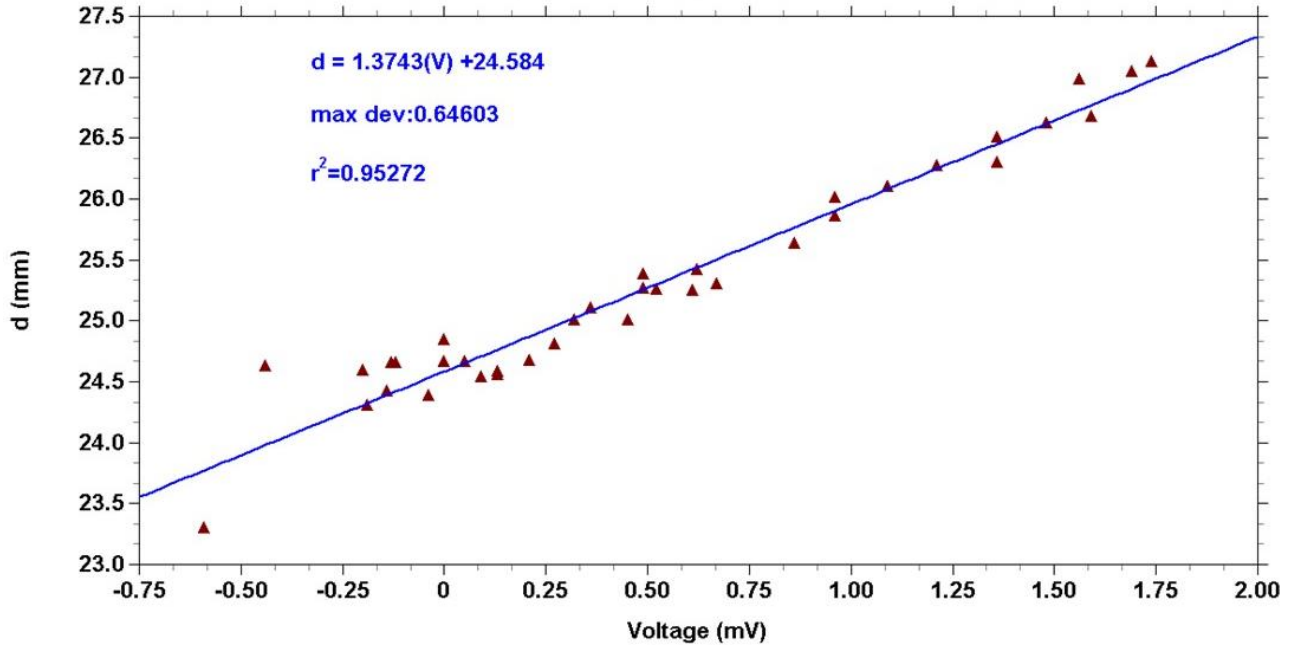
Figure 4.7: Displacement calibration curve for the LVDT sensor.

Aiming to have the lowest margin of error in the CRS experiments, the load rod and displacement rod (point of contact with melted alloy) were made of Titanium, which is a material with very low thermal expansion. This way, the results obtained in the experiment would have a very low influence of the thermal expansion of the rods and coupled with the margin of error from the calibration curves, the errors would still remain minimal.

4.1.3. Alloys Composition

In the first part of the experiments, the aluminum casting alloys A356 and B206 were selected as reference alloys used in verifying the CRS experiment apparatus to ensure repeatability of the transient responses. The alloy A356 is cast alloy with no tendency to hot tear, while, the B206 has a high tendency to hot tear; commercial ingots of both alloys were used in this part of the study.

In the second part of the experiments, three different compositions were critically studied for hot tearing susceptibility using the CRS experiments. The alloys were prepared using commercial pure Al (P0404), and Al-50 wt%Mg, Al-96 wt%Zn and Al-90 wt%Fe and the grain refiner Al-5 wt%Ti-1 wt%B. The alloys used were prepared using an electric resistance furnace and the melt was degassed with argon using a rotating impeller degasser, with an Ar gas flow rate of about 6 L/min, rotating at about 250 to 300 RPM for 30 minutes before pouring it into ingots.

The chemical compositions of the alloys in the experiments were measured using a Glow Discharge Optical Emission Spectroscopy (GDOES) equipment. The samples were cast during the alloy preparation stage, using a copper mould for rapid solidification. The mould used for the sample preparation and the sample obtained are shown in Figure 4.8. The samples were sectioned and prepared using progressive grinding papers with grits of 400#, 600# and 1200#, respectively.

Figure 4.8: Copper mould and typical cast sample for alloy chemistry analyses using GDOES.

4.1.4. Casting Parameters

The samples in the experiments were melted in an electric furnace. Each sample was poured into a fresh ceramic crucible and heated for approximately 30-40 minutes at 900⁰C, prior to pouring into the CRS experiment mould; each melt has the pouring temperature measured using a separate digital K-type thermocouple. A boron nitrate aerosol spray coating was applied to the mould two days before the experiments to allow it to dry thoroughly and a graphite aerosol spray lubricant coating was applied on top of the boron nitrate coating. The mould was preheated to four unique temperatures: 200, 250 and 300 and 350 ±2 °C, before pouring into the mould; the pouring temperatures for all alloys were maintained at 900 ± 5°C. All cast samples were removed from the mould when the measured temperature of the casting temperature reached the mould preheat temperature. After removal from the mould, the samples were visually examined for cracks. During the load and displacement experiments, the thermocouples were placed at the wall of the mould, since the thermocouples placed inside the mould would interfere with the experiments measuring transient load and displacement. The cooling curve data was measured during separate but nearly identical and repeatable experiment procedures. Once the data was acquired separately, the cooling curve, displacement vs. time curve and load vs. time curve were put together and normalized with time, using the date from the location *TC3*.

4.2.   Computerized Tomography (CT) Scan

All the cast samples were analyzed in the CT Scan located in the Department of Health Sciences at McMaster University. The sample was scanned to analyze and measure

external and internal cracks and pores in the cast samples. The CT Scan has the following properties:

- A field of view of 1024 X 1024 pixels;

- Beam → 75 keV;

- Resolution → 30 µm and 360⁰ rotation of beam at 0.3⁰ per scan, which results in 512 different images of the sample for each axes (x, y and z).

- Pixel size: 0.035mm

The CT Scan equipment is presented in Figure 4.9 and the area selected to be scanned (area of HTS) is presented in Figure 4.10.

Figure 4.9: CT Scan equipment.
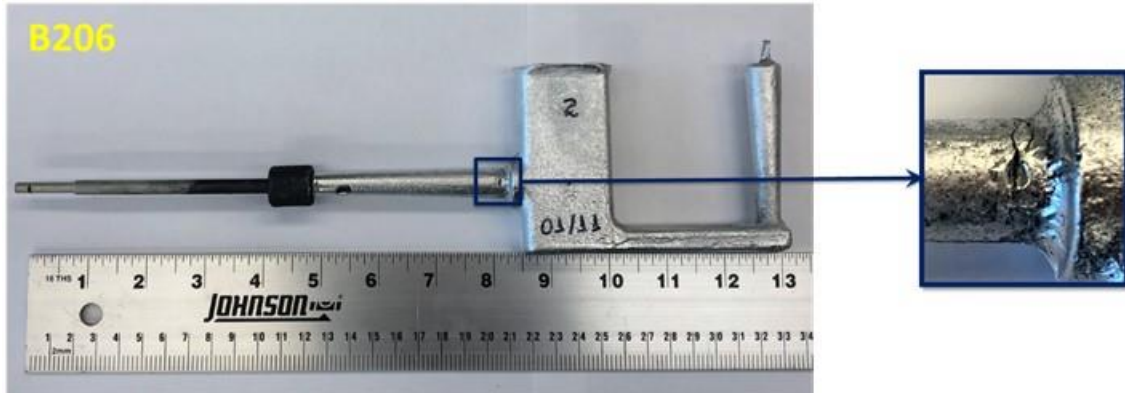
Figure 4.10: Area selected for imaging in CT Scan apparatus.

To ensure that the same area was being analyzed in all samples, it was determined through the slice 256 of each sample (slice that is located in the middle of the sample); a reference slice that would be equivalent in all the samples. Figure 4.11 shows the slice 256 image and how the reference slice was calculated. Once the reference slice was determined, then 249 slices above of it was added in order to obtain the same scanned area results for all samples. The following procedure was carried out for each of the experiment samples. The generated results refer to the area between A-A and B-B.
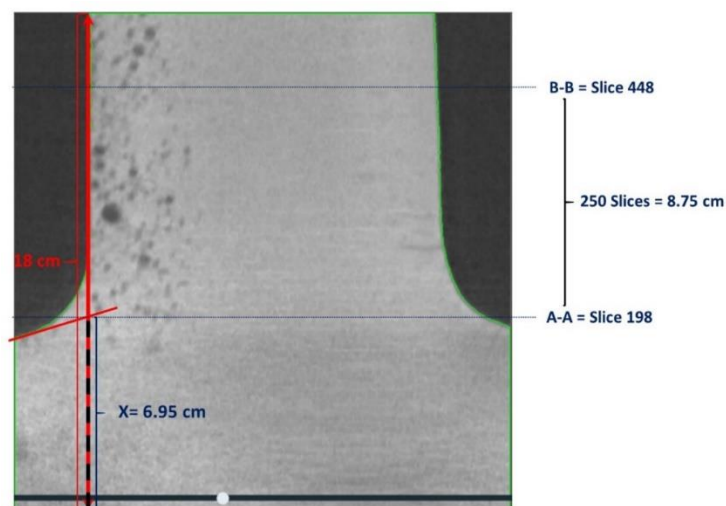
Figure 4.11: Determining the reference slice on the CT image (Slice 256).

The data acquired from the CT Scan was analyzed using the Thermo Scientific Amira[4] Software. Furthermore, the software was used to create the 3D images and calculate the volume and surface area of the whole selected area of the sample and hot crack and pores, separately.

4.3. Microstructure

Microstructure analyses were carried out in the regions of the tophat with hot tearing and in the hot tearing samples from the CRS experiments. The samples were sectioned using a vertical band saw, hot mounted in Bakelite, and ground and polished for metallography. The tophat samples were etched using Keller's reagent for grain size analysis and the hot tearing samples were etched using 0.5% HF reagent for secondary phases analyses. The light optical microscope used for the analyses was the Nikon Eclipse LV100.

Further, the crack surface of the tophat samples was analyzed in the Scanning Electron Microscopy (SEM). The samples were not etched or polished. A carbon tape was added around the sample to promote electrical conductivity. Secondary electron and backscatter images were obtained using the SEM JEOL 6610LV. Several mages of the crack surface were taken to identify the phases and the grain morphology at the crack location. The mapping feature in electron-dispersive X-ray spectroscopy (EDS) was used for phase identification purposes and elements composition.

---

[4] Thermo Fisher Scientific & Zuse Institute Berlin. 1999. Amira Software.

CHAPTER 5. *RESULTS AND DISCUSSIONS*

The results of this thesis would focus on the behaviour of three (3) alloys, namely, the Al-Zn-Mg (Alloy A), Al-Zn-Mg-Fe (Alloy B) and Al-Zn-Mg-Fe-Ti (Alloy C), in the constrained rod solidification experiments for analyzing the hot tearing tendencies of them. The alloy A356.2 would be used occasionally as a benchmark alloy that does not exhibit any tendency to hot tear. Prior to the evaluation of the three alloys of interest, the constrained rod solidification (CRS) apparatus was improved upon to provide repeatable and reproducible responses. The following sections would be elaborated in this chapter.

- Solidification Simulations and Microstructure of Alloys

- Improvements to CRS Experiments

- CRS Experiment Results

- Computerized Tomography (CT) Imaging

- Limiting Conditions for Hot Tearing in CRS Experiments

In order to better understand the presentation of the results and subsequent discussions, a detailed understanding of the CRS experiments would be beneficial. Figure 5.1 presents a schematic of the CRS experiments along with some salient features of the same. The term *constrained rod solidification* refers to the nature of solidification of the *zone of interest* within the casting that would be constrained on both ends, one by the stationary load cell and the other at the end opposite to the load cell in the *zone of interest*. Constraining the zone during solidification enables the collection of transient load from the load cell during solidification. Typically, when the load sensor experiences a *pull*, as shown in Figure 5.1 the force (load) increases while it is negative when the sensor

experiences a *push*. When the load sensor is replaced by an LVDT sensor to measure transient displacement of the solid in the mould, the LVDT sensor is free to move within the mould and would be either dragged on with the solidifying metal, by a *pull* due to solidification shrinkage or experience a *push* from the liquid filling the mould under a pressure head for flow. When the experiments were carried out for the transient temperature measurements, there was no constraint on the sensor side of the mould around the location marked *TC3*.
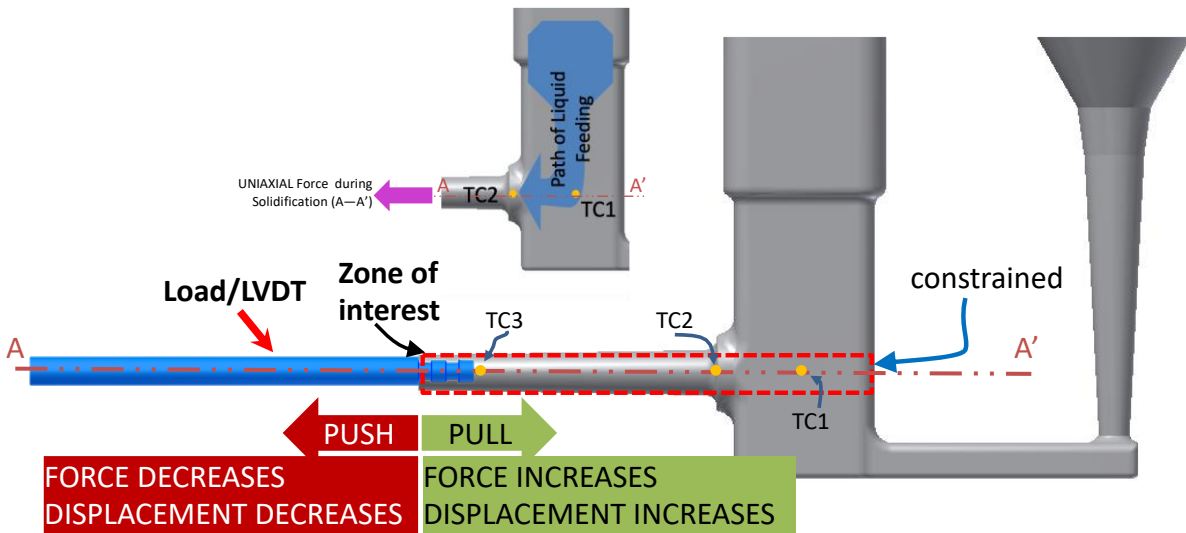
Figure 5.1: A schematic of the constrained rod solidification experiments along with the salient notations and process.

5.1. Solidification Simulation and Microstructure of Alloys

The composition of these alloys was measured, as described in Section 4.1.3 and the results are presented in Table 5.1.

Table 5.1: Chemical composition of the alloys (wt %) used in the experiments.

Alloy	Zn	Mg	Fe	Cu	Si	Mn	Ni	Ti	Al	
A356	-	0.38	0.06	<0.01	6.70	<0.001	-	0.14	Bal.	Achieved
B206	0.02	0.28	0.04	3.71	0.06	0.26	0.0014	0.03	Bal.	Achieved
Alloy A	4.00	1.00	-	-	-	-	-	-	Bal.	Targeted
	3.81	0.93	-	-	-	-	-	-	Bal.	Achieved
Alloy B	4.00	1.00	1.20	-	-	-	-	-	Bal.	Targeted
	3.81	0.93	1.17	-	-	-	-	-	Bal.	Achieved
Alloy C	4.00	1.00	1.20	-	-	-	-	0.10	Bal.	Targeted
	3.81	0.93	1.17	-	-	-	-	0.11	Bal.	Achieved

Solidification simulations were carried out using the Pandat[5] Software with the PanAl-2024 Al alloy database. The Scheil-Gulliver (S-G) solidification paradigm, wherein complete diffusion of the solutes in the solidifying liquid while no diffusion in the solid phase was assumed. The solidification temperatures, transient average solute composition in the remaining liquid phase, and reaction temperature and products for each phase evolved during solidification are presented in Table 5.2 and Table 5.3 presents the predicted volume percentage of each phase in the solidified microstructure. The phases C14 and HCP are both metastable solidifying phases of two different stoichiometry of the (Al, Zn, Mg) phase.

---

[5] Computherm LLC., Madison, WI, USA.

Table 5.2: Prediction of solidification phases from simulations using the Scheil-Gulliver model.

Alloy A						
T (°C)	w%(Al)	w%(Zn)	w%(Mg)			Phases
648.4	95.26	3.81	0.93			Liquid+**α(Al)**
478.7	37.42	49.09	13.48			Liquid+ α(Al)+ **σ(AlZnMg)**
475.3	31.48	57.36	11.16			Liquid+ α(Al)+ σ(AlZnMg)+**C14**
357.8	4.89	91.88	3.22			Liquid+ α(Al)+C14+**Mg$_2$Zn$_{11}$**
345.0	3.70	93.86	2.44			α(Al)+Mg$_2$Zn$_{11}$+**HCP**
Alloy B						
T (°C)	w%(Al)	w%(Zn)	w%(Mg)	w%(Fe)		Phases
643.5	94.09	3.81	0.93	1.17		Liquid+ **α(Al)**
642.1	93.65	4.06	0.99	1.29		Liquid+ α(Al)+ **Al$_{13}$Fe$_4$**
478.6	36.96	49.77	13.27	4.79E-05		Liquid+ α(Al)+ **σ(AlZnMg)**
475.3	31.48	57.36	11.16	6.66E-08		α(Al)+σ(AlZnMg)+**C14**
Alloy C						
T (°C)	w%(Al)	w%(Zn)	w%(Mg)	w%(Fe)	w%(Ti)	Phases
658.1	93.98	3.81	0.93	1.17	0.11	Liquid+**Al$_3$Ti**
646.5	93.99	3.81	0.93	1.17	0.09	Liquid+Al$_3$Ti+**α(Al)**
561.4	62.87	29.20	7.89	0.04	1.49E-15	Fcc+**Al$_{13}$Fe$_4$**
Alloy A356.2						
T (°C)	w%(Al)	w%(Si)	w%(Mg)	w%(Fe)	w%(Ti)	Phases
718.0	92.35	7.00	0.35	0.10	0.20	Liquid+**Al$_3$Ti**
617.3	92.47	7.03	0.35	0.10	0.05	Liquid+Al$_3$Ti+ **α(Al)**
573.9	86.42	12.78	0.60	0.20	1.30E-06	Liquid+α(Al)+**Si**
570.6	85.39	12.95	1.21	0.45	2.57E-10	Liquid+α(Al)+Si+ **β(AlFeSi)**
559.6	82.16	13.56	3.98	0.30	1.77E-15	α(Al)+Si+ β(AlFeSi)+**Al$_8$FeMg$_3$Si$_6$**

Table 5.3: Volume percentage of solidified phases in the three alloys after solidification with Scheil-Gulliver paradigm.

Alloy A		Alloy B		Alloy C		Alloy A356.2	
Phases	Mass %	Phases	Mass %	Phases	Mass %	Phases	Mass %
α(Al)	99.08	α(Al)	96.80	Al$_3$Ti	4.27E-02	Al$_3$Ti	0.35
σ(AlZnMg)	0.91	Al$_{13}$Fe$_4$	2.32	α(Al)	97.64	α(Al)	93.52
C14	0.012	σ(AlZnMg)	0.87	Al$_{13}$Fe$_4$	2.32	Si	5.13
Mg$_2$Zn$_{11}$	1.30E-04	C14	9.98E-03			β(AlFeSi)	-0.10
Hcp	7.08E-05					Al$_8$FeMg$_3$Si$_6$	1.10

Figure 5.2 presents the graph of transient solid fraction evolved as a function of temperature during the solidification of the three alloys. It could be observed in that the primary Al phase, α(Al) evolves over a temperature range of 169.7 °C (Table 5.2) before the evolution of other minor trace phases. Nearly 99% of all the α(Al) solidify without any other phase evolving, during this large temperature range.
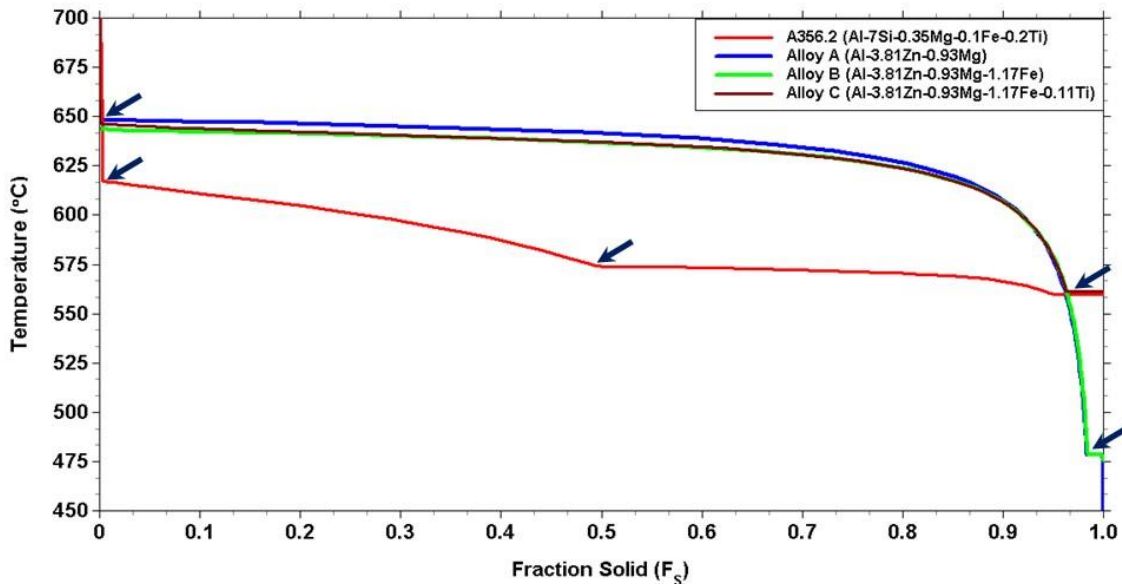

Figure 5.2: Transient solid fraction as a function of temperature for the three alloys.

In Alloy B, the co-evolution of about 2.32% of $Al_{13}Fe_4$ phase along with the α-Al for about 165 °C, results in a two-phase evolution during the solidification. In Alloy C, the addition of trace levels of Ti (0.1wt%), significantly alters the solidification pattern, wherein, the solidifying temperature range is reduced to about 85 °C and the evolves separately followed by the $Al_{13}Fe_4$ phase evolves as a eutectic phase along with α-Al at 561.4 °C. The addition of about 1.2 wt% Fe to the Alloy A results in a dual-phase solidification scenario while the further addition of 0.1wt % of Ti to this alloy significantly alters the solidification to one akin to a eutectic alloy (polyphase) solidification. Typically, from our understanding of the background literature in hot tearing of the Al alloys, it would be safe to assume that the hot tearing tendencies of Alloy A would be higher than that of Alloy B, and Alloy B would be higher than that of Alloy C.

Figure 5.3 (a) to (c) shows the typical light optical microstructures of Alloy A, Alloy B and Alloy C, respectively; in Alloy A, the light-coloured phase matrix is the α(Al) phase, while the dark shaded precipitates are the minor σ(AlZnMg) phase; while, in Alloy B, the α(Al) evolves as columnar and dendritic structure along with the $Al_{13}Fe_4$ phase, demarcated as intermetallic phases (IMP), evolving in the inter-dendritic regions of α(Al); in Alloy C, the α(Al) phase evolves as equiaxed dendrites with the $Al_{13}Fe_4$ phase (IMP) evolving as eutectic phase along with Al in the interdendritic/inter-granular regions of the microstructure. The specimen for all the microstructure images in Figure 5.3 was obtained from the location demarcated as *TC2* in Figure 5.1 along with typical hot cracks in Alloy A and shrinkage voids in Alloy B. The optical microstructure readily shows the significant differences in the solidified microstructure of the three alloys, stemming from the differences in their respective solidification characteristics, as described earlier in this sub-

section. The addition of Fe to Alloy A enables the formation of two phases in tandem during solidification while the further addition of Ti in Alloy C changes the morphology of the primary Al phase to an equiaxed dendrite, which is more favourable for alleviating hot tearing.

(a)
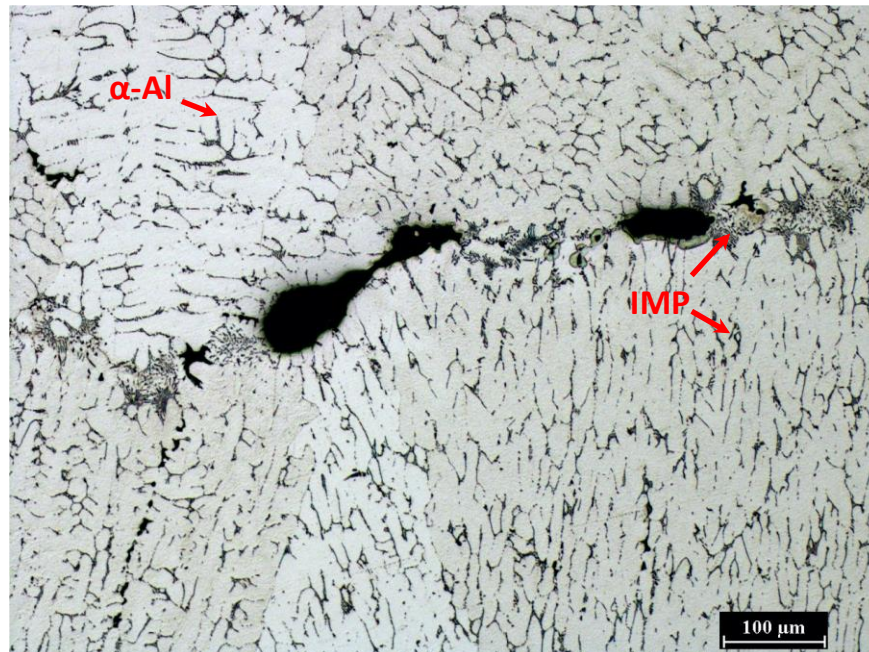
(b)
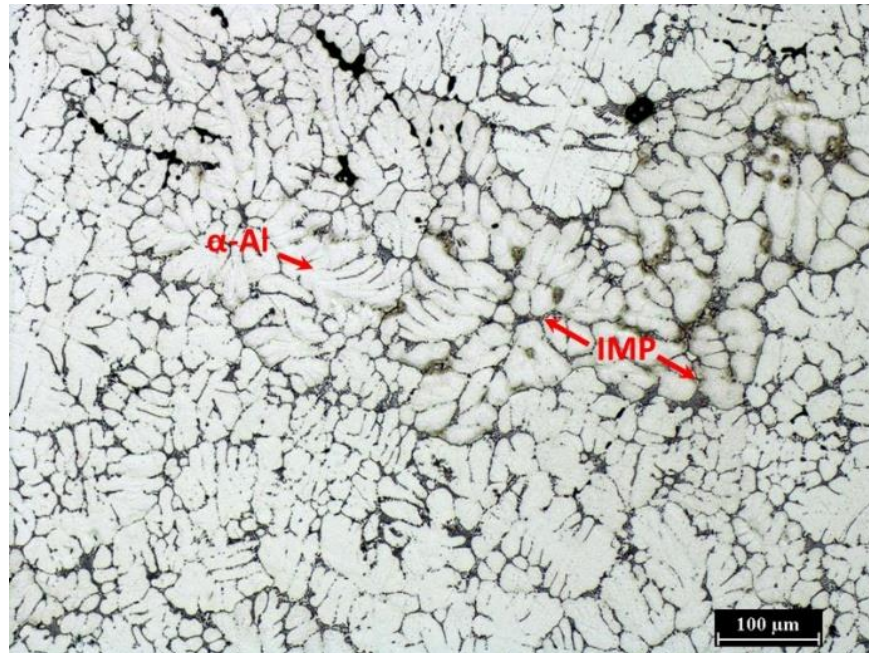
(c)

Figure 5.3: Typical light optical microstructure of the three alloys. (a) Alloy A, (b)

Alloy B and (c) Alloy C.

5.2.   Improvements to the CRS Experiments

Two aspects of the CRS experiments to measure the hot tearing sensitivity was improved in this work to,

- maintain a repeatable and consistent heat extraction across all experiments.

- maintain a uniform and consistent filling of the mould

Pouring temperature is a key factor when understanding hot tearing, as it defines the initial thermal state of the melt at the beginning of solidification in the mould. The previous generation of the CRS experiments was carried out at the melt pouring temperature of 750 ºC while using a graphite coating sprayed onto the die mould surface. Figure 5.4

presents the transient temperature curves from thermocouples in locations *TC1*, *TC2* and *TC3*, as shown in Figure 5.1; wherein the graph shows that the maximum temperature in thermocouple at *TC1* is barely above the liquidus temperature ($T_{liquidus}$) and the thermocouple at *TC 2* is below the $T_{liquidus}$, suggesting that the state of the alloy at the end of the filling stage is already in the two-phase mushy (semi-solid) state in the *zone of interest* (ZOI), shown in Figure 5.1. Hence, in order to minimize the mushy zone in the ZOI, the pouring temperature was increased to 900 °C and the resultant cooling curve is presented in Figure 5.5.
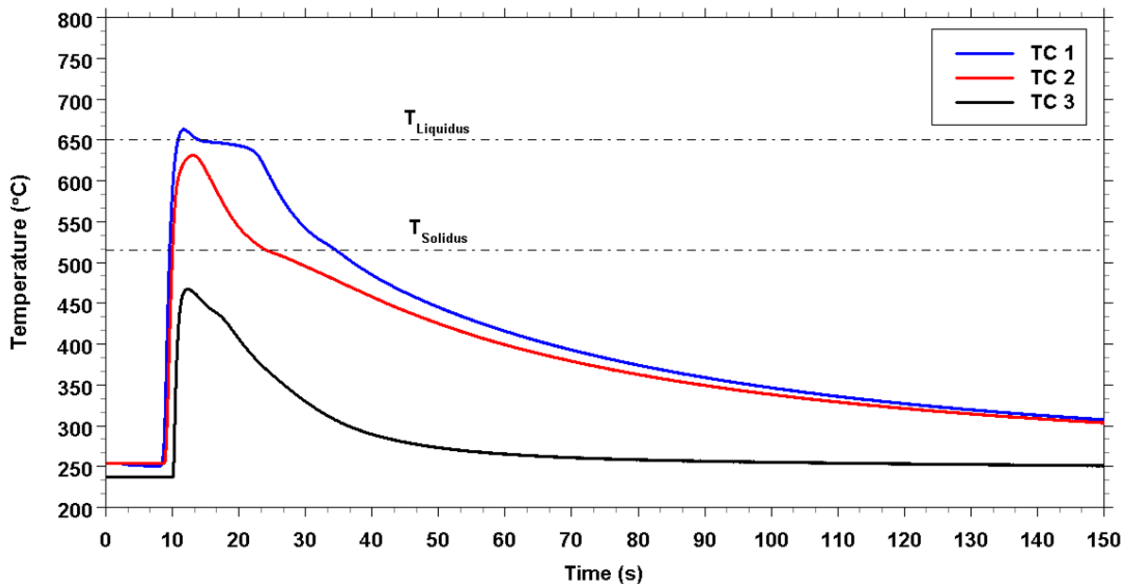
Figure 5.4: Typical transient thermal curves from *TC1*, *TC2* and *TC3* in Figure 5.1, during solidification in the CRS mould. The mould surfaces were coated with graphite and maintained at 250ºC, while the melt pouring temperature was 750 ºC.
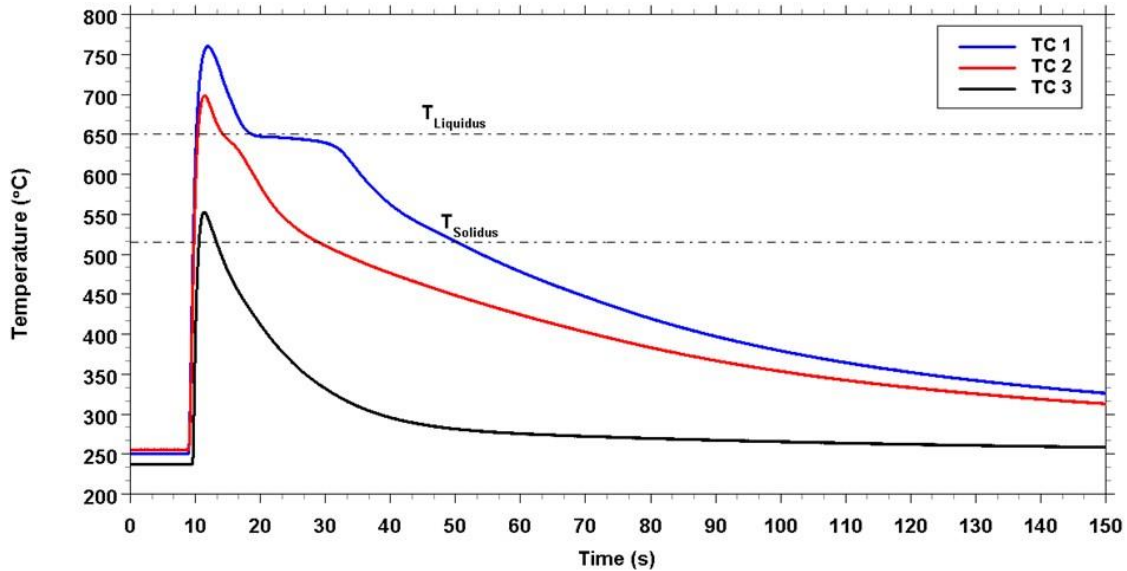
Figure 5.5: Typical transient thermal curves from *TC1*, *TC2* and *TC3* in Figure 5.1 during solidification in the CRS mould. The mould surfaces were coated with graphite and maintained at 250⁰C, while the melt pouring temperature was 900 ⁰C.

Increasing the pouring temperature to 900 ⁰C, as in Figure 5.5, increases the peak temperature at the end of mould filling, however, the temperature in location *TC2* did not increase enough to well above the $T_{Liquidus}$ as it can be observed in Figure 5.6; further, Figure 5.6 shows that the peak temperature at the location *TC2*, could not repeatably reach above the $T_{Liquidis}$ while varying the mould preheat between 250 and 400 ⁰C.
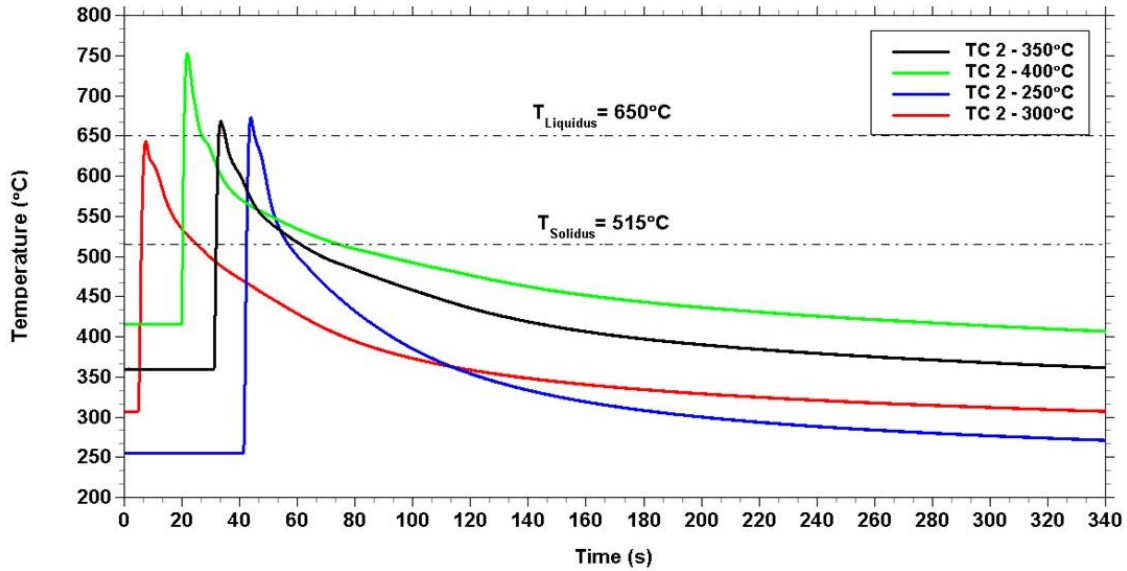
Figure 5.6: Transient temperature profiles of location *TC2* for a melt pouring temperature of 900ºC, with a graphite coated mould surface at four different mould preheat temperatures.

Aiming to increase the temperature in the thermocouple TC2 to at least 50 ºC above the $T_{Liquidus}$, required a decrease in the cooling rate of solidification, a layer of sprayed-on refractory Boron Nitride (BN) coating was administered on the mould surface beneath the sprayed graphite coating. The results obtained are presented in Figure 5.7; wherein, the peak temperature at TC2 was well over the $T_{Liquidus}$ and was repeatably so.
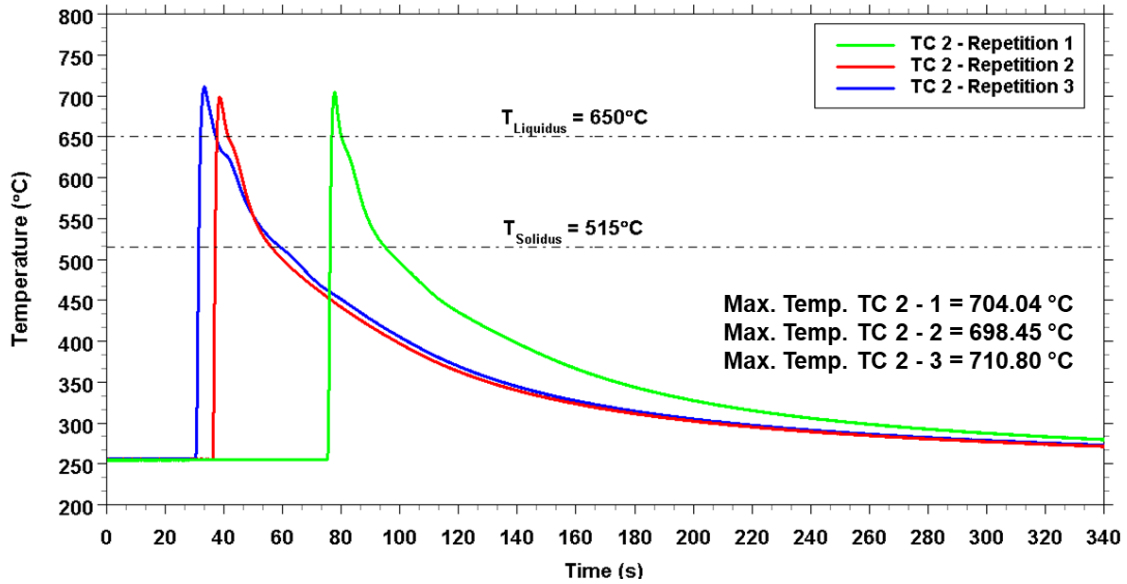
Figure 5.7: Transient temperature profiles of location _TC2_ for a melt pouring temperature of 900ºC, with two mould surface coatings of Boron Nitride and graphite, respectively. The mould preheat temperature was 250 ºC.

In order to maintain a mould filling pattern that is repeatable and reproducible, a pouring cup with a funnel was added to the pouring section of the mould. The funnel used in the experiment was made in the lab and it is shown in Figure 5.8. The melt is poured and accumulated in the funnel that was initially plugged with a graphite stopper rod; subsequently, the graphite stopper was removed to obtain a more uniform and repeatable fill of the mould in all experiments in this work.
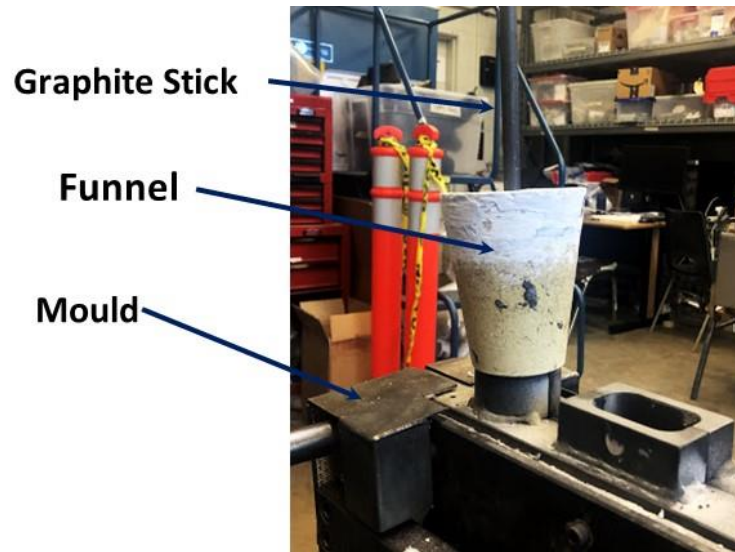
Figure 5.8: Funnel with a graphite stick used in all experiments.

In summary, the changes made to the melt pouring stage of the experiment in introducing a pouring cup with a funnel spout in the bottom created a more uniform mould filling scenario when coupled with an initial melt pouring temperature of 900 ºC. Further, the introduction of the boron nitride (BN) layer on the mould surface coupled with a graphite coat on top of the BN coat, enabled a more balanced cooling of the alloy during solidification and enabled a reasonable superheat of the melt above the alloy liquidus temperature at the end of the filling the mould.

5.3.   CRS Experiment Results

Figure 5.9 (a), (b) and (c) present the data acquired for one set of three experiments carried out for Alloy A with a mould preheat temperature of 200 ºC, transient thermal data, transient displacement from LVDT sensor and transient load from the load sensor, respectively; the red circles, demarcated as X, Y and Z, show the position in the graph that were used to align and normalize the curves to time.
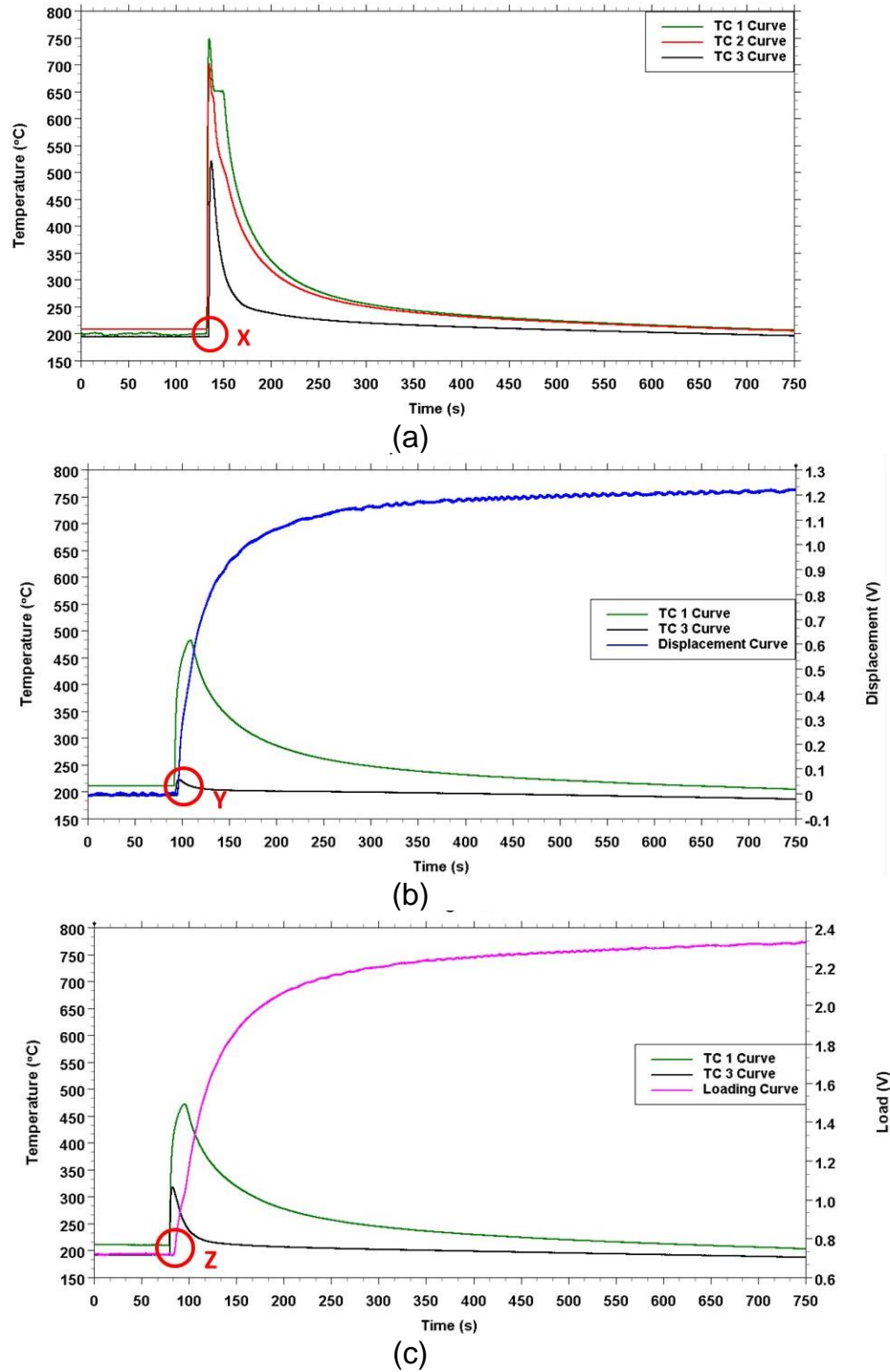
Figure 5.9: Transient Data (as obtained) acquired during one set of experiments with an alloy in the CRS mould; (a) transient thermal, (b) transient displacement and (c) transient loading.

After the data was collected, locations X, Y and Z were matched up and plotted to obtain a graph as shown in Figure 5.10. The temperature curves of the displacement and loading experiment were eliminated since the thermocouples were in the wall of the mould and the temperatures were measured only to merge the curves and confirm the mould preheat temperature.
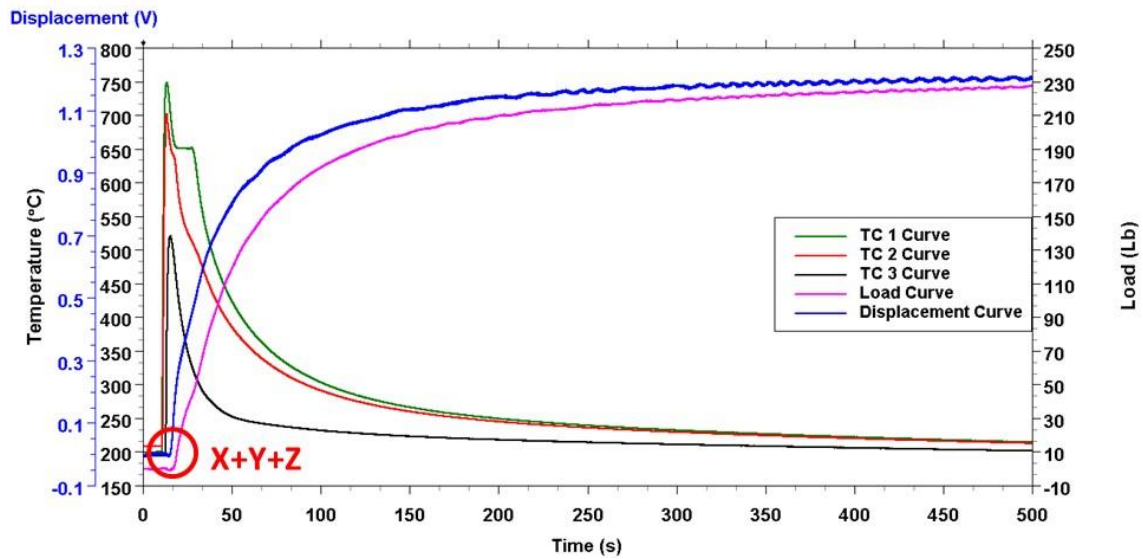
Figure 5.10: Processed data for transient thermal, displacement and load to merge the three and normalize with respect to time.

Once the curves were matched and normalized with time, the data was processed to obtain the value of stress and strain. The strain was obtained from the displacement curves voltage date, using the calibration curve shown in Figure 4.7 of Section 4.1.2. APPENDIX A presents all the normalized thermal, load and displacement curves for the three alloys at four mould preheat temperatures each.

The localized uniaxial stress along the A-A' axis shown Figure 5.1 was evaluated from the measured load (refer to Equation) was divided by the cross-sectional area of the mould at the location *TC2*. Further, to facilitate visualization of the data from one set of

experiments for an alloy, a combined graph was plotted; wherein the following information could be visually observed and evaluated:

- Transient temperature at location *TC1* (ordinate) as a function of strain (abscissa),

- Transient temperature at location *TC2* (ordinate) as a function of strain (abscissa),

- Transient temperature at location *TC2* (ordinate) as a function of normalized time (abscissa),

- Stress (ordinate) as a function of Strain (abscissa),

- Gradient of stress with respect to strain $\left(\frac{d\sigma}{d\varepsilon}\right)$ (ordinate) as a function of strain (abscissa), and

- Simulated Fraction solid evolved (S-G paradigm) (abscissa) as a function of Temperature (ordinate).

The final processed curve found for the Alloy A with a mould preheat of 200 ⁰C is shown in Figure 5.11.
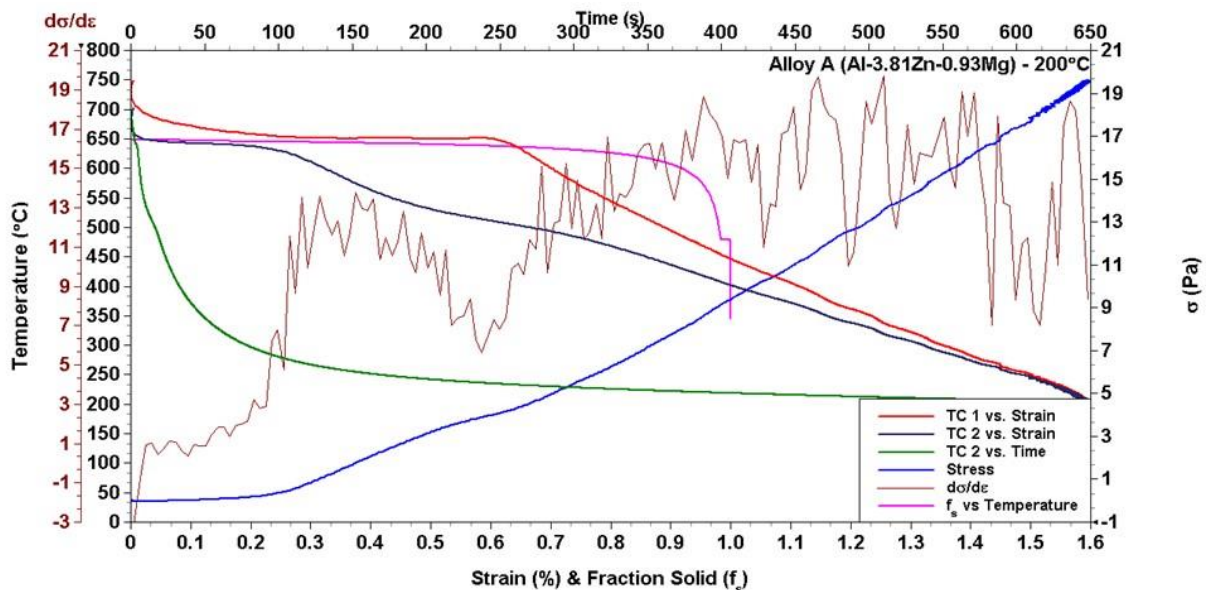
Figure 5.11: Final Curves of Alloy A at mould preheat temperature 200⁰C.

A graph for each alloy (Alloy A, Alloy B and Alloy C) at four different mould preheat temperatures were obtained and presented in Figure 5.11 to Figure 5.22. A graph for the alloy used as a reference, Alloy A356.2 at mould preheat temperature of 250ºC is also presented in Figure 5.23.

Figure 5.12: Final Curves of Alloy A at mould preheat temperature 250ºC.

Figure 5.13: Final Curves of Alloy A at mould preheat temperature 300ºC.

Figure 5.14: Final Curves of Alloy A at mould preheat temperature 350ºC.
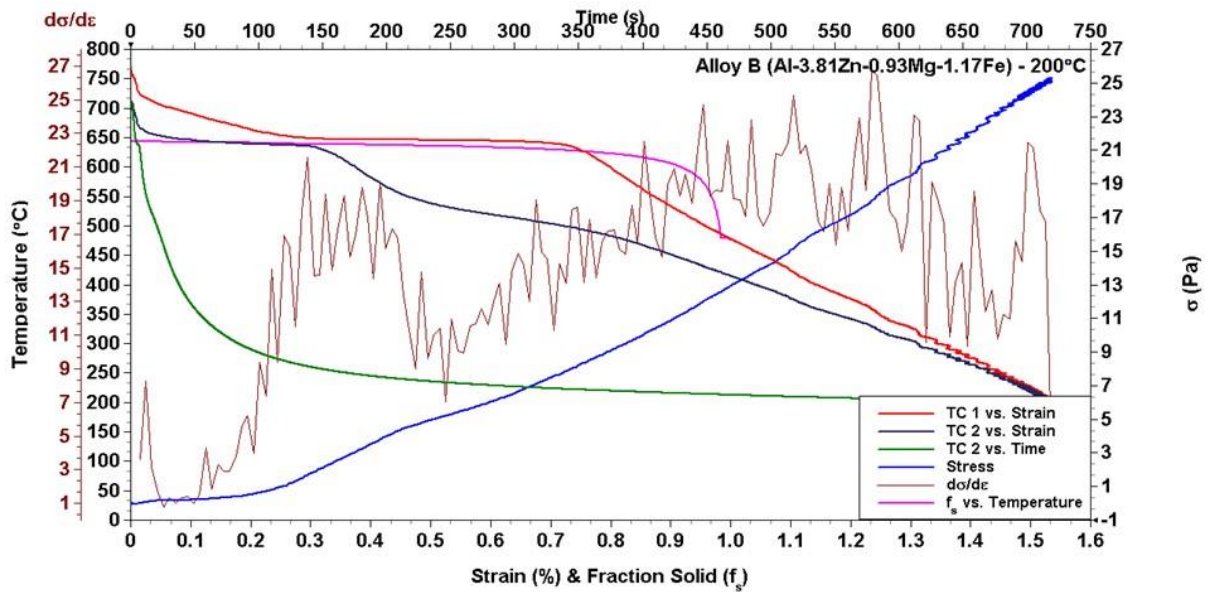
Figure 5.15: Final Curves of Alloy B at mould preheat temperature 200ºC.
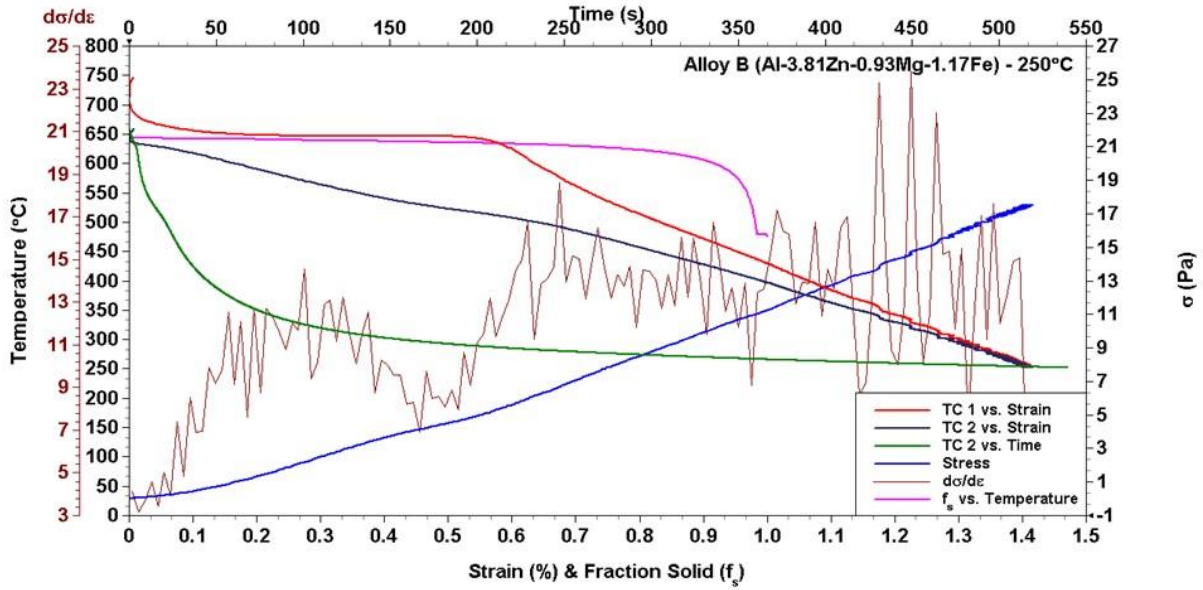
Figure 5.16: Final Curves of Alloy B at mould preheat temperature 250⁰C.
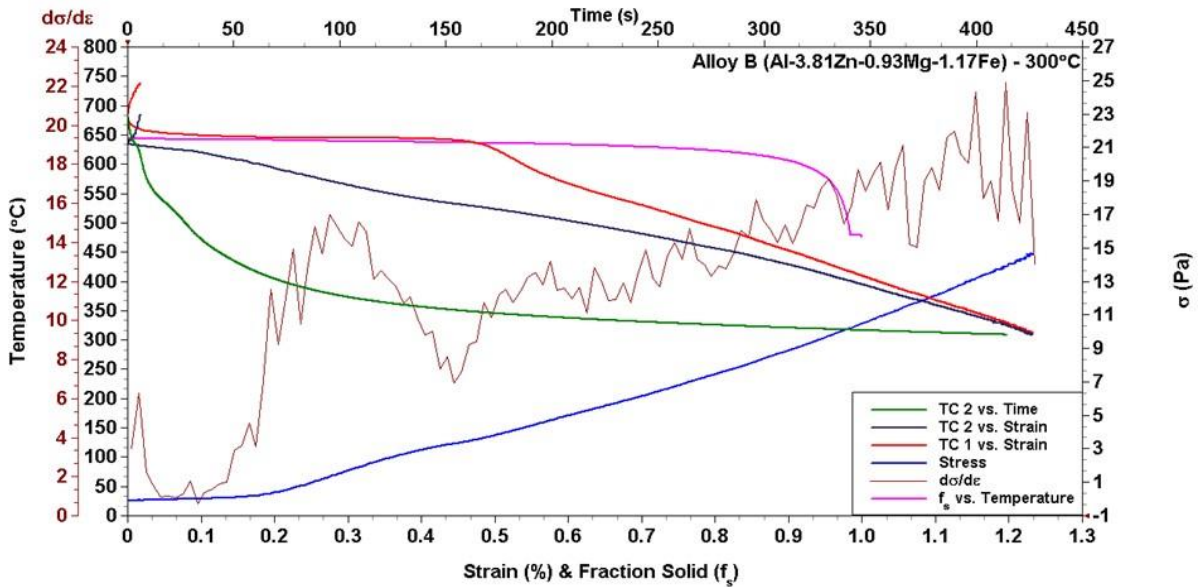
Figure 5.17: Final Curves of Alloy B at mould preheat temperature 300⁰C.
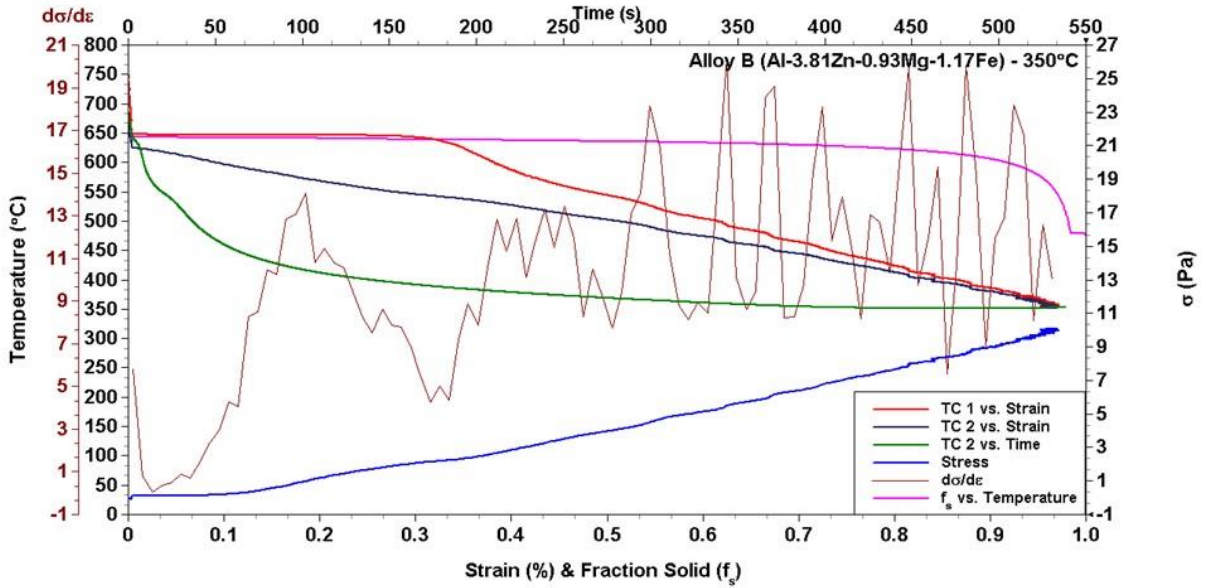
Figure 5.18: Final Curves of Alloy B at mould preheat temperature 350⁰C.
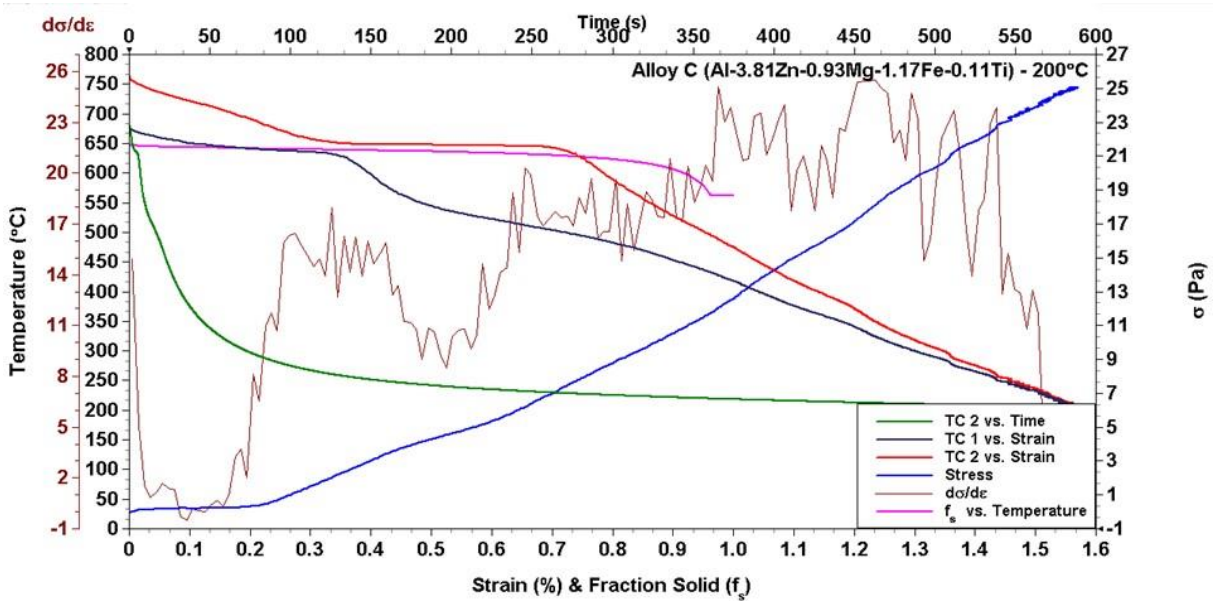
Figure 5.19: Final Curves of Alloy C at mould preheat temperature 200⁰C.
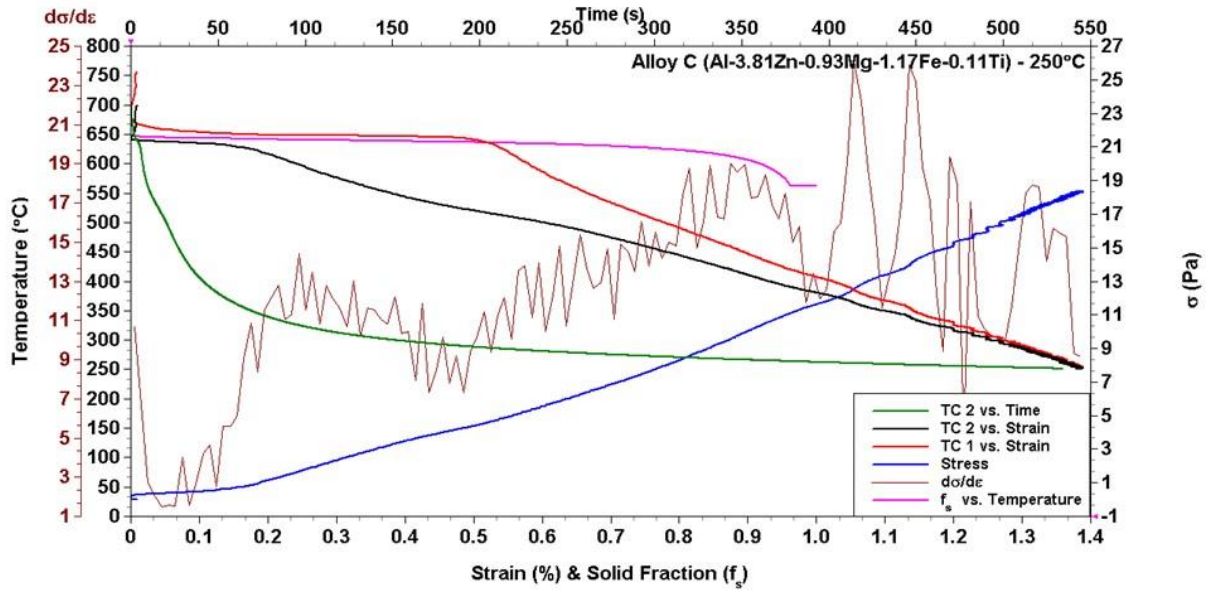
Figure 5.20: Final Curves of Alloy C at mould preheat temperature 250ºC.
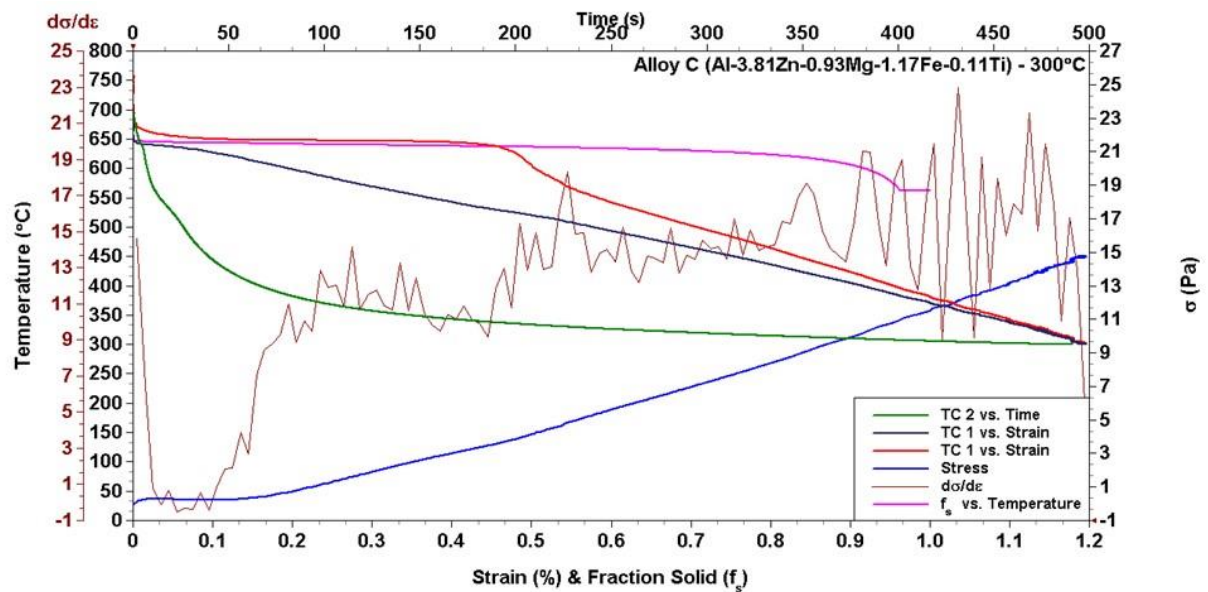
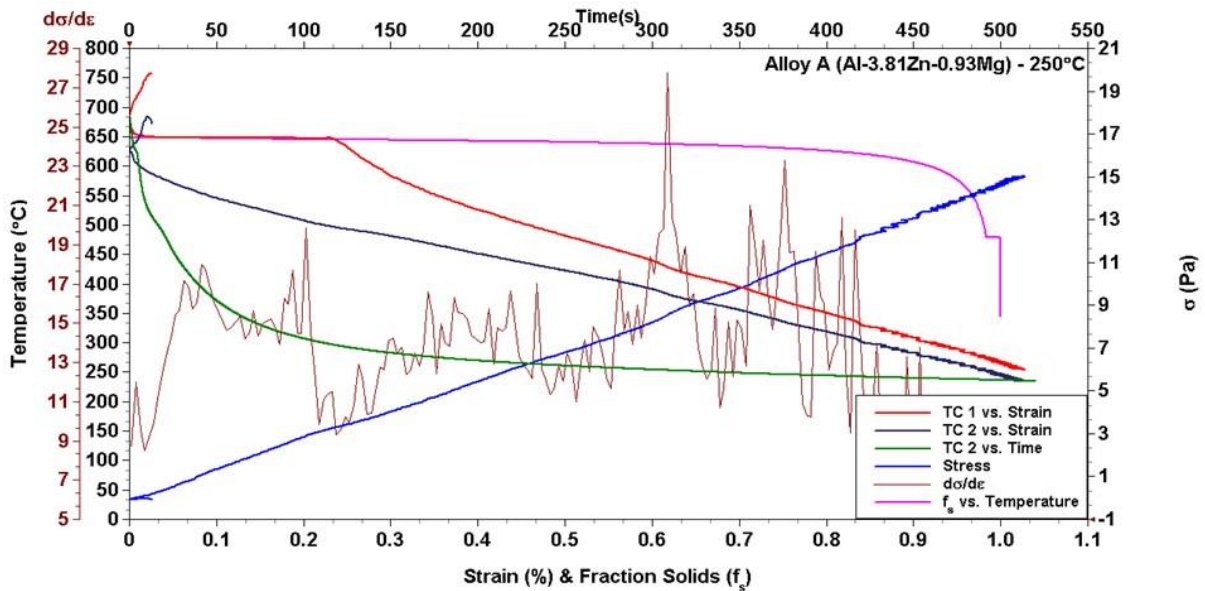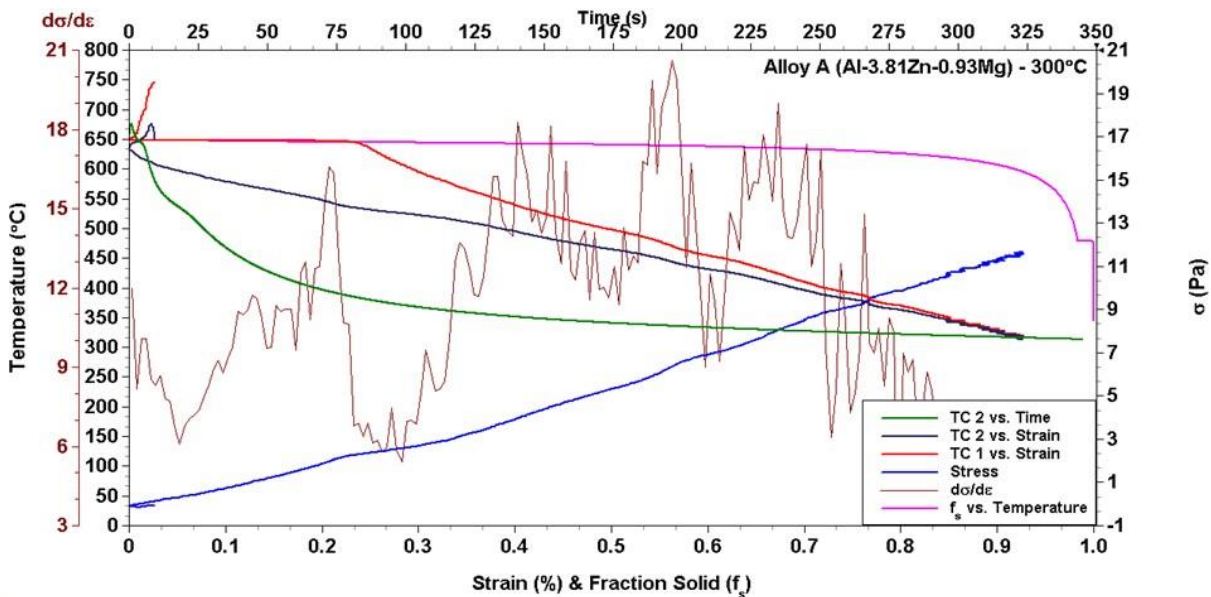**Figure 5.21: Final Curves of Alloy C at mould preheat temperature 300ºC.**
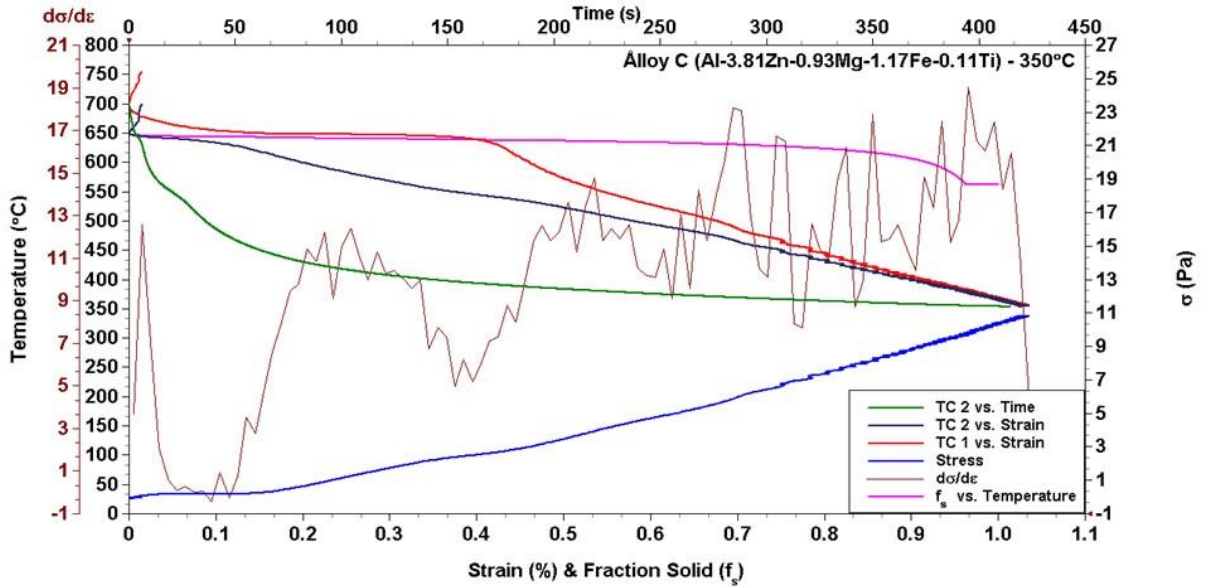
Figure 5.22: Final Curves of Alloy C at mould preheat temperature 350⁰C.

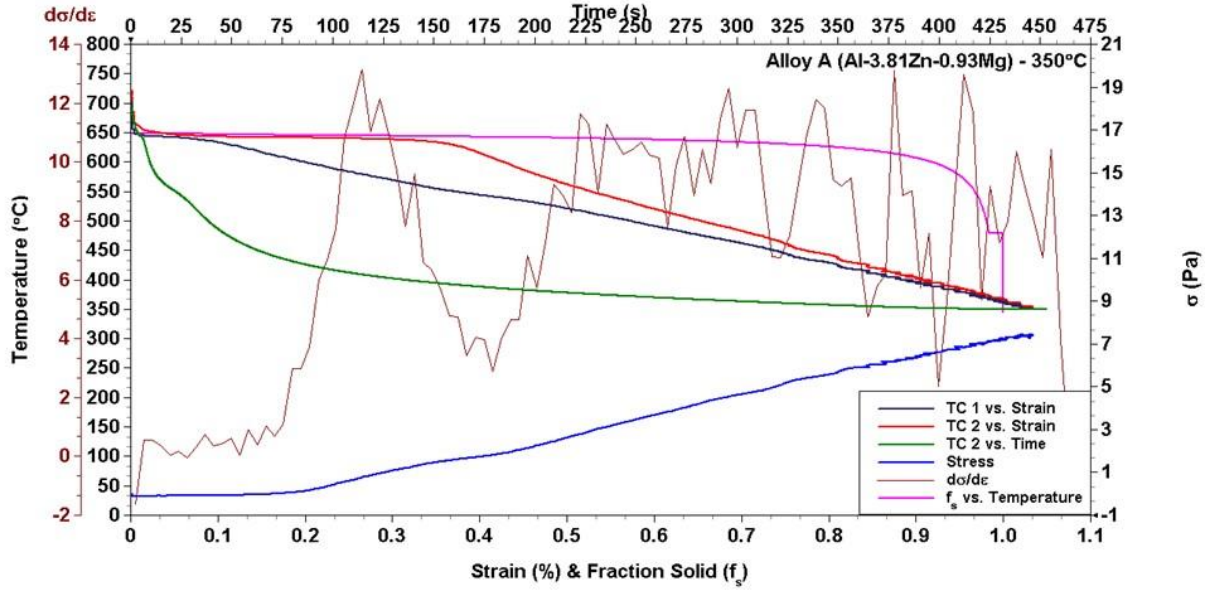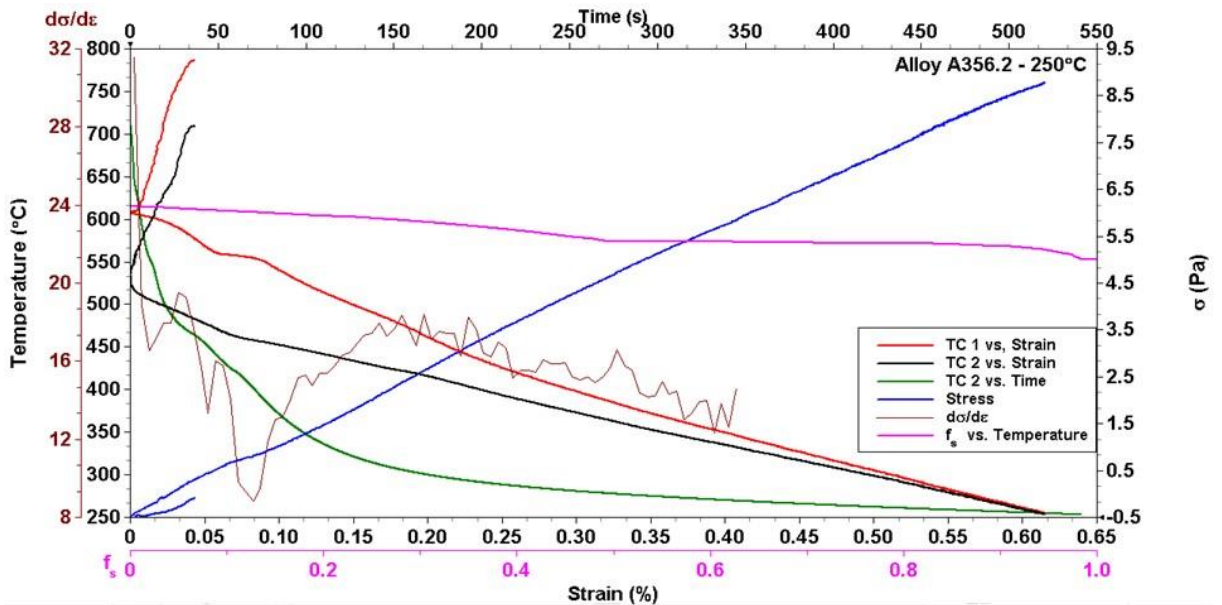**Figure 5.23: Final Curves of Alloy A356.2 at mould preheat temperature 250⁰C.**

After all the curves were plotted, critical data information was evaluated for the locations *TC1, TC2* and *TC3* within the ZOI in Figure 5.1. The salient observations from the curves

in Figure 5.11 to Figure 5.22, for the three alloys, were at the following critical solidification events within the ZOI.

- System coherency point → identified as subscript *coh*

- System coalesce point → identified as subscript *coas*

- End of solidification → identified as *end*.

The data for solid fraction (f_s), time (t), stress (σ) and strain (ε), at each of the above-mentioned critical event points such as *coh*, *coas* and *end* were identified, as shown in Figure 5.24 and tabulated in Table 5.4.
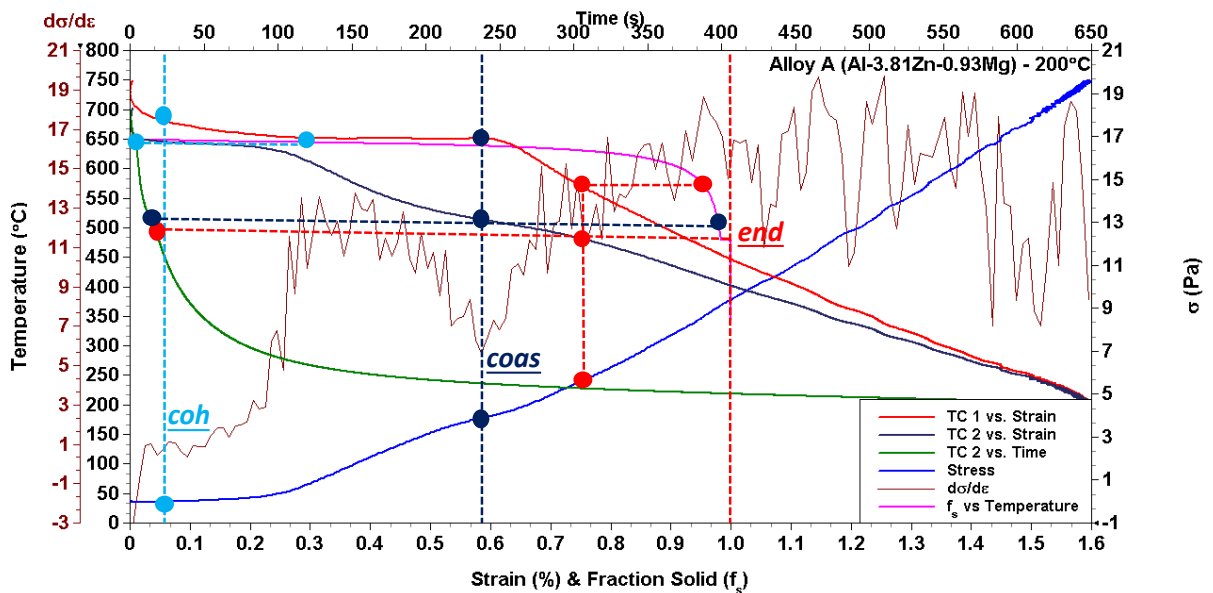
Figure 5.24: Typical locations of critical events during solidification in the CRS experiments; system coherency (*coh*), system coalesce (*coas*) and end of solidification of ZOI (*end*) collected in the Alloy A for a mould preheat of 200⁰C. *coh* (Light Blue); *coas* (Dark Blue) and *end* (Red).

Table 5.4: Data collected for critical events from the graphs in Figure 5.11 to Figure 5.22, following the process shown in Figure 5.24.

| Alloy	Mould T	Stress	Strain	TC 1	fs - TC1	TC 2	fs - TC2	Time
Coherency Point								
A	200	-0.01	0.0530	679.8	0	645.5	0.297	3.11
	250	-0.05	0.0021	662.9	0	623.4	0.827	4.45
	300	0.00	0.0000	650.2	0	637.1	0.643	5.62
	350	-0.10	0.0150	653.4	0	644.6	0.340	4.64
B	200	0.22	0.0600	699.7	0	650.0	0.000	3.90
	250	0.07	0.0020	696.5	0	637.4	0.470	2.59
	300	-0.08	0.0000	681.2	0	636.0	0.540	3.30
	350	0.00	0.0000	673.5	0	638.4	0.410	3.73
C	200	0.22	0.1600	706.0	0	644.4	0.070	2.51
	250	0.30	0.0000	695.7	0	645.5	0.030	2.49
	300	0.00	0.0000	693.0	0	649.3	0.001	3.06
	350	-0.07	0.0000	695.4	0	649.3	0.001	3.15
Coalesce Point								
A	200	3.95	0.5920	651.1	0	512.5	0.978	14.31
	250	3.25	0.2325	647.1	0.12	496.9	0.981	17.25
	300	2.42	0.2540	631.3	0.75	530.5	0.979	19.63
	350	1.73	0.4300	617.1	0.87	544.5	0.970	24.45
B	200	5.15	0.5200	646.3	0	533.3	0.979	14.71
	250	3.08	0.4200	646.1	0	523.0	0.977	15.52
	300	3.35	0.4500	641.2	0.22	531.6	0.975	18.54
	350	2.24	0.3300	633.1	0.64	540.4	0.972	23.69
C	200	4.53	0.5230	647.2	0.01	538.5	1.000	10.82
	250	3.88	0.4370	645.5	0.04	533.5	1.000	14.24
	300	3.20	0.4155	642.9	0.16	538.3	1.000	17.05
	350	2.37	0.3710	642.7	0.17	549.7	1.000	20.23
End of Solidification								
Alloy	Mould T	Stress	Strain	TC1	fs-T1	TC2	fs-T2	Time
A	200	5.05	0.7100	594.3	0.93	491.1	0.982	17.98
	250	4.76	0.3530	550.3	0.97	465.3	0.990	23.30
	300	3.59	0.3770	55.5	0.97	502.2	0.980	26.50
	350	2.73	0.5530	558.3	0.96	518.4	0.980	32.75
B	200	8.04	0.7360	636.4	0.53	497.3	0.982	20.91
	250	4.60	0.5500	567.6	0.96	488.7	0.983	23.09
	300	4.95	0.5950	568.6	0.96	504.2	0.981	26.12
	350	3.69	0.4660	555.3	0.97	509.7	0.980	33.69
C	200	7.74	0.7400	634.0	1.00	496.3	0.615	17.30
	250	5.94	0.6300	572.0	1.00	493.9	0.956	21.37
	300	4.91	0.5500	563.8	1.00	506.5	1.000	25.08
	350	3.92	0.5330	557.3	1.00	513.7	1.000	31.73

5.3.1. Analyses of the Results from CRS Experiments

Within the ZOI in Figure 5.1 the truncated cylindrical rod section between locations *TC2* and *TC3* is critical to understand the hot tearing tendencies of the solidifying alloy. The location *TC2* is prone to hot tearing due to the drastic change in cross-section area across both sides of this location due to the mould design, leading to a significant gradient in stress and strain fields during solidification across this location. As the solidification proceeds from *TC3* to *TC2*, the alloy shrinks towards *TC2* while being continuously compensated by the liquid feeding from the riser through location *TC1*, as shown in the enlarged section of Figure 5.1.

The system coherency point (*coh*) is defined as the time the liquid feeding the shrinkage in location *TC2* is choked; leading to a notable increase in stress values and $\frac{d\sigma}{d\varepsilon}$, respectively, in this location, as shown by Figure 5.24. The system coalesce point (*coas*) is defined as the time when the final remaining liquid in the location *TC2* solidifies into the secondary and eutectic phases leading to the initiation of a stress relaxation stage indicated by a decrease in both stress and $\frac{d\sigma}{d\varepsilon}$ values in Figure 5.24. The end of solidification (*end*) is the time when the ZOI in Figure 5.1 is solidified and the stress and $\frac{d\sigma}{d\varepsilon}$ values begin to increase with strain, as in Figure 5.24.

At the beginning of the solidification process, the stress is around zero, since the solidification shrinkage is being compensated by the remaining liquid from the *TC2* that is still liquid. Typically, when the location *TC2* reaches the coalesce point (*coas*), the location *TC1* would begin to solidify. Once the *TC1* and *TC2* locations are fully solidified

(*end*), the stress increases with strain in a consistent and predictable manner as defined by the linear thermal contraction of the solid alloy.

Figure 5.25 shows the stress values at the location at the end of the solidification for each alloy as a function of the mould preheat temperature; also shown are the respective linear regression models for the empirical fit of the stress data with mould preheat temperature. The fitting curves show that there is an increase in stress when decreasing mould preheat temperature (increase in rate of heat extraction during solidification). Lower mould preheat temperatures exhibit a higher cooling rate during solidification. At the end of the solidification, the fraction solid at each mould preheat temperature is very similar, however, with the higher cooling rate, more heat is being extracted from the system, resulting in a higher number of grains being formed, and consequently a higher surface area, a higher force pulling the load sensor rod and hence, higher stress.

Further, Alloy A shows a notably lower stress values at the end of the solidification, for each and every mould preheat temperatures due to the hot tears and cracks formed on these samples, which lead to a decrease in load values. Alloy C has a higher stress value because adding Ti to the system leads to refinement of the size and morphology of the solidifying primary α(Al) grains, as shown in Figure 5.3 (c), and consequently, a higher number of equiaxed grains is formed, increasing the surface area of grain boundaries applying an increased load (stress) during solidification.
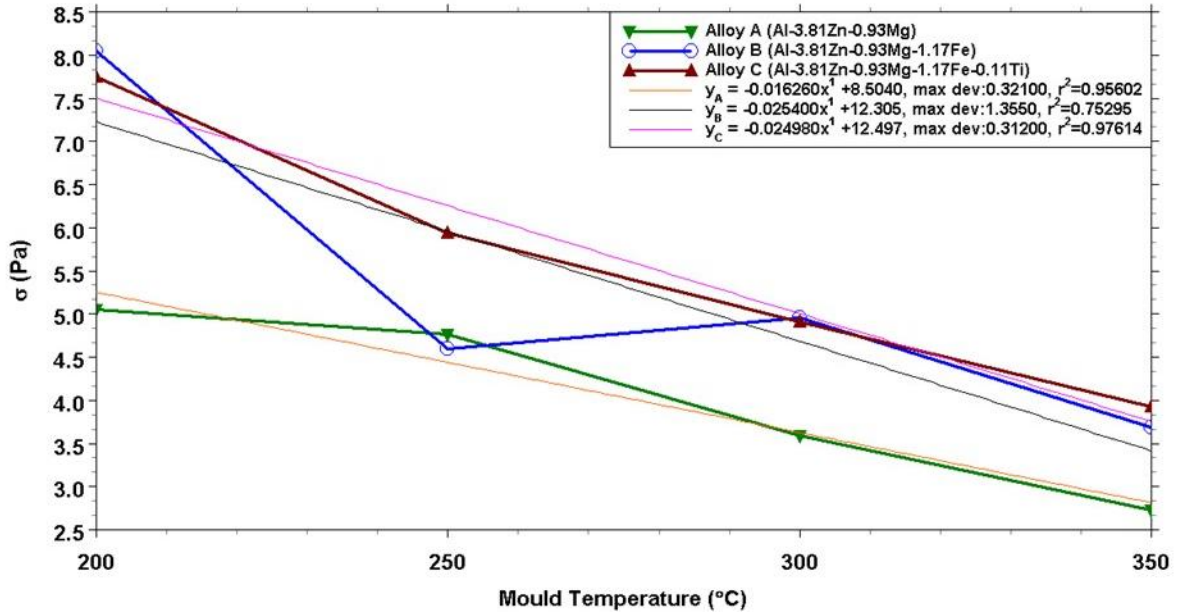
Figure 5.25: Stress Curves for each alloy at the end of the solidification according to the mould preheat temperatures.

Higher stress means higher forces pulling the solidifying grains, increasing the propensity to create stable shrinkage voids leading to a tear when there is no liquid feeding them to heal; this would result in hot tearing at location *TC2*. Hence, the tendency to hot tear in an alloy could be related to the competing phenomena of increasing solidifying stresses in location (*TC2*) and the ability of liquid feeding this location during the *coas* stage during solidification. When comparing the microstructure of the alloys in Figure 5.3 (a), it is evident that at the *coas* stage of Alloy A would exhibit large primary grains of α(Al) with a very thin and flimsy liquid layer in the inter-granular regions, due to the lack of secondary solidifying phases, leading to an increased difficulty in feeding liquid to the final stages of solidification and resulting in an increased tendency to hot tear.

However, in Alloy B, shown in Figure 5.3 (b), the presence of about 3% of the $Al_{13}Fe_4$ phases along with the primary $\alpha(Al)$, results in an increase of liquid surrounding the $\alpha(Al)$ grains, resulting in an improved feedability at the *coas* point. Further, with the primary $\alpha(Al)$ grains of Alloy A, the secondary dendrite arm spacing (SDAS) within the primary grain are significantly larger than that in Alloy B, and the feedability of the regions between the secondary dendrite arms of Alloy A is significantly less than that in Alloy B; due to the presence of more liquid in the interdendritic regions that transforms to the IMP phase of $Al_{13}Fe_4$ in the Alloy B.

In Figure 5.3 (c) for Alloy C, the equiaxed morphology of the primary Al phase coupled with the significantly better distributed IMP phases evolving as the eutectic phases during solidification, in the inter-granular regions, show that this alloys will be the best fed by the liquid at the *coas* stage and would heal and shrinkage void or crack formed from the higher stress gradients acting on the grains during solidification, leading to low tendencies for hot tearing. The increase in the stress state at *coas* from Alloy A to Alloy B to Alloy C is overcompensated by the significant increase in the feedability of the solidifying liquid at this stage for Alloy A, Alloy B and Alloy C, respectively. The increase in feedability seems to be far more dominant than the increase in local solidifying stresses, resulting in a decrease of hot tearing susceptibility (HTS) from Alloy A to Alloy B to Alloy C.

Figure 5.26 presents the t_{coh}, t_{coas} and t_{end} for the three alloys; all the times for the Alloy C is smaller than the two counterparts. Alloy C has a significantly smaller freezing range, as shown in Figure 5.2, and further, the nature of solidification in Alloy C is different from that of Alloy A and Alloy B, in that the addition of Ti as a grain refiner in Alloy C results in an unconstrained nucleation and growth pattern of the $\alpha(Al)$ phase [23], while that in Alloy

A and Alloy B are constrained growth for the α(Al) phase [23]. These two features further enhance the liquid feeding in Alloy C during the *coas* stage and alleviate the HTS; similar results were reported by Li et al. [31], as well for the grain refined primary Al alloys.
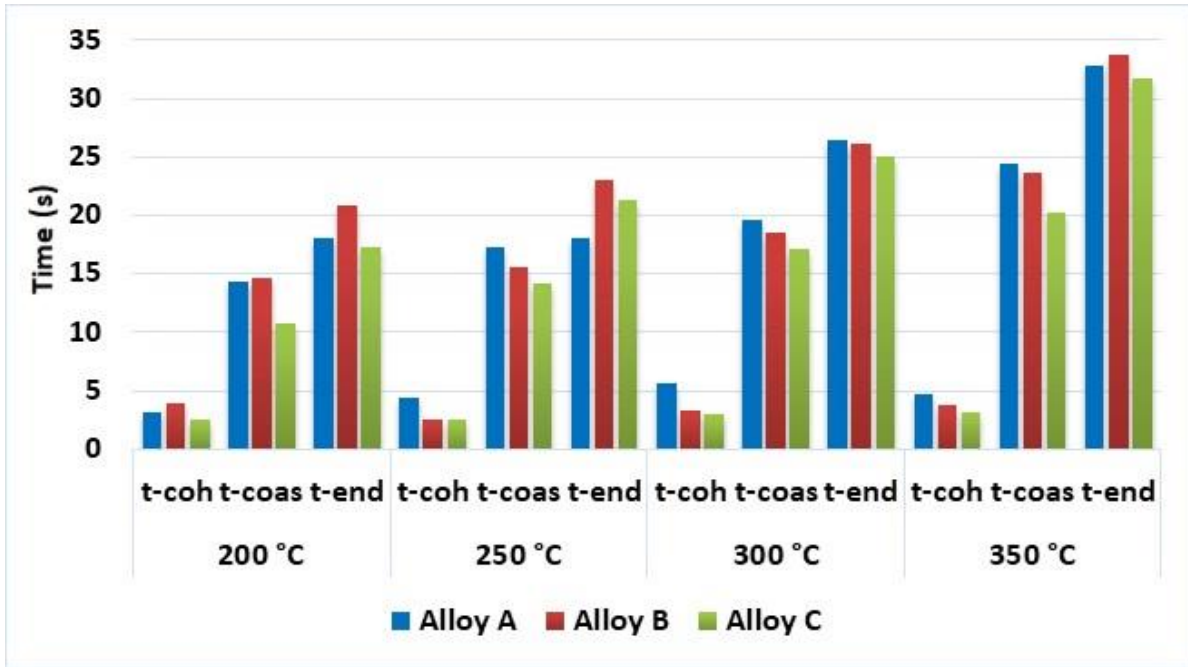
Figure 5.26: t-coh, t-coas and t-end for the three alloys at four mould preheat temperatures, each.

The calibration of the load and LVDT sensors during the experiments enabled the evaluation of the uniaxial σ–ε graphs at the location *TC2* for all three alloys; as shown in Figure 5.27(a), (b) and (c) for Alloy A, Alloy B and Alloy C, respectively, for four (4) mould preheat temperatures, each. Notably, detailed calibration of the LVDT sensor data to obtain the change in dimensions of the solidifying metal enabled the generation of the uniaxial σ–ε graphs during the solidification of these alloys.
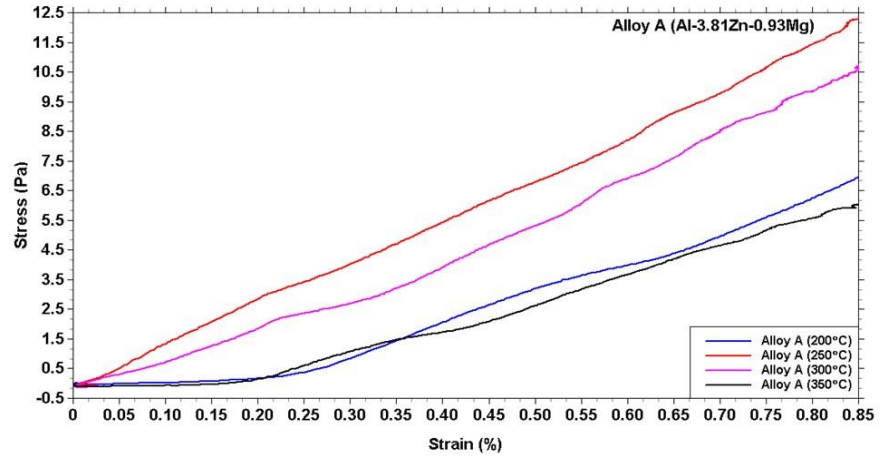
(a)
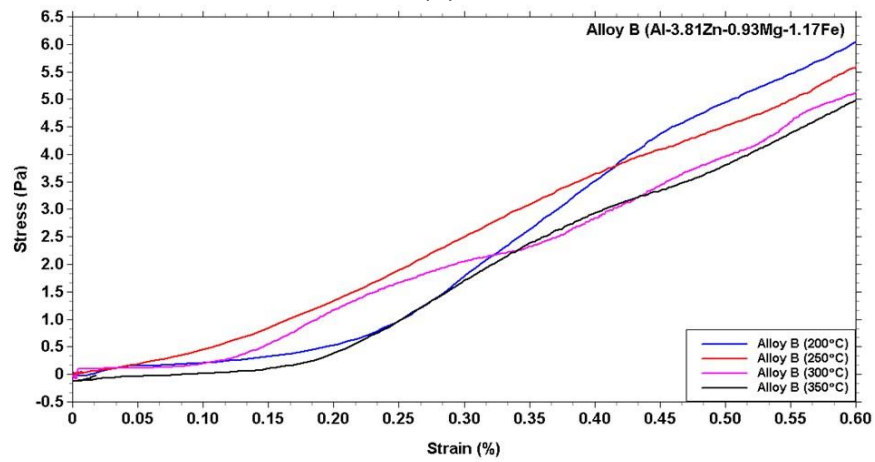
(b)
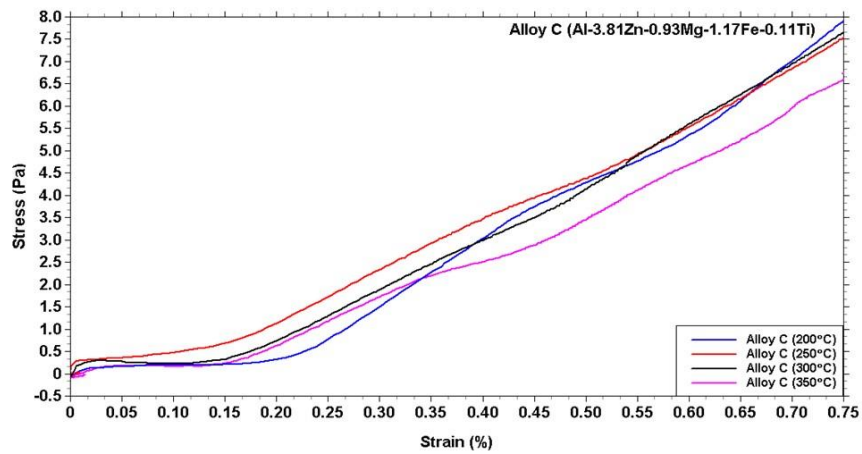
(c)

Figure 5.27: Uniaxial Strain-Stress Curves during solidification for (a) Alloy A, (b) Alloy B and (c) Alloy C at four (4) different mould preheat temperatures, each.

5.4. Computerized Tomography (CT) Imaging

CT Imaging was used in this work to assist with the identification and analyses of hot tearing in the alloy samples. The CT Scan showed to be an effective tool to help to measure and analyze hot tearing. Further, it was possible to construct high-quality 3D images of the hot tear. Figure 5.28 shows a CT Scan image and 3D images of the B206 (Al-Cu based) alloy samples with hot tearing.
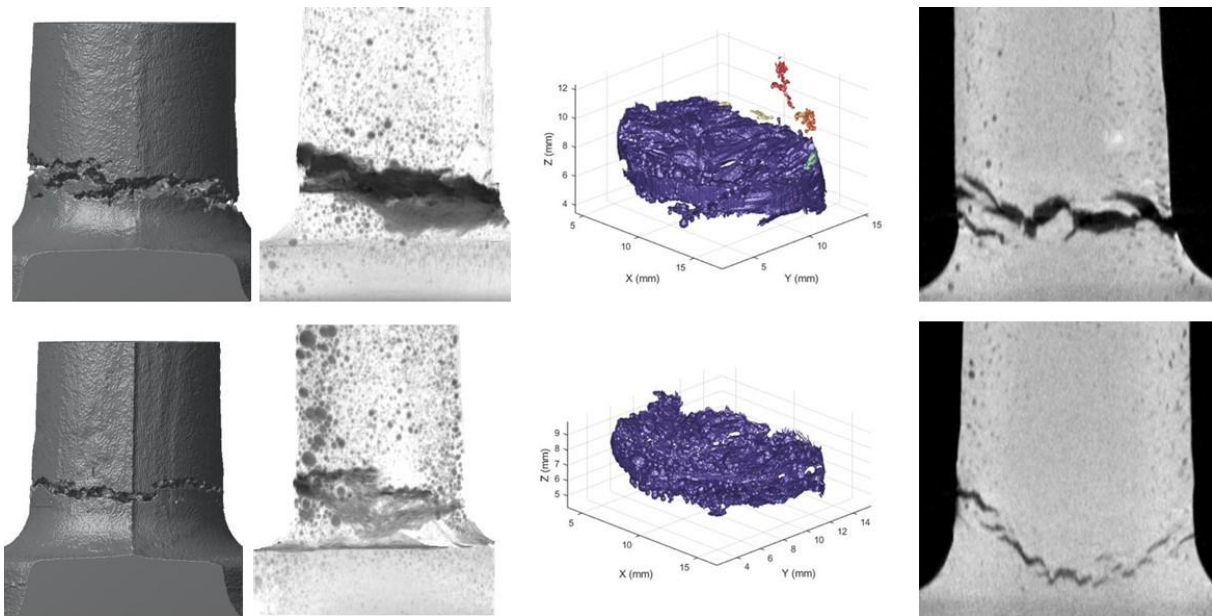
Figure 5.28: CT Scan images and analyses from the Alloy B206. The gravity vector acts on the plane of view, pointing in the right direction.

The CT Scan was used to obtain images of the hot tearing samples. After the hot tearing experiments were carried out each of the samples was CT Scanned. The resulting images were analyzed in the Thermo Scientific software Amira[6], in which the 3D images of the

---

[6] Thermo Fisher Scientific & Zuse Institute Berlin. 1999. Amira Software.

samples were generated and several features such as the surface area and volume of the sample, cracks and pores, were evaluated. The images obtained along with a picture of the casting at location *TC2* for the three alloys, Alloy A, Alloy B and Alloy C in this study are presented in Figure 5.29. The calculated volume and the surface area of the sample, pores and cracks are presented in Table 5.5.
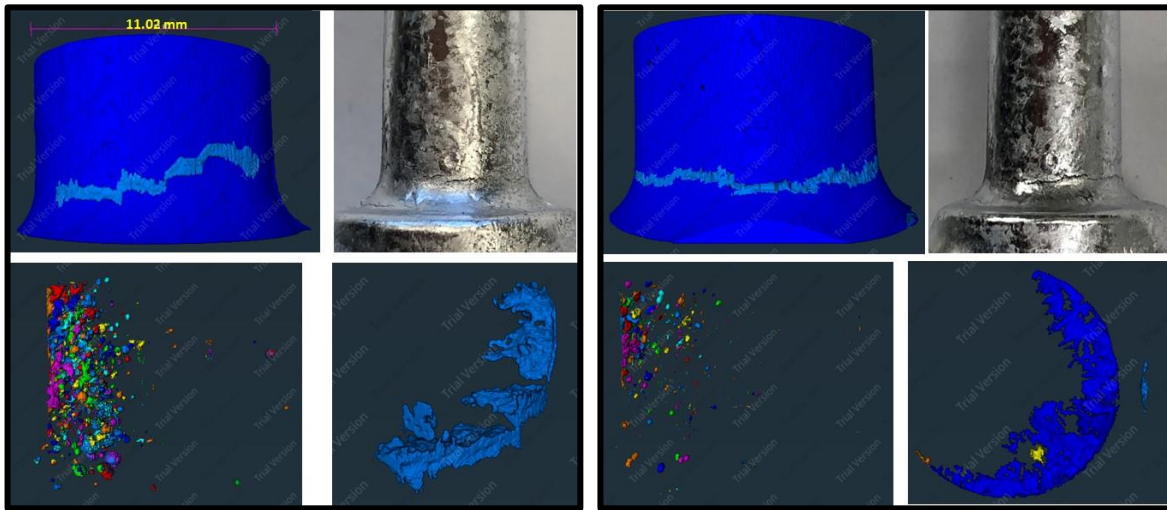
(a)

(b)
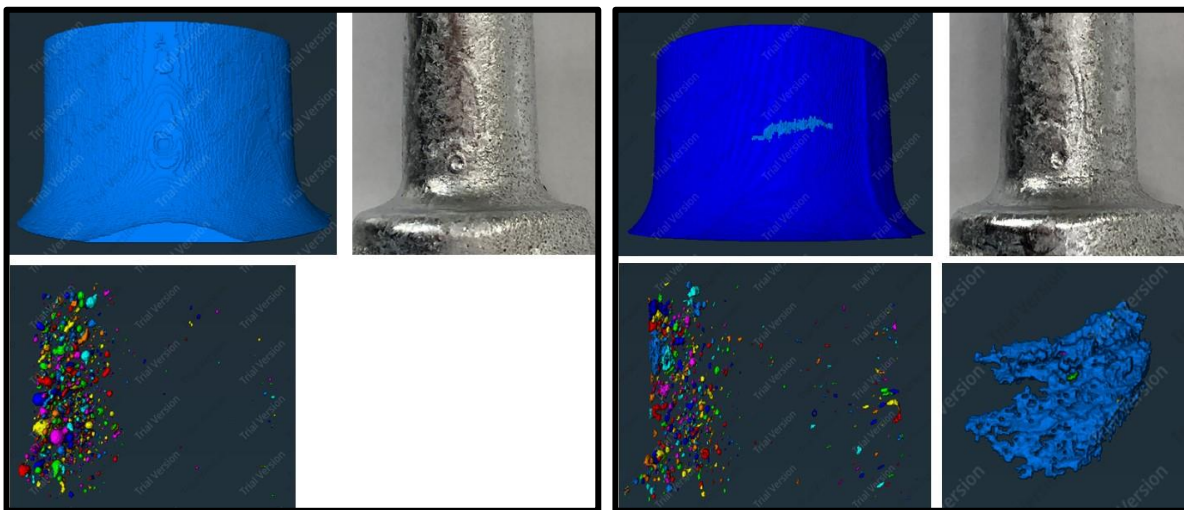
(c)

(d)
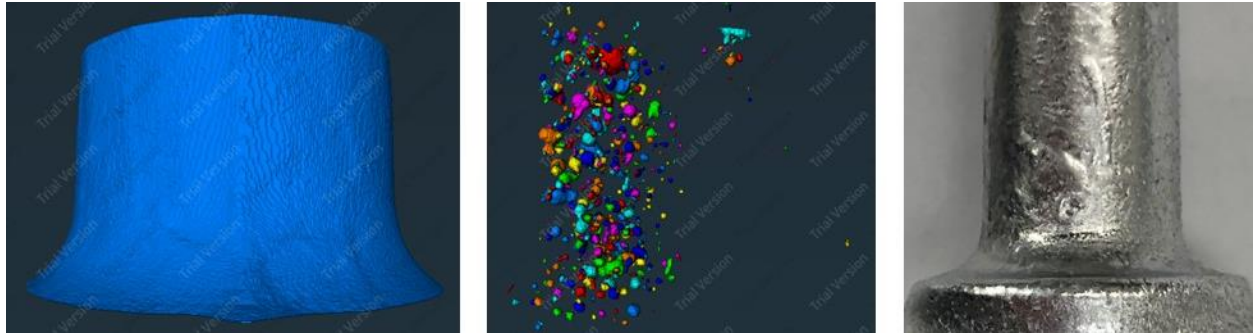
(e)

(f)
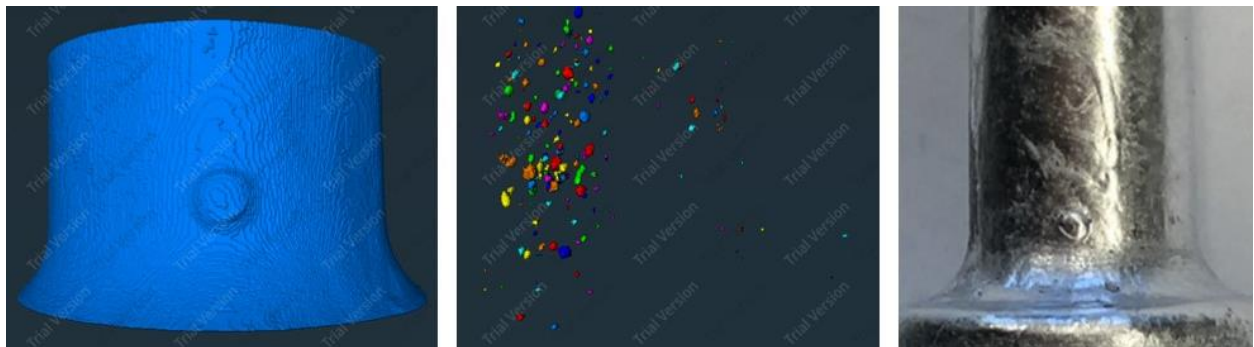
(g)
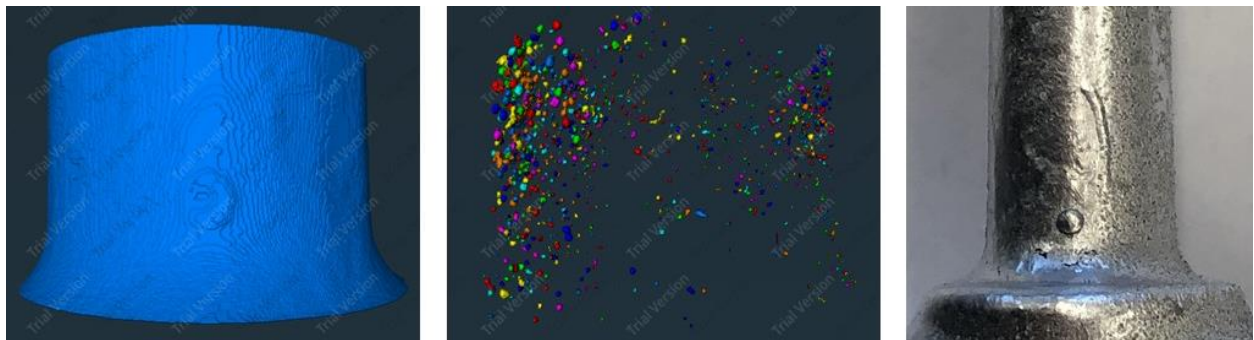
(h)
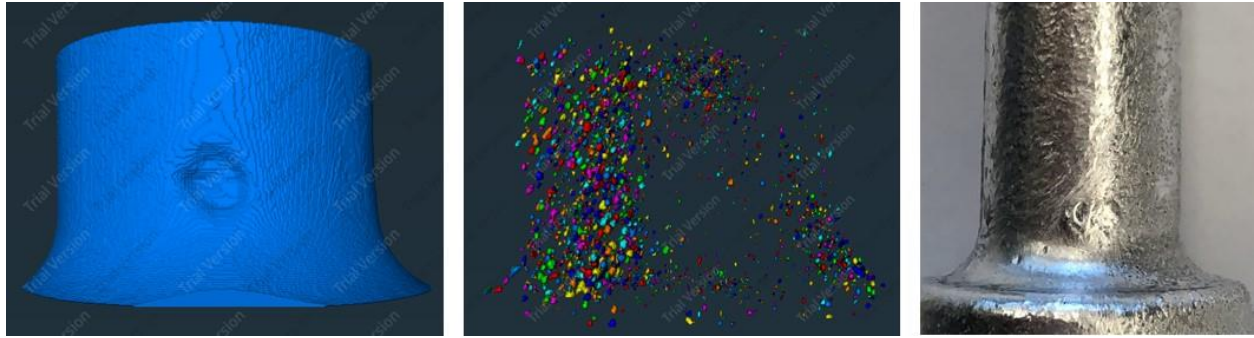
(i)
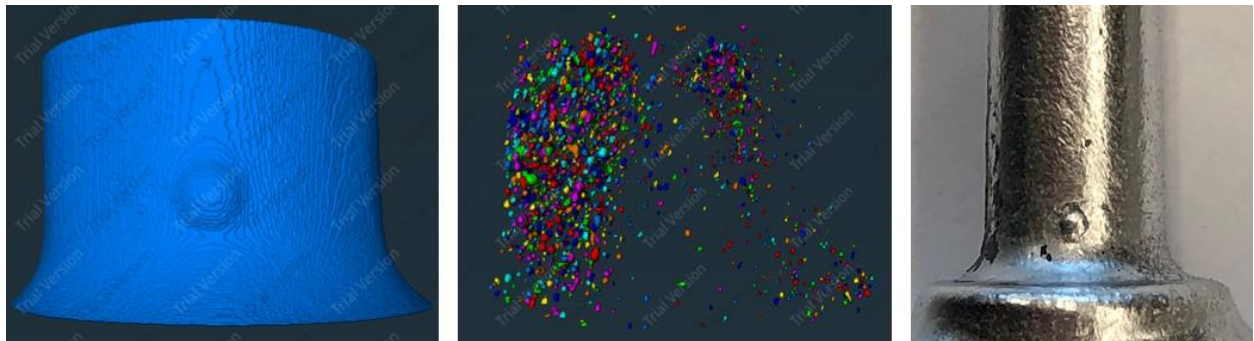
(j)
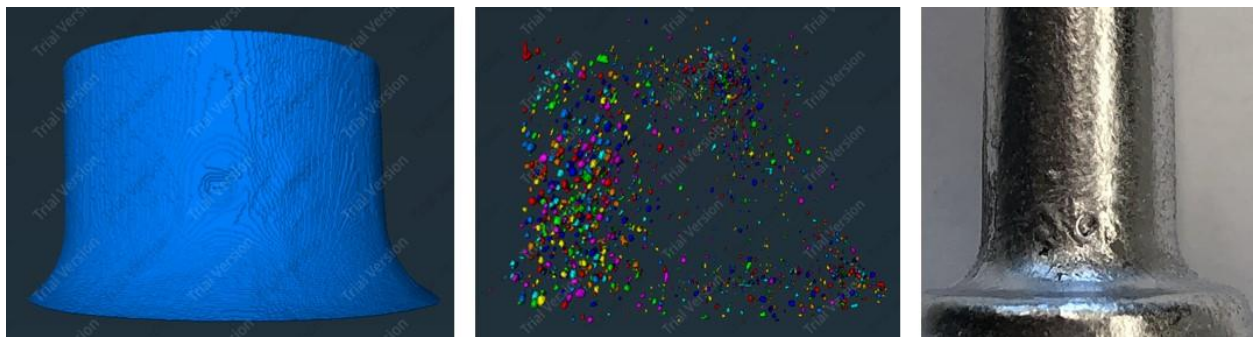
(k)
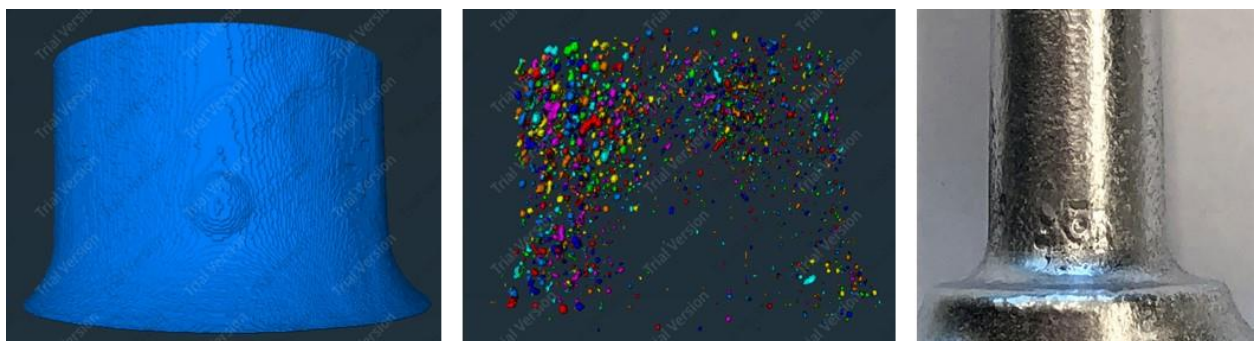
(l)

Figure 5.29: Computerized Tomography (CT) images with CT analyses and casting photograph: (a) Alloy A – Mould preheat temperature at 200⁰C; (b) Alloy A – Mould preheat temperature at 250⁰C; (c) Alloy A – Mould preheat at temperature 300⁰C; (d) Alloy A – Mould preheat at temperature 350⁰C; (e) Alloy A – Mould preheat at temperature 250⁰C; (f) Alloy B – Mould preheat at temperature 250⁰C; (g) Alloy B – Mould preheat at temperature 300⁰C; (h) Alloy B – Mould preheat at temperature 350⁰C; (i) Alloy C – Mould preheat at temperature 200⁰C; (j) Alloy C – Mould preheat at temperature 250⁰C; (k) Alloy C – Mould preheat at temperature 300⁰C; (l) Alloy C – Mould preheat at temperature 350⁰C. The gravity vector acts on the plane of view, pointing to the right direction.

**Table 5.5: Volume and surface area of the sample, pores and cracks for Alloy A, B and C at four different mould preheat temperatures.**

Alloy	ID	Mould Preheat T (⁰C)	Total Volume (mm³)	Surface Area (mm²)	L_c (mm)	Pores Vol. (mm³)	Pores S.A. (mm²)	Crack Vol. (mm³)	Crack S.A. (mm²)
A	a	200	1147.23	656.72	1.75	8.70	188.46	2.94	47.97
A	b	250	1166.22	672.71	1.73	1.18	38.37	6.50	129.01
A	c	300	1164.83	667.56	1.74	6.06	129.12		
A	d	350	1161.67	662.77	1.75	2.53	87.33	1.04	36.12
B	e	200	1166.70	686.96	1.70	4.91	111.34		
B	f	250	1162.01	667.94	1.74	5.71	118.92		
B	g	300	1155.45	656.33	1.76	0.68	20.99		
B	h	350	1151.46	651.40	1.77	2.60	85.53		
C	i	200	1164.25	675.23	1.72	4.59	157.71		
C	j	250	1161.23	664.70	1.75	6.41	202.97		
C	k	300	1160.78	674.93	1.72	3.34	117.99		
C	l	350	1145.81	655.26	1.75	5.04	174.86		

The results presented in the Figure 5.29 (a) to (l) show the presence of accumulated gas porosity from entrapped air and dissolved hydrogen in the melt, at the upper part of the

sample, as expected, due to gravity. Since the volume of the pores is less than 1% of the total volume, their data value were not included in further calculations and analyses.

Notably, in Figure 5.29 (a) - (l), the blue image shows the section of the samples investigated and analyzed, such that the height and location of this section was identical in all alloys and mould temperatures, so as to compare the radial shrinkage of the various experiments. Further, the CT Scan showed to be an efficient tool to analyze hot tearing volume and porosity, except that the hairline hot tears and shrinkage voids were not captured by the bulk CT instrument due to the lack of resolution of the same.

Figure 5.30 shows the total volume and surface area obtained from Table 5.5; wherein, increasing the mould preheat resulted in a decrease of the image volume and surface area, or, an increase in radial shrinkage of the samples. At a higher mould preheat temperature, the cooling rate is lower, which translates to a slower rate of heat extraction during solidification, leading to improved liquid feedability and lesser HTS, resulting in a smaller volume and surface area. Notably, in Figure 5.30, Alloy A at a 200 ºC mould preheat temperature showed an anomalous behaviour, which may be attributed to a significant hot tear, reducing the volume and surface area. When there is a lower mould preheat temperature, the heat extraction is faster and the shrinkage is trapped within the intergranular regions of the solidifying primary α(Al) phases as micro-voids, thus, resulting in a higher volume and surface area. However, as the mould preheat temperature increases, reducing the rate of heat extraction during solidification, the shrinkage is pushed out towards the riser of the casting, resulting in a more compact casting with decreasing volume and surface area.
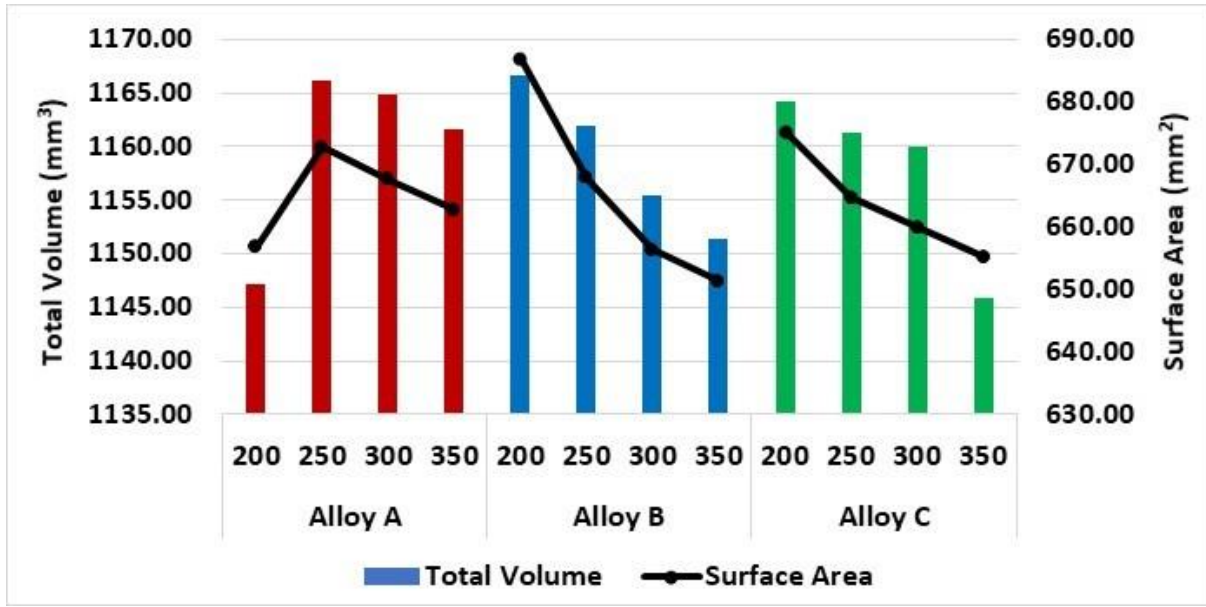
Figure 5.30: Total volume and surface area of Alloy A, Alloy B and Alloy C hot tearing samples according to mould preheat temperature.

5.5.   Limiting Condition for Hot Tearing in CRS Experiments

Further analyses of the competing phenomena of stress acting in location *TC2* and the feedability of solidification shrinkage at the same location from the liquid in the riser, through the location *TC1* was carried out to quantify the reasons for HTS in these alloys. Table 5.6 presents some of the critical data extracted from the CTS experiment curves at the *coas* stage (t$_{coas}$), shown in Figure 5.11 to Figure 5.23, so as to facilitate the analyses of HTS in these alloys: the fraction solid at location *TC1*, the axial stress at location *TC2* and mean cooling rate $\left(\frac{T_{Liquidus}-TC1}{t}\right)$ up until the t$_{coas}$, all as a function of t$_{coas}$. Figure 5.31 show the graphical representation of the data in Table 5.6.

.

Table 5.6: Critical data extracted from the curves at t_{coas} in Figure 5.11 to Figure 5.22.

Alloy	Mould Preheat T (°C)	t_{coas} (s)	f_s at *TC1*	σ at *TC2*	Mean Cooling Rate at *TC1*
A	200	14.31	0	3.95	16.7
	250	17.25	0.12	3.25	15.1
	300	19.63	0.55	2.42	14.4
	350	24.45	0.87	1.73	11.3
B	200	14.71	0	5.15	16.2
	250	15.52	0.05	4.08	14.0
	300	18.54	0.22	3.35	12.1
	350	23.69	0.64	2.24	11.7
C	200	10.82	0.01	4.53	18.1
	250	14.24	0.04	3.88	15.8
	300	17.05	0.16	3.20	15.4
	350	20.23	0.17	2.37	13.7
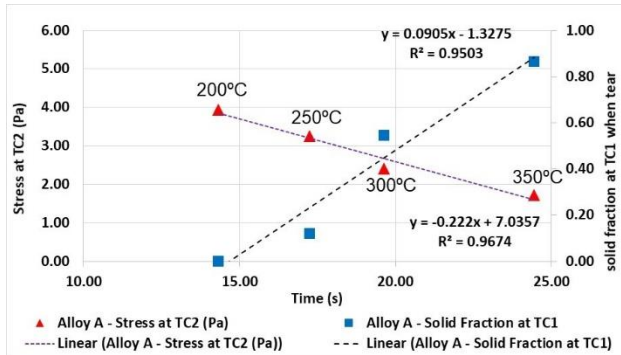
(a)
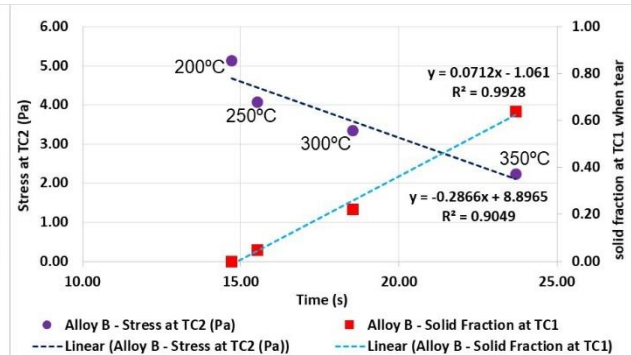
(b)
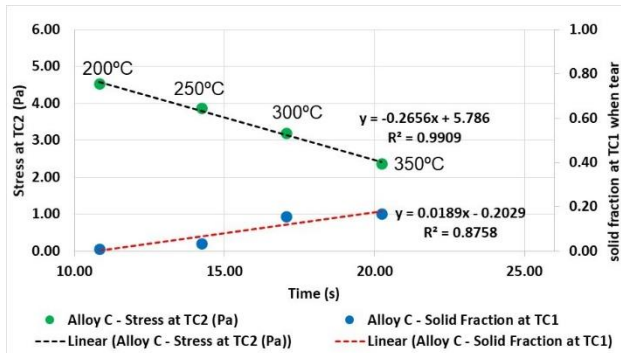
(c)
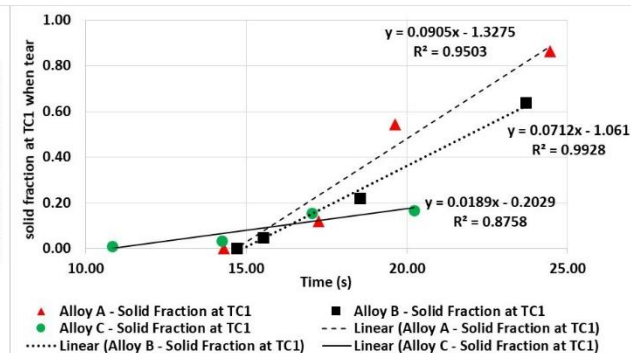
(d)
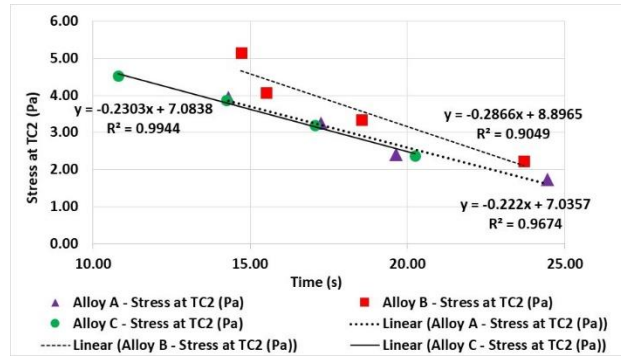
(e)

Figure 5.31: Graphs of the critical parameters in Table 5.6 for the CTS experiments. (a) stress at *TC2* and f_s at *TC1* as a function of time for Alloy A, (b) stress at *TC2* and f_s at *TC1* as a function of time for Alloy B, (c) stress at *TC2* and f_s at *TC1* as a function of time for Alloy C, (d) f_s at *TC1* as a function of time for the three alloys and (e) stress at *TC2* as a function of time for the three alloys. In all the graphs, the data points for the respective alloys have increasing mould preheat temperature (decreasing mean cooling rate) from the left to right (for increasing time values).

Figure 5.1 shows the path of liquid feeding from the riser in the casting to the critical location *TC2*, through the location *TC1*. Typically, when the location *TC2* reaches the *coas* stage, the feeding for the final stages of solidification would occur from the location *TC1*, as the other volume of metal around this region would be more solidified than that in *TC1*. Hence, the path of feeding to prevent hot tearing in *TC2* would be from the location *TC1*.

Figure 5.31 (a) shows that in Alloy A, the t_{coas} at *TC2* increases with increasing mould preheat temperatures, as anticipated, while the σ_{TC2} decreases as the mould preheat temperature increases. The mould preheat temperature is inversely proportional to the mean cooling rates of the solidification. Hence, with decreasing mean cooling rate until

103

the *coas* stage, the $t_{coas,TC2}$ increases and σ_{TC2} decreases. A similar trend has been observed for Alloy B and Alloy C, as shown in Figure 5.3 (b) and (c), respectively. Further, the solid fraction at *TC2* at t_{coas} is >0.97 for all alloy cases, while the $f_{s@TC1}$ increases with decreasing cooling rate (increasing mould preheat temperature). At the highest cooling rates (200 °C mould preheat temperature), the $f_{s@TC1}$ for all the three alloys are the same and nearly zero (0), showing that the alloy in location *TC1*, just begins to solidify at t_{coas}. However, the time taken to reach this solid fraction at *TC1* decreases from Alloy C to Alloy B to Alloy A.

The constrained solidification mechanism in Alloy A and Alloy B, maintains a defined solid/liquid front moving against the direction of heat extraction, while unconstrained solidification in Alloy C (grain refined) leads to the nucleation and growth of stable $\alpha(Al)$ phase well ahead of the progressing solid/liquid interface during solidification. Hence, the t_{coas} for Alloy C is significantly lower than that for Alloy A and Alloy B. Further, the well-distributed equiaxed dendrites in Alloy C when compared to the columnar dendritic grains of reaches $\alpha(Al)$ phase in both Alloy A and Alloy B, results in a significantly lower value of $f_{s@TC1}$ for Alloy A, while that for Alloy B is greater than Alloy C but less than Alloy A, for the respective mould preheat temperature (mean cooling rate). Hence, the permeability of the Alloy C at location *TC1*, during t_{coas} would be far greater than that for Alloy B, which would be greater than that in Alloy A for the same mean cooling rate (mould preheat). Hence, at t_{coas}, the liquid feedability from location *TC1* to *TC2* would be highest in Alloy C, followed by that in Alloy B and the lease in Alloy A.

Further, the σ_{TC2} for the three alloys at the various mould preheat temperatures, shown in Figure 5.31, is comparable with each other in magnitude, with Alloy B and Alloy C being

marginally higher than that for Alloy A; the solidification stresses at $t_{coas,TC2}$ would be deemed as nearly the same for a particular mould preheat temperature condition. Hence, the critical factor that would determine the HTS of the alloy in a CTS experiment would be the permeability of the liquid feeding path between locations *TC1* and *TC2*, which is increasing from Alloy A to Alloy B and further to Alloy C, showing that the HTS will decrease among the alloys, in that order. Alloy C showed no HTS while that for Alloy A was the highest. Alloy B showed marginal hairline cracks instead of a tear.

Figure 5.32 (a) and (b) shows a typical light optical microstructure of Alloy A and Alloy B, respectively, along with the photograph of the nature of hot tear in the respective castings at location *TC2*. The defect in Alloy A could be classified as a hot tear, as confirmed by the CT images in Figure 5.29, wherein the tear initiates and grows at around the t_{coas}, as confirmed by the presence of increasing density of the σ(Al, Zn, Mg) phases on the primary α(Al) phase matrix, towards the final stages of solidification, bounding the tear region; the hot tear could also be seen in the photograph of the casting, as well. In Figure 5.32 (b), the defect in the Alloy B is more of connected shrinkage voids, which have a higher concentration of the eutectic phases of α(Al) + $Al_{13}Fe_4$ phases that have formed within the sections of shrinkage voids, that was healed during the *coas* stage of solidification in these alloys, due to the presence of about 3 % excess liquid. Further, there are a presence of micro-voids from solidification shrinkage within the primary α(Al) grains in the matrix of the two alloys, caused by localized disruption of liquid feeding to compensate shrinkage, arising from a dendritic constrained growth pattern of the primary Al phase during solidification.
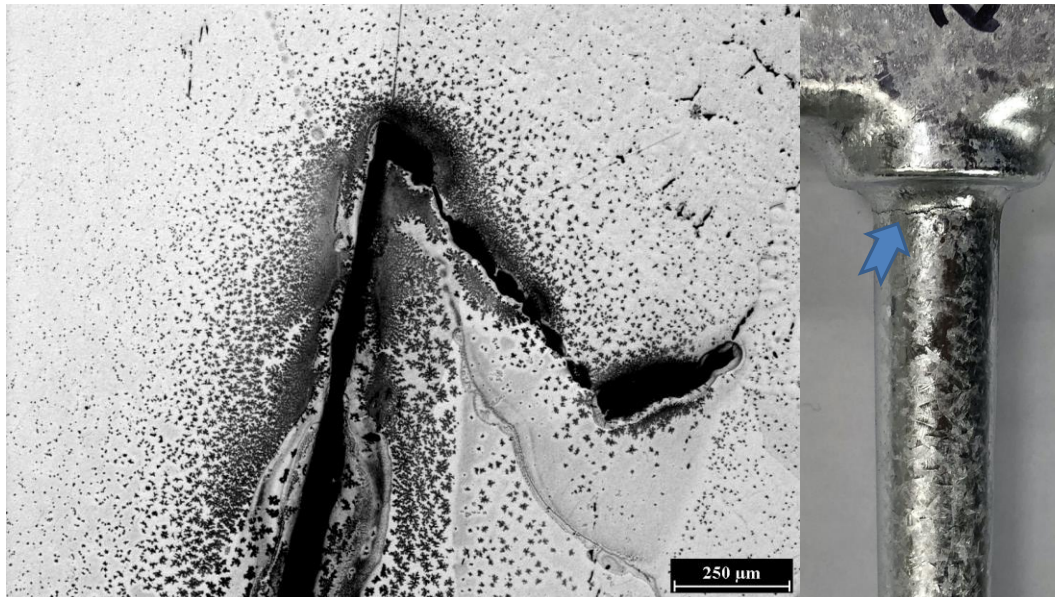
(a)
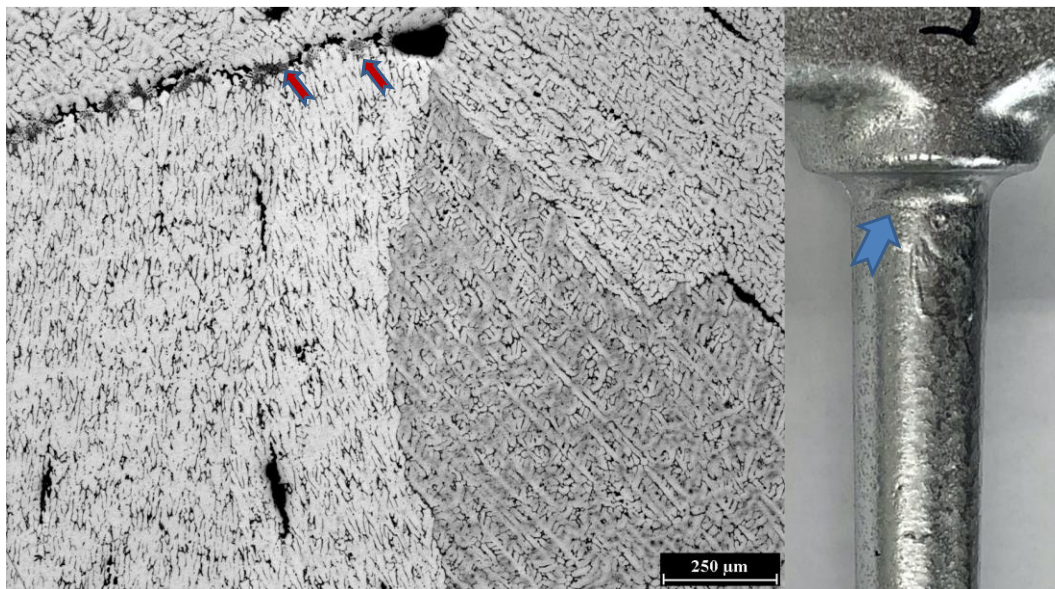
(b)

Figure 5.32: Typical light optical microstructure and photograph of casting at location *TC2* for (a) alloy A and (b) Alloy B. It is also shown a typical hot tear in Alloy A and stable shrinkage voids in Alloy B after solidification. The evolution of the secondary Al$_{13}$Fe$_4$ phase from the liquid at t$_{coas}$ facilitates local healing of the shrinkage voids as shown by red arrows in (b).

Presently, Alloy C is been commercialized by Nemak US/Can corporation as Nemalloy HE700, and this alloy has been successfully validated to be used in manufacturing structural automotive components using the high vacuum high-pressure die casting process, with superior properties and performance to the existing Al-Si-Mg structural alloys [41].

CHAPTER 6. *CONCLUSIONS AND FUTURE WORK*

There are two salient topics of study in this work, namely, the improvement to the constrained rod solidification (CRS) experiments and the mechanism for hot tearing susceptibility for the three alloys used in the study, namely, Alloy A (Al-4 wt%Zn-1 wt%Mg), Alloy B (Al-4 wt%Zn-1 wt%Mg–*1.2 wt%Fe)*, and Alloy C (Al-4 wt%Zn-1 wt%Mg-*1.2 wt%Fe–0.1 wt%Ti)*.

❖ The improvements made to the CRS experiments proved to be beneficial in obtaining a repeatable response to the data acquired from the experiments, namely, transient temperature, load and displacement, alike.

❖ In Alloy C, at the coalesce stage, the liquid remaining would have a significantly higher content of Fe (~0.45), as shown in Table 5.2, when compared with Alloy B, because the $Al_{13}Fe_4$ phase does not evolve in tandem with the α(Al), as in Alloy B, but the Fe accumulates in the liquid in the interdendritic regions of the equiaxed dendrites until the final invariant temperature is reached when the eutectic phases evolve. In this scenario, the feedability of the final stages of solidification of Alloy C from the nearly 4 vol% of liquid, would be significantly higher than that in Alloy B and Alloy A; hence, Alloy C would have the lowest HTS among the three, and additions of Fe and Ti additions increase resistance to hot tear.

❖ The stress-strain curves for the three alloys during solidification were derived from the experimental data. The curve has four major regimes of interest:

- At t < t_{coh}; the stress is negligible and the $\frac{d\sigma}{d\varepsilon}$ is also negligible.

- At $t_{coh} < t < t_{coas}$, the stress increases due to constrained liquid feeding of the solidifying section between locations *TC2* and *TC3*.

- At $t_{coas} < t < t_{end}$, the stress relaxation occurs wherein the final liquid solidified with a notable reduction in $\frac{d\sigma}{d\varepsilon}$ to a constant value, as well.

- At $t > t_{end}$, the stress increases with strain as the solid reduces temperature and the value of $\frac{d\sigma}{d\varepsilon}$ is constant; akin to thermal contraction of the solid.

❖ The HTS is maximum at location *TC2*, and the probability of the tear initiation is maximum when this location reaches the *coalesce* stage at t_{coas}. When *TC2* reaches t_{coas}, the limiting factor for hot tearing is the stress and strain rate acting on the solidifying microstructure at this location due to the rate of shrinkage, enabling the hot tear, while, the liquid feeding into location *TC2* from *TC1* counters this by attempting to heal the shrinkage voids. The solidification stresses at coalesce for all the three alloys are nearly similar, however, the ability to feed the location and heal voids at *TC2* increases significantly from Alloy A to Alloy B and to Alloy C, for a particular cooling rate of solidification (mould preheat temperature) and this difference in feedability at t_{coas} also increases significantly with increasing mould preheat temperature (decreasing the mean cooling rate of solidification).

❖ The Computerized Tomography (CT) Imaging was successfully used to detect large hot tears in Alloy A but the resolution was not good enough to detect the hairline tears in Alloy B. Further, the CT Imaging data also provided a precise evaluation of the radial shrinkage of the solidifying section between *TC2* and *TC3* locations, within the cylindrical section of the mould.

6.1.   Future Work

Continuation of the data analyses to explore the several relationships between the stress, strain, thermal and temporal fields may yield a quantified HTS criterion for the CRS experiments. The variation of solid fraction as a function of temperature was simulated using the Scheil-Gulliver (S-G) paradigm and may not be representative of the real scenario occurring in the solidification experiments. Uni-directional solidification experiments within the cooling rate regimes of the CRS experiments to evaluate the actual relationship between f_s and T would vastly improve the accuracy and predictability of the HTS.   An in-depth analysis of the microstructure using light optical and electron microscopes could not be carried due to time constraints and lack of availability of equipment. Such an in-depth analysis would further establish and hone the mechanisms of hot tearing in alloys with unconstrained and constrained growth of the primary Al phase in them.

REFERENCES

[1] U. Nations, World Population Prospects 2019, 2019. http://www.ncbi.nlm.nih.gov/pubmed/12283219.

[2] P. Bastani, J. Heywood, C. Hope, US CAFE STANDARDS, (2012) 2016–2025. http://web.mit.edu/sloan-auto-lab/research/beforeh2/files/CAFE_2012.pdf (accessed May 7, 2013).

[3] C. Li, I.Y. Kim, Multi-material topology optimization for automotive design problems, Proc. Inst. Mech. Eng. Part D J. Automob. Eng. 232 (2018) 1950–1969. https://doi.org/10.1177/0954407017737901.

[4] J. Rowe, Introduction: Advanced materials and vehicle lightweighting, Adv. Mater. Automot. Eng. (2012) 1–4. https://doi.org/10.1533/9780857095466.

[5] Ducker Worldwide Report, Aluminum Content in North American Light Vehicles 2016 To 2028, (2017) 1–46. http://www.ducker.com/sites/default/files/protected-files/Aluminum Content in North American Light Vehicles 2016 to 2028 - Summary Report (1) (1).pdf.

[6] Ducker Worldwide, Metallic Material Trends in the North American Light Vehicle Ducker Worldwide Introduction, 2015. http://www.autosteel.org/.

[7] The Aluminium Association, International Alloy Designations and Chemical Composition Limits for Wrought Aluminum and Wrought Aluminum Alloys., Alum. Assoc. Arlington, Virginia. (2015) 31. https://www.aluminum.org/sites/default/files/Teal Sheets.pdf.

[8] J.R. Davis, Light Metals and Alloys-Aluminum and Aluminum Alloys, Alloy. Underst. Basics. (2001) 351–416. https://doi.org/10.1361/autb2001p351.

[9] H.I. Laukli, High Pressure Die Casting of Aluminium and Magnesium Alloys - Grain Structure and Segregation Characteristics, 2004. http://urn.kb.se/resolve?urn=urn:nbn:no:ntnu:diva-379%5Cnhttps://drive.google.com/open?id=0B0fTxDBXtHZMdVVpMHNJU0lRLXc.

[10] M.A. Farooq, R. Roth, R. Kirchain, Lightweighting technologies: Analyzing strategic and economic implications of advanced manufacturing processes, Int. J. Prod. Econ. 206 (2018) 268–279. https://doi.org/10.1016/j.ijpe.2018.10.003.

[11] L.X. Kong, F.H. She, W.M. Gao, S. Nahavandi, P.D. Hodgson, Integrated optimization system for high pressure die casting processes, J. Mater. Process. Technol. 201 (2008) 629–634. https://doi.org/10.1016/j.jmatprotec.2007.11.250.

[12] M.S. Dargusch, G. Dour, N. Schauer, C.M. Dinnis, G. Savage, The influence of pressure during solidification of high pressure die cast aluminium telecommunications components, J. Mater. Process. Technol. 180 (2006) 37–43. https://doi.org/10.1016/j.jmatprotec.2006.05.001.

[13]   G. Birsan, Private Communication, (2020).

[14]   M. Hartlieb, Structural Die Casting, (1814).

[15]   J. Vann, From Simulation to Process Automation – "Define It And Do It," Die Cast. Eng. (2011) 33–39. https://doi.org/10.1111/ajco.12362.

[16]   Ducker Worldwide, 2015 North American Light Vehicle Aluminum Content Study, (2015) 1–24. http://www.ducker.com.

[17]   Y. He, S. Li, K. Sadayappan, D. Apelian, Thermomechanical simulation and experimental characterisation of hot tearing during solidification of aluminium alloys, Int. J. Cast Met. Res. 26 (2013) 72–81. https://doi.org/10.1179/1743133611Y.0000000028.

[18]   N. Hatami, R. Babaei, M. Dadashzadeh, P. Davami, Modeling of hot tearing formation during solidification, J. Mater. Process. Technol. 205 (2008) 506–513. https://doi.org/10.1016/j.jmatprotec.2007.11.260.

[19]   L. Sweet, M.A. Easton, J.A. Taylor, J.F. Grandfield, C.J. Davidson, L. Lu, M.J. Couper, D.H. Stjohn, Hot tear susceptibility of Al-Mg-Si-Fe alloys with varying iron contents, Metall. Mater. Trans. A Phys. Metall. Mater. Sci. 44 (2013) 5396–5407. https://doi.org/10.1007/s11661-012-1562-1.

[20]   M. Rappaz, J.M. Drezet, M. Gremaud, A new hot-tearing criterion, Metall. Mater. Trans. A Phys. Metall. Mater. Sci. 30 (1999) 449–455. https://doi.org/10.1007/s11661-999-0334-z.

[21]   Pumphrey, W.I. and Lyons, J.V., Cracking During the Casting and Welding of the More Common Binary Aluminum Alloys, J. Inst. Met. 1118 (1948) 439–455.

[22]   A.S. Sabau, S. Mirmiran, C. Glaspie, S. Li, D. Apelian, A. Shyam, J.A. Haynes, A.F. Rodriguez, Hot-Tearing of Multicomponent Al-Cu Alloys Based on Casting Load Measurements in a Constrained Permanent Mold, TMS 2017 146th Annu. Meet. Exhib. Suppl. Proc. (2017) 465–473. https://doi.org/10.1007/978-3-319-51493-2.

[23]   X. Zeng, C. Ferguson, Assandra, K. Sadayappan, S. Shankar, Effect of Titanium Levels on the Hot Tearing Sensitivity and Abnormal Grain Growth After T4 Heat Treatment of Al–Zn–Mg–Cu Alloys, Int. J. Met. 12 (2018) 457–468. https://doi.org/10.1007/s40962-018-0227-2.

[24]   J.A. Grandfield, J. F., Davidson, C. J., & Taylor, Application of a new hot tearing analysis to horizontal direct chill cast magnesium alloy AZ91, Contin. Cast. (2000) 205–210. https://onlinelibrary.wiley.com/doi/abs/10.1002/3527607331.ch30.

[25]   R. Ghiaasiaan, S. Shankar, Microstructure, Intermetallic Phases, and Fractography of the Cast Al-5.8Zn-2.2Mg-2.5Cu Alloy by Controlled Diffusion Solidification, Metall. Mater. Trans. A Phys. Metall. Mater. Sci. 51 (2020) 4711–4726. https://doi.org/10.1007/s11661-020-05885-z.

[26]   D. Warrington, D.G. McCartney, Hot-cracking in aluminium alloys 7050 and 7010— a comparative study, Cast Met. 3 (1990) 202–208.

[27] G.J. Clyne, T.W., Davies, Solidification and Casting of Metals, (1979) 275–278.

[28] M. Easton, H. Wang, J. Grandfield, D. StJohn, E. Sweet, An analysis of the effect of grain refinement on the hot tearing of aluminium alloys, Mater. Forum. 28 (2004) 224–229.

[29] D.J. Lahaie, M. Bouchard, Physical modeling of the deformation mechanisms of semisolid bodies and a mechanical criterion for hot tearing, Metall. Mater. Trans. B Process Metall. Mater. Process. Sci. 32 (2001) 697–705. https://doi.org/10.1007/s11663-001-0124-5.

[30] I.I. Novikov, Hot-Shortness of Nonferrous Metals and Alloys, FOREIGN TECHNOLOGY DIV WRIGHT-PATTERSON AFB OHIO, 1968.

[31] S. Li, D. Apelian, Hot Tearing of Aluminum Alloys a Critical Literature Review, Am. Foundry Soc. (2011) 23–40.

[32] G.J. Clyne, T.W., Davies, A Quantitative Solidification Cracking Test for Castings and an Evaluation of Cracking in Aluminium-Magnesium Alloys, Br. Foundryman. 68 (1975) 238.

[33] K. Strobel, M.A. Easton, V. Tyagi, M. Murray, M.A. Gibson, G. Savage, T.B. Abbott, Evaluation of castability of high pressure die cast magnesium based alloys, Int. J. Cast Met. Res. 23 (2010) 81–91. https://doi.org/10.1179/136404609X12535244328332.

[34] M.A. Easton, M.A. Gibson, M. Gershenzon, G. Savage, V. Tyagi, T.B. Abbott, N. Hort, Castability of some Magnesium Alloys in a Novel Castability Die, Mater. Sci. Forum. 690 (2011) 61–64. https://doi.org/10.4028/www.scientific.net/MSF.690.61.

[35] M. Easton, J. Grandfield, D. Stjohn, B. Rinderer, The effect of grain refinement and cooling rate on the hot tearing of wrought aluminium alloys, Mater. Sci. Forum. 519–521 (2006) 1675–1680. https://doi.org/10.4028/www.scientific.net/msf.519-521.1675.

[36] S. Li, K. Sadayappan, D. Apelian, Role of grain refinement in the hot tearing of cast Al-Cu alloy, Metall. Mater. Trans. B. 44 (2013) 614–623.

[37] T.A. Davis, L. Bichler, F. D'Elia, N. Hort, Effect of TiBor on the grain refinement and hot tearing susceptibility of AZ91D magnesium alloy, J. Alloys Compd. 759 (2018) 70–79. https://doi.org/10.1016/j.jallcom.2018.05.129.

[38] F.D. Elia, A study of hot tearing during solidification of B206 Aluminium alloy, (2015).

[39] Q.L. Bai, Y. Li, H.X. Li, Q. Du, J.S. Zhang, L.Z. Zhuang, Roles of Alloy Composition and Grain Refinement on Hot Tearing Susceptibility of 7××× Aluminum Alloys, Metall. Mater. Trans. A Phys. Metall. Mater. Sci. 47 (2016) 4080–4091. https://doi.org/10.1007/s11661-016-3588-2.

[40] A. Mazahery, SHAPE CASTING HIGH STRENGTH Al-Zn-Mg-Cu ALLOYS: INTRODUCING COMPOSITION-BEHAVIOR RELATIONSHIPS, McMaster University, Hamilton - ON, Canada, 2016.

[41]   C. Wu, Quantitative Metallography, Optimization of HVHPC Process and Modelling Solute Homogenization During Solutionizing of Al-4Zn-1Mg-1.2Fe-0.1Ti Alloy, McMaster University, Hamilton - ON, Canada, 2019.

[42]   Z. Zhang, G. Li, X.G. Chen, Effect of nickel and vanadium on iron bearing intermetallic phases in AA 5657 simulated DC castings, Mater. Sci. Technol. (United Kingdom). 30 (2014) 951–961. https://doi.org/10.1179/1743284713Y.0000000376.

[43]   L. Sweet, S.M. Zhu, S.X. Gao, J.A. Taylor, M.A. Easton, The effect of iron content on the iron-containing intermetallic phases in a cast 6060 aluminum alloy, Metall. Mater. Trans. A Phys. Metall. Mater. Sci. 42 (2011) 1737–1749. https://doi.org/10.1007/s11661-010-0595-6.

[44]   J. Verö, The hot-shortness of aluminum alloys, Met. Ind. 48 (1936) 431–434.

[45]   M.O. Pekguleryuz, P. Vermette, A study on hot-tear resistance of magnesium diecasting alloys, Trans. Am. Foundry Soc. Vol. 114. 114 (2006) 729–736.

[46]   D.G. Eskin, L. Katgerman, Effect of Structure on Hot Tearing Properties of Aluminum Alloys, Mater. Sci. Forum. 561–565 (2007) 995–998. https://doi.org/10.4028/www.scientific.net/msf.561-565.995.

[47]   L. Lu, A.K. Dahle, Iron-Rich Intermetallic Phases and Their Role in Casting Defect Formation in Hypoeutectic Al-Si Alloys, Metall. Mater. Trans. A. 36 (2005) 819–835.

[48]   K. Liu, X. Cao, A. Bolouri, X.-G. Chen, Effect of Fe-Rich Intermetallics on Tensile Behavior of Al–Cu 206 Cast Alloys at Solid and Near-Solid States, (2019) 85–96. https://doi.org/10.1007/978-3-030-06034-3_8.

[49]   A. Barbucci, P.L. Cabot, G. Bruzzone, G. Cerisola, Role of intermetallics in the activation of Al-Mg-Zn alloys, J. Alloys Compd. 268 (1998) 295–301. https://doi.org/10.1016/S0925-8388(97)00605-1.

[50]   Z. Zhang, G. Li, X.-G. Chen, Identification and Distribution of Fe Intermetallic Phases in AA 5657 DC Cast Ingots, in: ICAA13 Pittsburgh, Springer, 2012: pp. 1857–1863.

[51]   L. Bichler, A. Elsayed, K. Lee, C. Ravindran, Influence of mold and pouring temperatures on hot tearing susceptibility of AZ91D magnesium alloy, Int. J. Met. 2 (2008) 43–54. https://doi.org/10.1007/BF03355421.

[52]   S. Li, K. Sadayappan, D. Apelian, Effects of Mold Temperature and Pouring Temperature on the Hot Tearing of Cast Al-Cu Alloys, Metall. Mater. Trans. B Process Metall. Mater. Process. Sci. 47 (2016) 2979–2990. https://doi.org/10.1007/s11663-016-0739-1.

[53]   K. Singer, H. Benek, Contribution to hot tears in steel castings, Stahl and Sisen. 51 (1931) 61–65.

[54]   J.M. Middleton, H.T. Protheroe, The hot-tearing of steel, J. Iron Steel Inst. 168 (1951) 384–398.

[55]   A. Couture, J.O. Edwards, The hot-tearing of copper-base casting alloys, AFS

Trans. 74 (1966) 709–721.

[56]   C.W. Briggs, The metallurgy of steel castings, McGraw-Hill book Company, Incorporated, 1946.

[57]   N.N. Prokhorov, Resistance to hot tearing of cast metals during solidification, Russ. Cast. Prod. 2 (1962) 172–175.

[58]   D.G. Eskin, Suyitno, L. Katgerman, Mechanical properties in the semi-solid state and hot tearing of aluminium alloys, Prog. Mater. Sci. 49 (2004) 629–711. https://doi.org/10.1016/S0079-6425(03)00037-9.

[59]   Suyitno, W.H. Kool, L. Katgerman, Hot tearing criteria evaluation for direct-chill casting of an Al-4.5 pct Cu alloy, Metall. Mater. Trans. A Phys. Metall. Mater. Sci. 36 (2005) 1537–1546. https://doi.org/10.1007/s11661-005-0245-6.

[60]   U. Feurer, Quality control of engineering alloys and the role of metals science, Delft Univ. Technol. Delft, Netherlands. (1977) 131–145.

[61]   J. Song, F. Pan, B. Jiang, A. Atrens, M.X. Zhang, Y. Lu, A review on hot tearing of magnesium alloys, J. Magnes. Alloy. 4 (2016) 151–172. https://doi.org/10.1016/j.jma.2016.08.003.

[62]   G.J. Clyne, T. W., & Davies, The influence of composition on solidification cracking susceptibility in binary alloy systems, Br. Foundryman. 74 (1981) 65–72.

[63]   L. Katgerman, A Mathematical Model for Hot Cracking of Aluminum Alloys During D.C. Casting, JOM J. Miner. Met. Mater. Soc. 34 (1982) 46–49. https://doi.org/10.1007/BF03339110.

[64]   S. Li, Hot Tearing in Cast Aluminum Alloys: Measures and Effects of Process Variables, 2011. https://doi.org/10.4028/www.scientific.net/MSF.690.355.

[65]   S. Shankar, Private communications, (2020).

[66]   G. Gottardi, A. Pola, G.M. La Vecchia, Solid fraction determination via DSC analysis, Metall. Ital. 107 (2015) 11–16.

[67]   J. Sokolowski, W. Kierkus, P. Marchwica, Fraction solid evolution characteristics of AlSiCu alloys - dynamic baseline approach, J. Achiev. Mater. Manuf. Eng. 47 (2011) 115–136.

[68]   M.C. Flemings, Behavior of Metal Alloys in the Semisolid State DURING dendritic solidification of castings and ingots, 22 (1991).

[69]   L.A. Alcazar-Vara, E. Buenrostro-Gonzalez, Liquid-Solid Phase Equilibria of Paraffinic Systems by DSC Measurements, Elkordy, AA Appl. Calorim. a Wide Context. Scanning Calorimetry, Isothermal Titration Calorim. Microcalorim. Rijeka InTech. (2013) 253–276. https://doi.org/10.1016/j.colsurfa.2011.12.014.

[70]   D. Emady, L.V. Whiting, M.Djurdjevic, W.T. Kierkus, J. Sokolowski, Comparison of Newtonian and Fourier thermal analysis techniques for calculation of latent heat and solid fraction of aluminum alloys, Metal. J. Metall. 10 (2004) 91–106.

https://doi.org/10.30544/379.

[71]   Ihsan-Ul-Haq, J.S. Shin, Z.H. Lee, Computer-aided cooling curve analysis of A356 aluminum alloy, Met. Mater. Int. 10 (2004) 89–96. https://doi.org/10.1007/BF03027368.

[72]   E. Fras, W. Kapturkiewicz, A. Burbielko, H.F. Lopez, A New Concept in Thermal Analysis of Castings, Trans. Am. Foundrymen's Soc. 101 (1993) 505–511. https://doi.org/10.1021/am100311m.

APPENDIX A: NORMALIZED TEMPERATURE-LOAD DISPLACEMENT CURVES FOR ALL THREE ALLOYS

The normalized transient data for temperatures, load and displacement are presented in this appendix. Notably, the legends of the graphs showing Thermocouple 1, Thermocouple 2 and Thermocouple 3 represent the data from *TC1, TC2* and *TC3*, respectively.
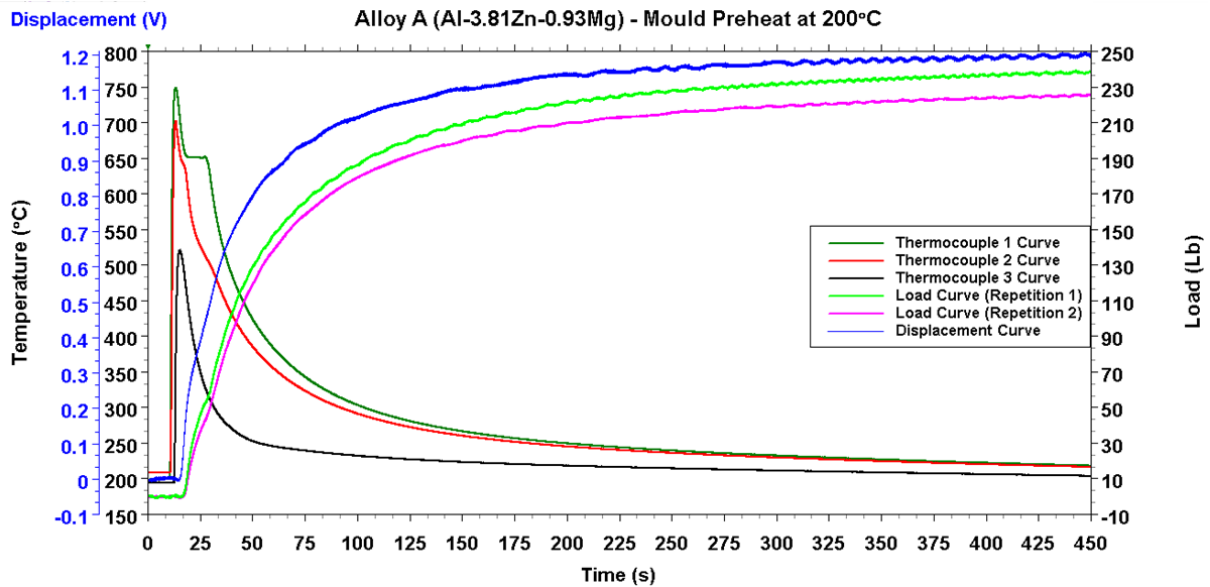
Figure A-1: Alloy A at mould preheat at 200⁰C
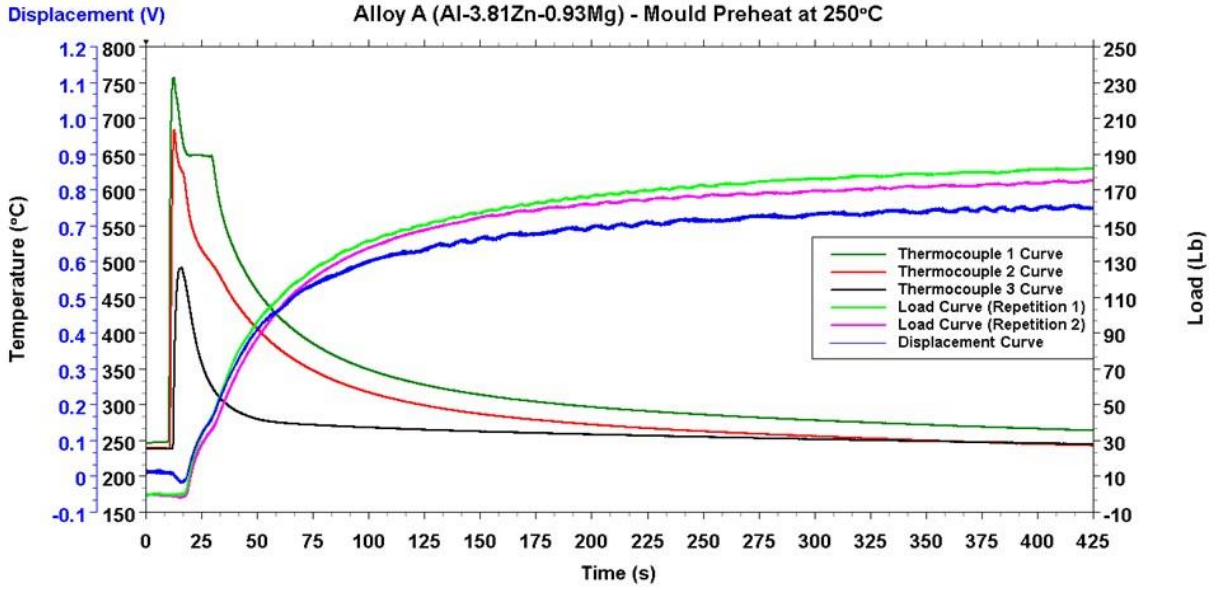
Figure A-2: Alloy A at mould preheat at 250⁰C
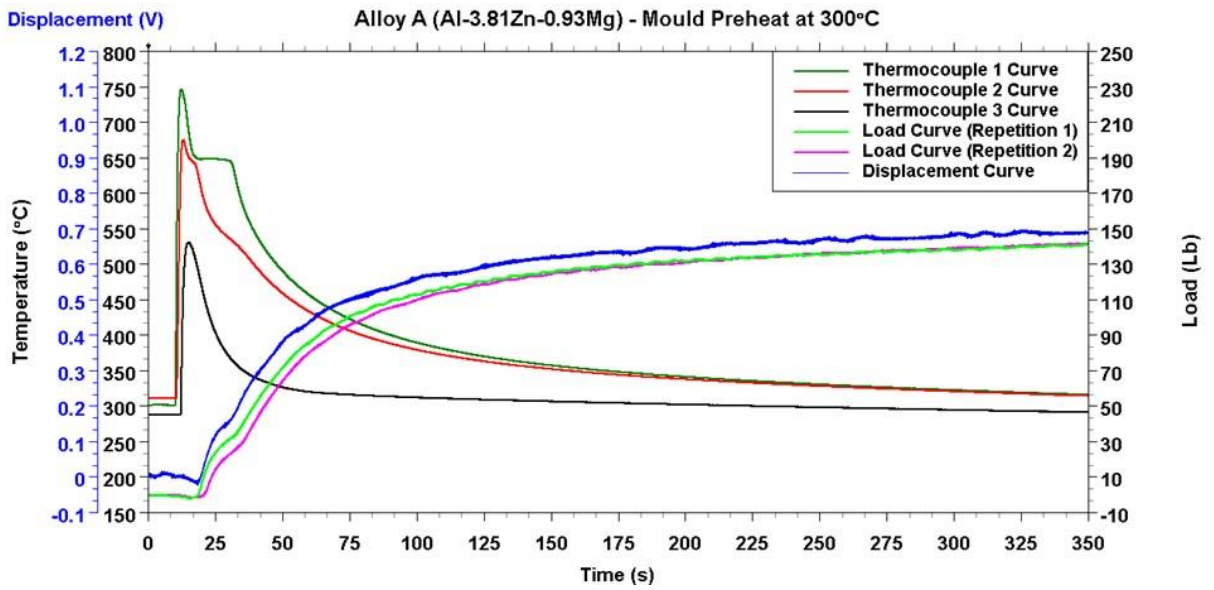
Figure A-3: Alloy A at mould preheat at 300⁰C
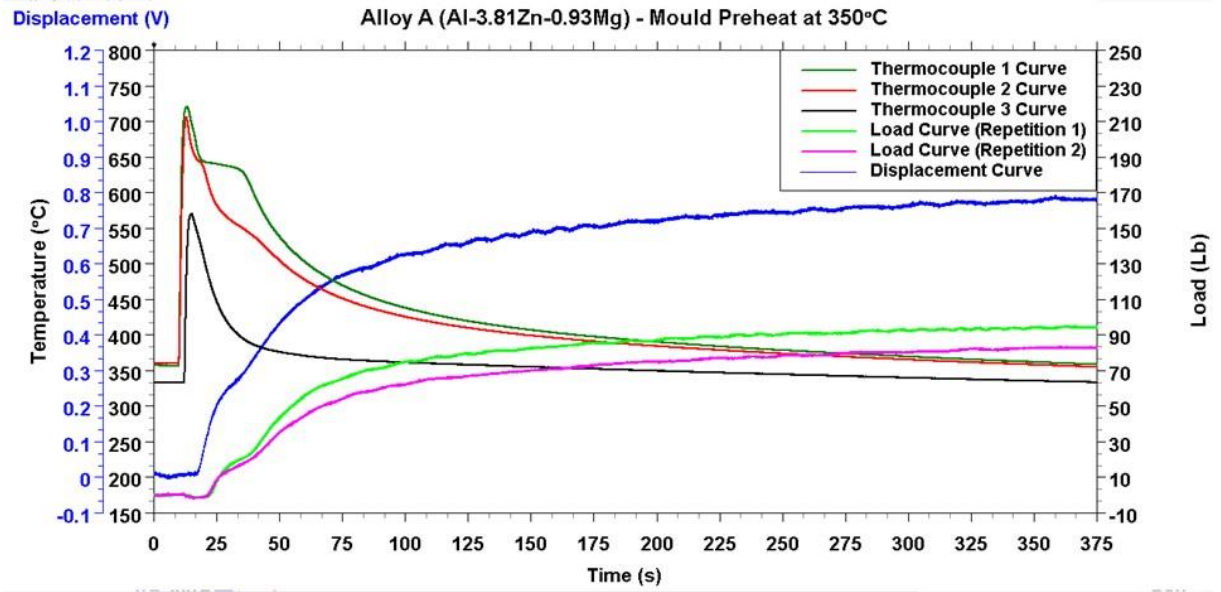
Figure A-4: Alloy A at mould preheat at 350⁰C
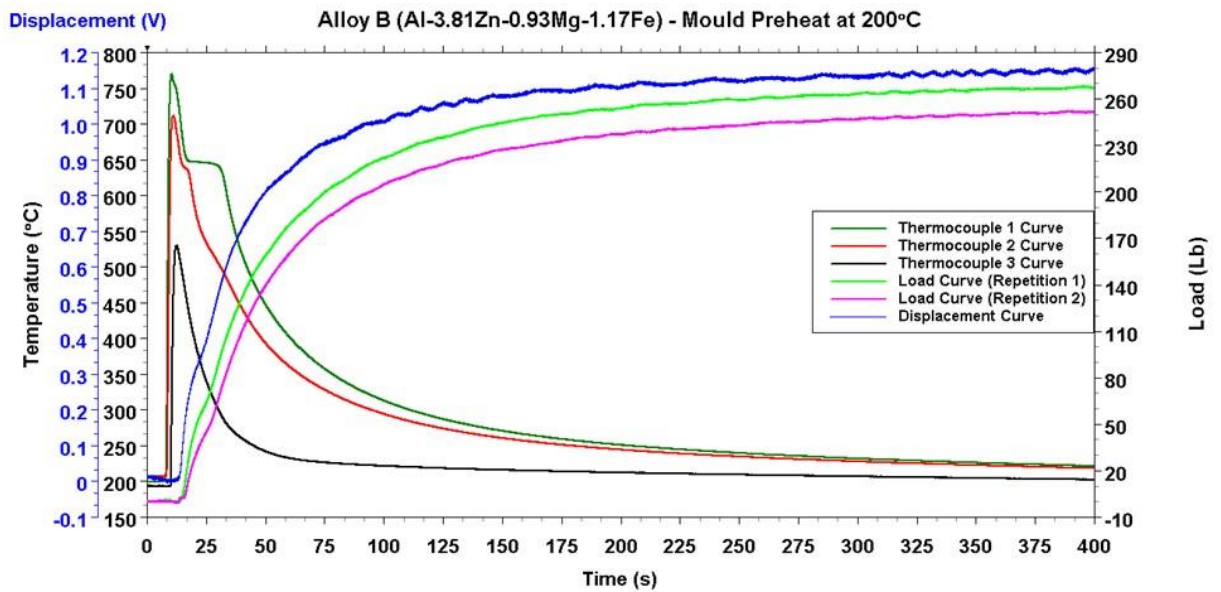
Figure A-5: Alloy B at mould preheat at 200⁰C
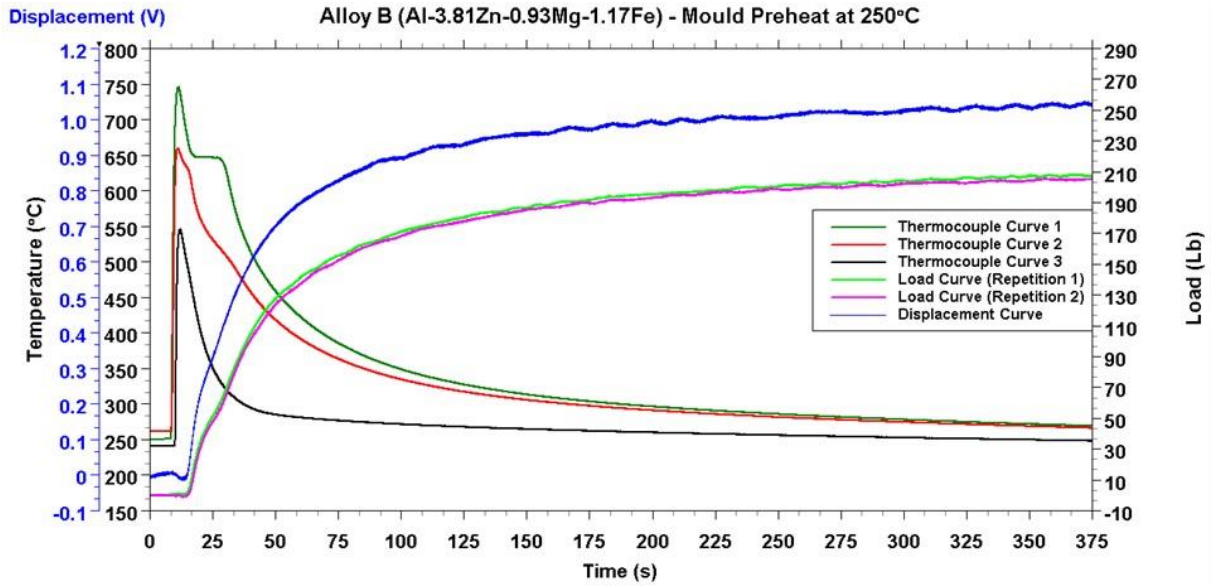
Figure A-6: Alloy B at mould preheat at 250⁰C
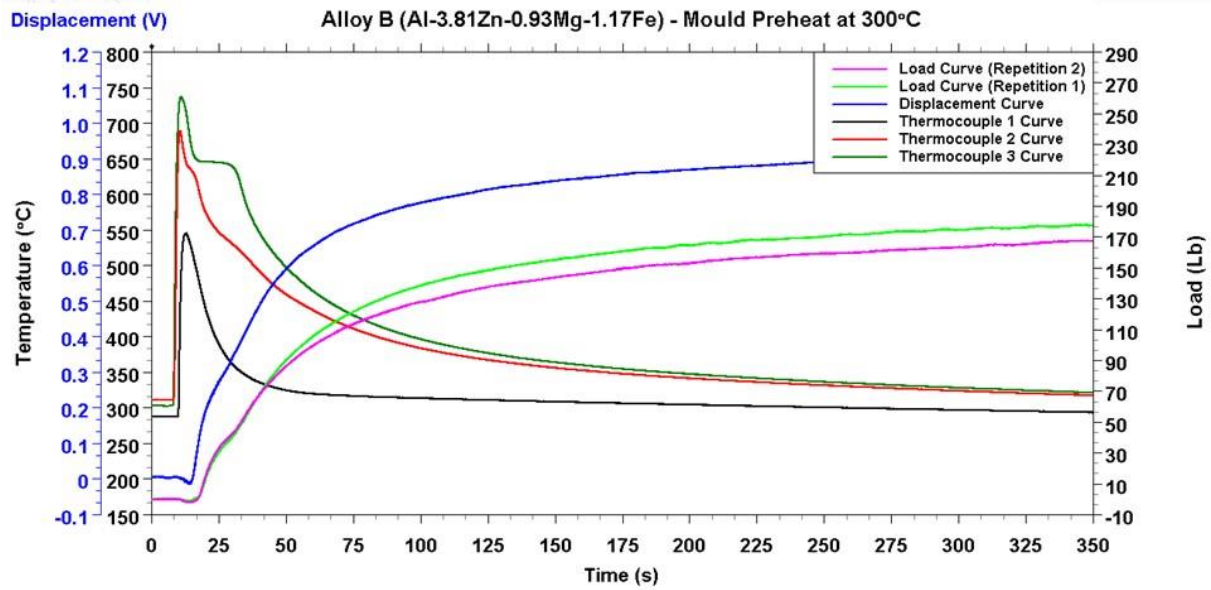
Figure A-7: Alloy B at mould preheat at 300⁰C
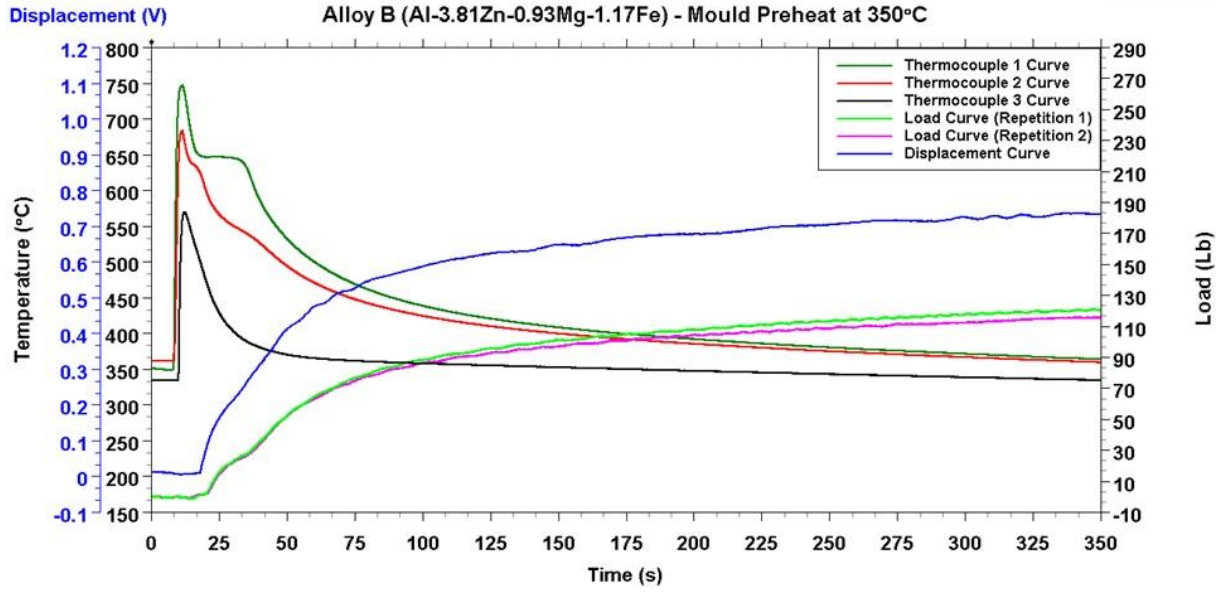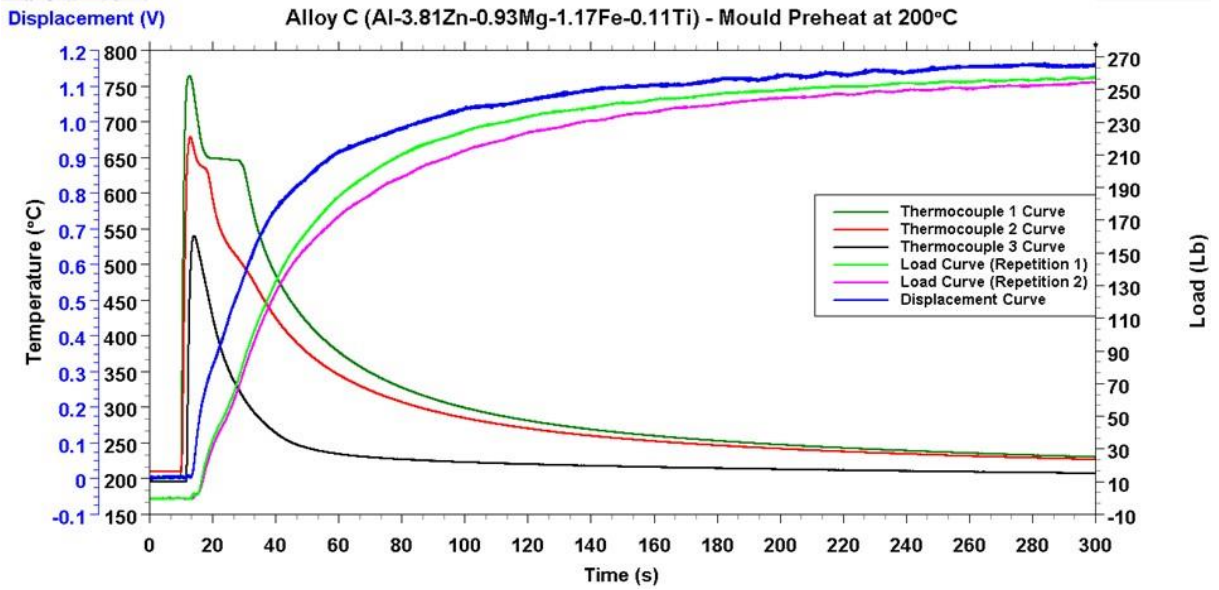
Figure A-8: Alloy B at mould preheat at 350⁰C
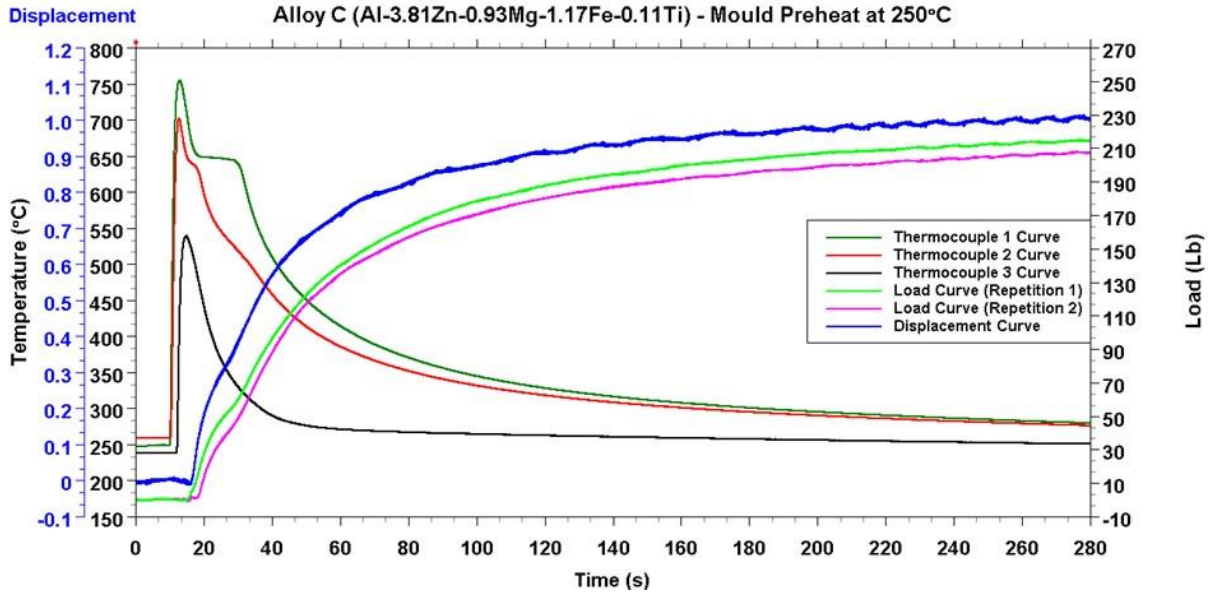

Figure A-9: Alloy C at mould preheat at 200⁰C
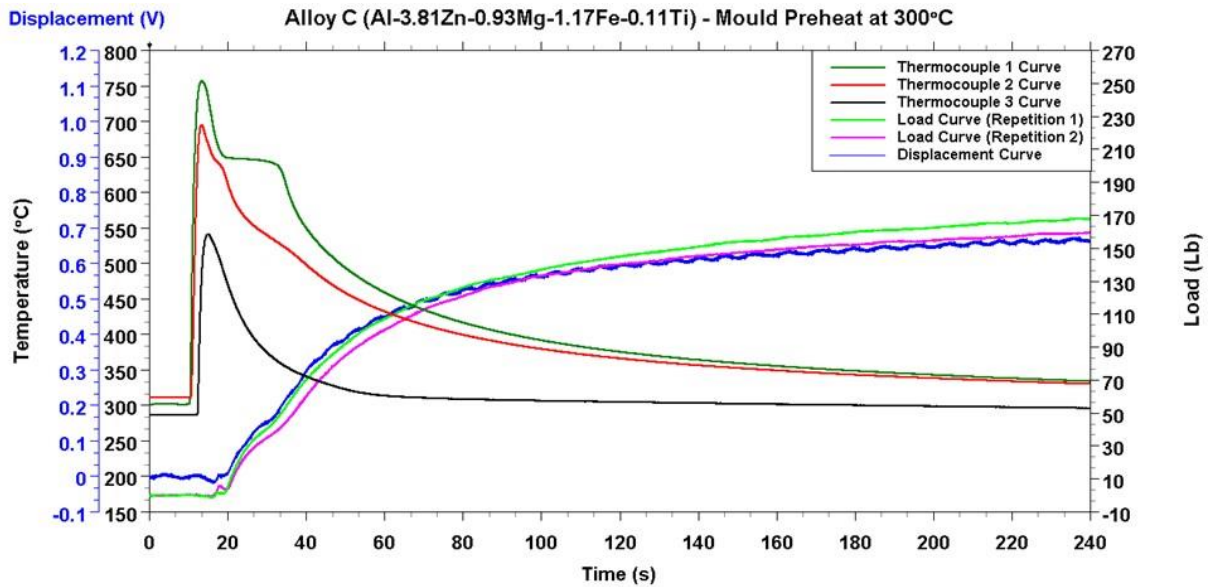
Figure A-10: Alloy C at mould preheat at 250⁰C

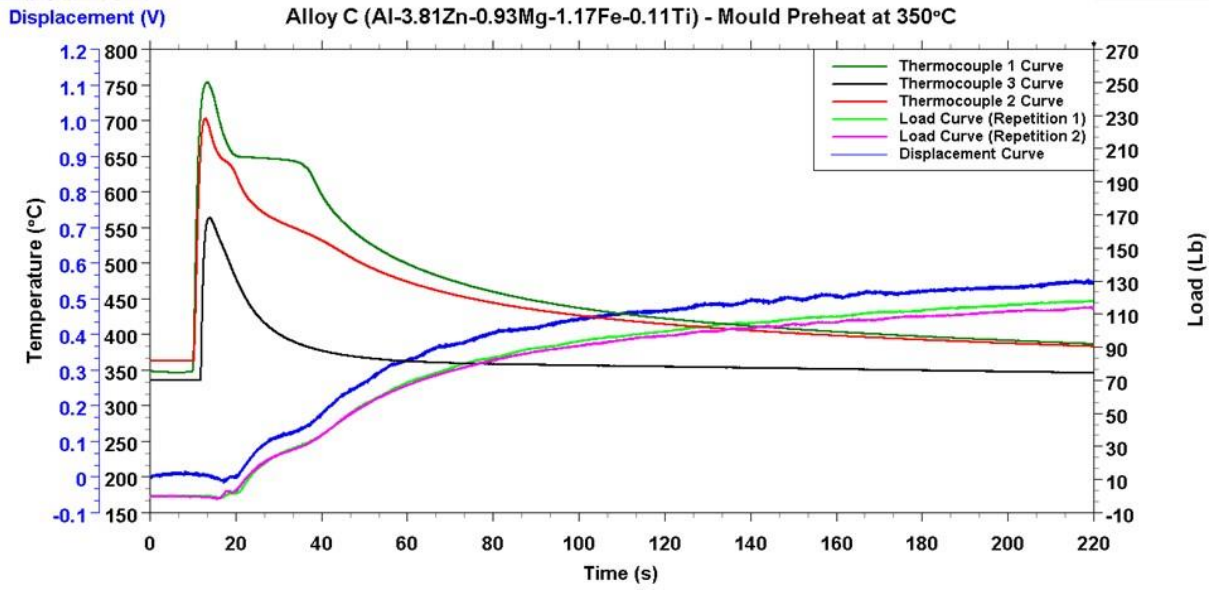
Figure A-11: Alloy C at mould preheat at 300⁰C
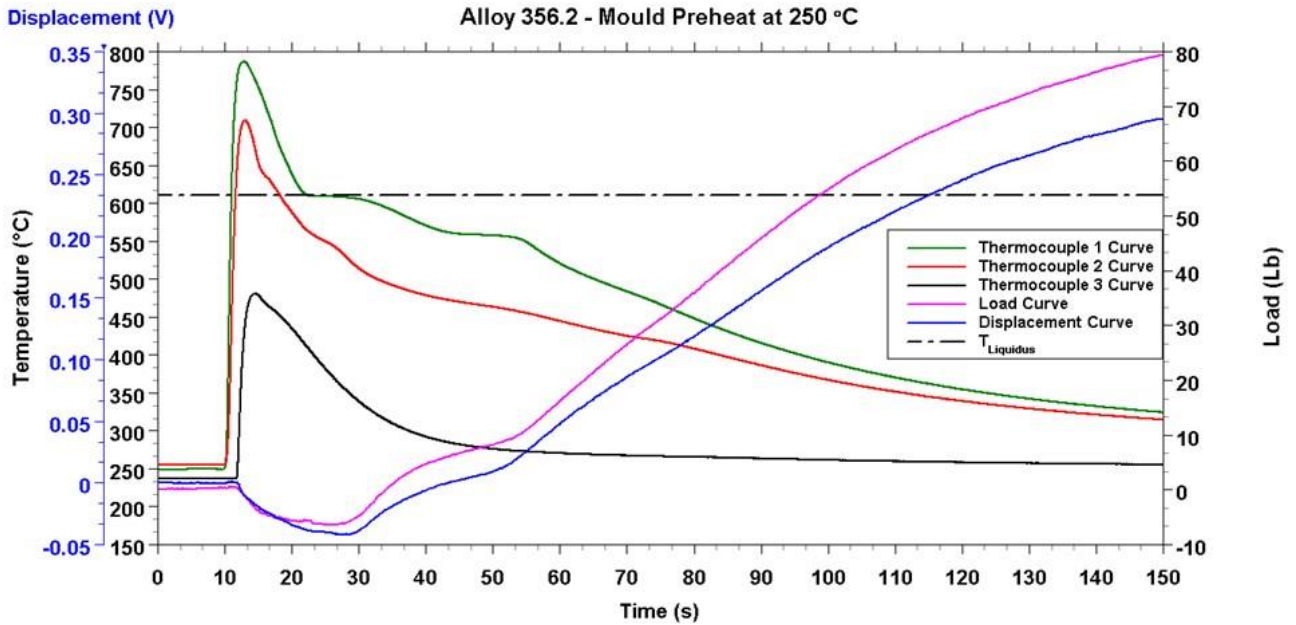
Figure A-12: Alloy C at mould preheat at 350⁰C

Figure A-13: Alloy A356.2 at mould preheat at 250⁰C